

# UC Riverside

## UC Riverside Electronic Theses and Dissertations

### Title

The Development and Application of Models for Dispersion of Roadway Emissions: The Effects of Roadway Configurations on Near Road Concentrations of Vehicle Emissions and Increasing the Spatial Resolution of Satellite-Derived PM2.5 Maps

### Permalink

<https://escholarship.org/uc/item/8fd5032s>

### Author

Amini, Seyedmorteza

### Publication Date

2018

Peer reviewed|Thesis/dissertation

UNIVERSITY OF CALIFORNIA  
RIVERSIDE

The Development and Application of Models for Dispersion of Roadway Emissions:  
The Effects of Roadway Configurations on Near Road Concentrations of Vehicle Emissions  
and Increasing the Spatial Resolution of Satellite-Derived PM<sub>2.5</sub> Maps

A Dissertation submitted in partial satisfaction  
of the requirements for the degree of

Doctor of Philosophy

in

Mechanical Engineering

by

Syedmorteza Amini

March 2018

Dissertation Committee:

Dr. Akula Venkatram, Chairperson

Dr. Marko Princevac

Dr. David R. Cocker III

Copyright by  
Seyedmorteza Amini  
2018

The Dissertation of Seyedmorteza Amini is approved:

---

---

---

Committee Chairperson

University of California, Riverside

## ACKNOWLEDGEMENTS

Many individuals have supported me during the work on this dissertation. I would like to share my deepest gratitude to my advisor, Dr. Akula Venkatram, for his constant support and encouragement. His vast knowledge in the field of air quality modeling has helped me learn a lot. Without his guidance and persistent help, this dissertation would have been not possible.

I thank my committee members, Dr. Marko Princevac and Dr. David Cocker, who not only taught me the fundamentals of turbulence and air quality measurement techniques, but also challenged me to improve my work.

I would like to thank my colleague and friend Mr. Faraz Enayati Ahangar. We spent numerous hours working together during field measurements, meetings, conferences, etc. I want to express my utmost gratitude to Dr. Nico Schulte, who taught me fundamentals of data analysis and different instruments' working principles. His willingness to give his time so generously is very much appreciated. I would like to extend my thanks to Dr. Si Tan who always answered my questions regarding the fundamentals of dispersion modeling. I want to offer my special thanks to my friend and colleague, Mr. Masoud Ghasemian, whose proficiency in CFD modeling facilitated my understanding of the effects of vegetation on near road air quality.

Many thanks to Dr. David Heist and Dr. Steven Perry from the U.S. EPA for providing us with the wind tunnel data and fruitful discussions.

The research in chapter 2 was supported by funding provided by the California Air Resources Board under contract number 13-306. I thank the CARB's Research Division staff,

including Dr. Abhilash Vijayan, Mr. Steve Mara, Dr. Walter Ham, and Dr. Toshihiro Kuwayama, for their support during the course of this project. I also thank the UCLA professors Dr. Suzanne Paulson, Dr. Yifang Zhu, and our colleagues at UCLA, Dr. Eon S. Lee, and Ms. Dilhara Ranasinghe for having useful discussions regarding the project.

The research in chapter 5 was supported by funding provided by NASA Earth Sciences Division Applied Sciences Program. I would like to thank the San Jose State University professor Dr. Frank Freedman, Dr. Mohammad Al-Hamdan from NASA Marshall Space Flight Center in Huntsville, AL, Dr. Robert Chatfield from NASA Ames Research Center in Moffett Field, CA, and Dr. Sang-Mi Lee from South Coast Air Quality Management District for giving me different perspectives of the problems.

I would like to express my very great appreciation to my parents, Ebrahim and Nahid, for their encouragement, understanding, support, and love. My sincerest gratitude goes to my lovely wife Maryam for her support and patience during this journey. Without her love and dedication, reaching the end of this road would have been impossible. And last but not least, I would like to thank my sister, Zahra, and brothers, Hamed and Hassan, for their enormous love and support during all my life.

The text in chapter 2 of this dissertation is in part a reprint of the material as it appears in Amini, S., Ahangar, F.E., Schulte, N., Venkatram, A., 2016. Using models to interpret the impact of roadside barriers on near-road air quality. *Atmos. Environ.* 138, 55-64. doi:10.1016/j.atmosenv.2016.05.001.

Dedicated to

My parents

Ebrahim and Nahid

My wife

Maryam

And my siblings

Zahra, Hamed, and Hassan

## ABSTRACT OF THE DISSERTATION

The Development and Application of Models for Dispersion of Roadway Emissions:  
The Effects of Roadway Configurations on Near Road Concentrations of Vehicle Emissions  
and Increasing the Spatial Resolution of Satellite-Derived PM<sub>2.5</sub> Maps

by

Seyedmorteza Amini

Doctor of Philosophy, Graduate Program in Mechanical Engineering  
University of California, Riverside, March 2018  
Dr. Akula Venkatram, Chairperson

Near road air quality is a public concern because exposure to elevated concentrations of vehicular pollution is associated with adverse health effects. Roadway design is suggested as a potential strategy to mitigate near-road exposure. The first part of my dissertation describes the development and application of roadway dispersion models to examine the effectiveness of roadway configurations as pollutant mitigation strategies. These configurations include depressed roadways and at-grade roadways with the presence of solid/vegetative barriers.

Roadside solid barriers increase dispersion of pollutants by lofting emissions and inducing a recirculation zone on their leeward edge. I adapt a model, developed using data from a wind tunnel, to describe ultrafine particle measurements made in a field study. This requires modifying the model to account for uncertainties in emissions and meteorological parameters of real-world studies. Results suggest that 1) a model developed under

controlled conditions is useful in the complex environment of urban areas, 2) the surface can be taken neutral in modeling dispersion in urban areas., and 3) the primary impact of the barrier is equivalent to shifting the road upwind by a distance of  $H(U/u^*)\cos\theta$ .

I next analyze data from a wind tunnel that examined dispersion of emissions from depressed roadways using roadway dispersion models. I show that dispersion governed by the complex flow induced by depressed roads can be described using modified flat-terrain models. The modifications include 1) an initial vertical spread dependent on the geometry of the depressed roadway, and 2) increasing the friction velocity above its upwind value. Also, the vertical concentration profiles under neutral stability conditions are best explained with a vertical distribution function with an exponent of 1.3 rather than the 2 used in most currently used dispersion models.

Health risk assessment of PM<sub>2.5</sub> on the community scale requires PM<sub>2.5</sub> concentration estimations at the scale of tens of meters. The PM<sub>2.5</sub> measurement from air quality stations and satellite-derived PM<sub>2.5</sub> estimates cannot provide concentrations at this spatial resolution. In the last part of my dissertation, I describe a “downscaling” system that adapts roadway dispersion models to yield the concentration gradients that are not captured by satellite maps.

## TABLE OF CONTENTS

<b>1</b>	<b>Motivation, Objectives, and Approach .....</b>	<b>1</b>
1.1	Problem statement .....	1
1.2	Background .....	5
1.2.1	The effectiveness of the roadside solid barriers and vegetation to reduce near-road pollutant concentrations .....	5
1.2.2	The effects of depressed roads on concentrations of roadway-emitted air pollutants .....	9
1.2.3	Downscaling satellite-derived PM <sub>2.5</sub> concentrations to community scale .....	12
1.3	Objectives and approach.....	13
1.4	Structure of the dissertation .....	16
<b>2</b>	<b>Effect of Solid Barriers on Dispersion from Roads.....</b>	<b>17</b>
2.1	Introduction .....	17
2.2	Field study .....	22
2.2.1	Site description .....	22
2.2.2	Measurements.....	24
2.3	Experimental results.....	28
2.3.1	Air quality.....	28
2.3.2	Meteorology .....	31
2.4	Framework for the barrier models .....	33
2.4.1	Simple barrier model.....	33
2.4.2	Modified mixed-wake model .....	34
2.5	Comparison with observations .....	36
2.6	Summary and conclusions .....	42

<b>3</b>	<b>Effect of Vegetation Barriers on Dispersion from Roads .....</b>	<b>45</b>
3.1	Introduction .....	45
3.2	Wind tunnel experiments .....	48
3.2.1	Experiment description.....	48
3.2.2	Experimental results.....	51
3.3	Data analysis .....	59
3.4	Conclusions and summary .....	61
<b>4</b>	<b>Modeling Dispersion of Emissions from Depressed Roadways.....</b>	<b>63</b>
4.1	Introduction .....	63
4.2	Wind tunnel experiments .....	66
4.2.1	Experiment description.....	66
4.2.2	Experimental results.....	70
4.3	Framework for the depressed road models .....	74
4.3.1	Modified van Ulden model .....	74
4.3.2	Modified RLINE model .....	81
4.4	Comparison of the modified models with observations .....	83
4.4.1	Modified van Ulden model .....	84
4.4.2	Modified RLINE model .....	87
4.5	Discussions.....	89
4.6	Summary and conclusions .....	91
<b>5</b>	<b>Downscaling Satellite-Derived PM<sub>2.5</sub> Surface Concentration Fields Using Dispersion Models.....</b>	<b>93</b>
5.1	Introduction .....	93
5.2	System design.....	94
5.2.1	System overview .....	94

5.2.2	System description .....	95
5.2.3	Dispersion models formulations .....	96
5.2.4	Dispersion models inputs .....	99
5.2.5	Dispersion model outputs.....	101
5.3	I-710 field study .....	102
5.4	Results of the field study .....	106
5.4.1	Meteorology .....	106
5.4.2	Fine particulate matter, black carbon content, and NOx concentrations .....	107
5.5	Dispersion modeling results .....	110
5.5.1	Simple line source model assessment .....	114
5.5.2	Analytical line source model assessment.....	117
5.6	Demonstration of the proposed system.....	121
5.7	Summary and conclusions .....	125
<b>6</b>	<b>Conclusions .....</b>	<b>128</b>
6.1	Roadside solid barriers .....	129
6.2	Roadside vegetation barriers.....	131
6.3	Depressed roadway configurations .....	132
6.4	Downscaling satellite-derived PM <sub>2.5</sub> concentrations.....	134

## LIST OF FIGURES

Figure 2-1- Co-ordinate systems used to calculate contribution of point source at $Y_s$ to concentration at $(X_r, Y_r)$ . The system $x-y$ has the $x$ -axis along the mean wind direction, which is at an angle $\theta$ to the fixed $X$ -axis. Adapted from (Venkatram and Horst, 2006). ...	20
Figure 2-2- Schematic of concentration profile in the mixed-wake model. ....	21
Figure 2-3- Map of the selected site. Adapted from Google Map. ....	23
Figure 2-4- Co-location of CPCs before start of tests. ....	26
Figure 2-5- Approximate location of instruments. ....	26
Figure 2-6- Sonic anemometer attached to a light post behind the barrier. ....	28
Figure 2-7- Time series of UFP number concentrations between 4 pm and 5 pm of test 6.	29
Figure 2-8- Averaged particle concentrations at different distances behind the barrier for a) Test 1, b) Test 2, c) Test 3, d) Test 4, e) Test 5, and f) Test 6.....	30
Figure 2-9- Observed wind rose measured by the upwind 3-D sonic anemometer along with freeway direction.....	31
Figure 2-10- Comparison of observed a) wind speed and b) standard deviation of vertical velocity fluctuations ( $\sigma_w$ ) downwind of the barrier against upwind of the freeway.....	32
Figure 2-11- Schematic of concentration profile in the modified mixed-wake model.....	34
Figure 2-12- Comparison of observations and a) simple barrier model estimates and b) the modified mixed-wake model estimates.....	38
Figure 2-13- Fractional bias versus barrier height for modified mixed-wake model (red solid line) and for simple barrier model (black dashed line).....	39

Figure 2-14- Concentration gradients for observations and a) simple barrier model for test 3, b) the modified mixed-wake model for test 3, c) simple barrier model for test 4, d) the modified mixed-wake model for test 4, e) simple barrier model for test 6, and f) the modified mixed-wake model for test 6. (Emission factors are calculated for each day using the data measured beyond 40 m from the barrier.) .....	40
Figure 2-15- Comparison of estimated normalized concentrations, to no-barrier case, behind barriers with different heights for a) simple barrier model and b) the modified mixed-wake model.....	42
Figure 3-1- Illustration of line sources, roughness blocks, and filter material representing vegetation (view from upwind).....	49
Figure 3-2- Schematic of the line sources in the wind tunnel study; a) looking crosswind, and b) looking upwind.....	50
Figure 3-3- Magnitudes of observed velocity and velocity fields for a) solid barrier case and b) vegetation barrier case. Barriers are represented by black rectangles.....	53
Figure 3-4- Contours of vertical velocity fluctuations for a) solid barrier case and b) vegetation barrier case. Barriers are represented by black rectangles. ....	54
Figure 3-5- Contours of longitudinal velocity fluctuations for a) solid barrier case and b) vegetation barrier case. Barriers are represented by black rectangles. ....	55
Figure 3-6- Scatterplots comparing $\sigma_u$ values with $\sigma_w$ values at different points within the wind tunnel for a) solid barrier case, and b) vegetation case. ....	55
Figure 3-7- Concentration contours for a) flat terrain, b) solid barrier, and c) vegetation cases. Barriers are represented by red rectangles. ....	56

Figure 3-8- Vertical profiles of concentrations for all 3 case at six different downwind distances.....	58
Figure 3-9- Vertical profiles of the ratio of $\sigma_u$ behind vegetation barrier to $\sigma_u$ in undisturbed boundary layer. The vegetation extends from $x = 2H_w$ to $x = 3H_w$ . .....	60
Figure 3-10- Comparison of measured surface concentrations with estimated surface concentrations versus downwind distance in the flat terrain case. ....	60
Figure 3-11- Comparison of the measured surface concentrations with estimated surface concentrations versus downwind distance. Vegetation ends at $3H_w$ . ....	61
Figure 4-1- Schematic of near roadway wind tunnel setup: a) elevation and b) plan view. ....	68
Figure 4-2- Elevation view showing cross sections through the different roadway designs studied; a) flat terrain roadway (FLAT), b) 6 m deep depressed roadway with vertical sidewalls (D690), c) 6 m deep depressed roadway with 30° sloping sidewalls (D630), and d) 9 m deep depressed roadway with vertical sidewalls (D990). The small black rectangles indicate the location of the tracer emission lines. The width of the road in all cases is 36 m. Adapted from Heist et al. (2009). ....	69
Figure 4-3- Observed mean velocity vectors for a) FLAT, b) D690, c) D630, and d) D990 cases.....	71
Figure 4-4- Vertical profiles of horizontal velocity at multiple downwind locations in FLAT case. The air speed increases as air travels downwind. ....	72
Figure 4-5- Gradient of square root of TKE values of a) D690, b) D630, and c) D990 cases, normalized by the corresponding values observed at flat terrain case. ....	73
Figure 4-6- Surface concentration as a function of downwind distance for different road configurations. Left plot includes flat terrain concentrations. ....	74

Figure 4-7- Performance of a vertical distribution function with exponent  $s=1.3$  in estimating vertical concentration profiles of the FLAT case at different downwind distances. .... 77

Figure 4-8- Performance of a vertical distribution function with exponent  $s=2$  in estimating vertical concentration profiles of the FLAT case at different downwind distances. .... 78

Figure 4-9- Comparison of modified van Ulden model estimates (with  $s=1.3$  and  $p=1/7$ ) with observed concentrations; a) FLAT case, b) D690 case, c) D630 case, and d) D990 case.... 85

Figure 4-10- Comparison of the vertical concentration profiles at multiple downwind locations predicted by the modified van Ulden model (with  $s=1.3$  and  $p=1/4$ ) with those of the observations (D690 case). .... 86

Figure 4-11- Performance of the modified van Ulden model in predicting concentration vertical profiles of different cases at  $x=3H$  (Open squares – measured flat terrain, solid circles – measured D690, dashed line – modeled flat terrain, and solid line – modeled D690).... 87

Figure 4-12- Performance of modified RLINE model in estimating concentrations below 6 m height for all downwind distances. .... 88

Figure 4-13- Comparison of the vertical concentration profiles at multiple downwind locations predicted by the modified RLINE model with those of the observations (D690 case)..... 89

Figure 4-14- Ratio of surface concentrations downwind of barrier cases to those of D690 case. (Solid circle corresponds to 6 m double solid barriers and open square corresponds to 6 m downwind barrier). .... 90

Figure 5-1- Overview of the system resulting in downscaled concentrations..... 95

Figure 5-2- Major line sources implemented into the line-source dispersion model for the South Coast air basin. Circles indicate locations of mileposts where AADT is measured. Left panel, entire area; Right panel, zoomed-in over area around Riverside, CA. ....100

Figure 5-3- Aerial view of the sampling area showing the locations of the two monitoring stations near the I-710 freeway (“near” and “far” sites), and the background site in Del Amo. Adapted from (Polidori and Fine, 2012). .... 103

Figure 5-4- Diurnal variation of average traffic flow rate of Light Duty Vehicles (LDV) and High Duty Vehicles (HDV) for a) winter weekdays, b) winter weekends, c) summer weekdays, and d) summer weekends. Error bars indicate one standard deviation. ....106

Figure 5-5- Observed wind rose measured by the upwind 3-D sonic anemometer along with freeway direction. ....107

Figure 5-6- Representative 1-hr average of a) winter BC, b) summer BC, c) winter NO<sub>x</sub>, and d) summer NO<sub>x</sub>, at the ‘near’, ‘far’, and Del Amo stations. .... 110

Figure 5-7- Comparison of BC observed concentrations and simple line source model estimates during a) winter unstable, b) winter stable, c) summer unstable, and d) summer stable. Emission factors are shown on each plot. ....115

Figure 5-8- Comparison of NO<sub>x</sub> observed concentrations and simple line source model estimates during a) winter unstable, b) winter stable, c) summer unstable, and d) summer stable. Emission factors are shown on each plot. ....117

Figure 5-9- Comparison of BC observed concentrations and analytical line source model estimates during a) winter unstable, b) winter stable, c) summer unstable, and d) summer stable. Emission factors are shown on each plot. .... 119

Figure 5-10- Comparison of NO<sub>x</sub> observed concentrations and simple line source model estimates during a) winter unstable, b) winter stable, c) summer unstable, and d) summer stable. Emission factors are shown on each plot. ....121

Figure 5-11- The area of study. The left panel shows the 3-km grid generated by (Al-Hamdan et al., 2014). The right panel shows the generated subgrids with their centers marked by asterisks. The scale of each subgrid is 500 m. .... 122

Figure 5-12- The line sources detected within the grid (indicated by red lines). The red circles indicate the traffic sensors available in AADT files ..... 123

Figure 5-13 the plot of estimated daily-averaged primary PM<sub>2.5</sub> concentrations due to line sources within the 3-km grid.....124

Figure 5-14- Downscaled PM<sub>2.5</sub> concentrations at the scale of 100 m. .... 125

## LIST OF TABLES

Table 2-1- Overview of dates and duration of measurements.....	25
Table 2-2- Meteorological conditions.....	32
Table 4-1- Values of empirical parameters of different cases that form the $\sigma z$ expression ( $s=1.3$ and $p = 1/4$ ).....	79
Table 4-2- Values of empirical parameters of different cases that form the $\sigma z$ expression ( $s=1.3$ and $p = 1/7$ ).....	81
Table 4-3- Values of empirical parameters of different cases that form the $\sigma z$ expression in RLINE model. ....	83
Table 5-1- List of the particle and gaseous species monitored during this study. Both continuous and integrated measurement techniques were used to collect/monitor all targeted pollutants. Adapted from Polidori and Fine (2012). ....	104
Table 5-2- Average and median fine particulate matter (PM <sub>2.5</sub> ), black carbon (BC), and NO <sub>x</sub> concentrations at the “near”, “far” and background stations during the winter and summer campaigns. Minimum (Min) and maximum (Max) values, standard deviations (SD), and the total number of valid samples (Valid N) are also included. Background PM <sub>2.5</sub> , BC, and NO <sub>x</sub> data were measured at the North Long Beach station, Del Amo station, and Del Amo station respectively. (Adapted from Polidori and Fine (2012)).....	108
Table 5-3- Gasoline and diesel vehicle emissions under test cycles similar to cruise driving patterns. ....	113

# 1 Motivation, Objectives, and Approach

## 1.1 Problem statement

The impact of roadway emissions on air quality has been studied since the 1970s. Recently, a number of epidemiological studies have reported associations between living within a few hundred meters of high-traffic roadways and adverse health effects such as asthma and other respiratory impacts, birth and developmental effects, premature mortality, cardiovascular effects, and cancer (Beelen et al., 2008; Gehring et al., 2010; Hoek et al., 2002; Wellenius et al., 2012; Wilhelm & Ritz, 2003). Air quality monitoring studies conducted near major roadways suggest that these health effects are associated with elevated concentrations, compared with overall urban background levels, of various motor-vehicle-emitted compounds. These compounds include carbon monoxide (CO); nitrogen oxides (NO<sub>x</sub>); coarse (PM<sub>10-2.5</sub>), fine (PM<sub>2.5</sub>), and ultrafine (PM<sub>0.1</sub>) particle mass; particle number; black carbon (BC), polycyclic aromatic hydrocarbons (PAHs), and a suite of volatile organic compounds including benzene (Hitchins et al., 2000; Kim et al., 2002; Kittelson et al., 2004; Zhu et al., 2002a, 2002b).

The need to relate near-road pollutant concentrations to vehicular emissions has led to the development of variety of dispersion models that treat the processes that govern the transport and transformation of emitted pollutants (Holmes and Morawska, 2006). The research described in this thesis deals with a class of dispersion models referred to as semi-empirical models. While these models have mechanistic foundations, some of the physical processes are modeled using parameters whose values are obtained by fitting model estimates to corresponding observations. The most commonly used models, such as AERMOD (Cimorelli et al., 2005) belong to this class of models.

Semi-empirical dispersion models that treat a highway as a continuous line source are critical components of studying the health effects of exposure to vehicle emissions near major roads. Until recently, CALINE<sub>3</sub> (Benson, 1992) and more refined models such as CAL<sub>3</sub>QHC and CAL<sub>3</sub>QHCR were recommended by the United States Environmental Protection Agency (U.S. EPA) for estimating the impact of vehicular emissions on near-road air concentrations. The situation changed in 2016 when the U.S. EPA replaced CALINE<sub>3</sub> with the American Meteorological Society/U.S. EPA Regulatory Model (AERMOD) for Transportation Related Air Quality Analyses (U.S. Environmental Protection Agency, 2016). However, AERMOD designed primarily for point, area, and volume-type pollutant sources does not simulate the line-type sources explicitly; line sources are represented as elongated area sources or a series of volume sources evenly spaced along the length of the lines (Heist et al., 2013). AERMOD is also not currently configured to model concentrations downwind of roadways with complex geometries.

In an effort to develop a comprehensive line source dispersion model, the U.S. EPA formulated the Research LINE source model (RLINE) (Snyder et al., 2013, Snyder and Heist,

2013). The model framework is designed to facilitate the inclusion of algorithms for complex road geometries, therefore providing a suitable testbed for potential depressed roadway approaches. To add algorithms of complex geometries to RLINE, there is a critical need to develop line source dispersion models that model dispersion of emissions from roadways with complex geometries. My research contributes to the development of models such as AERMOD and RLINE that play a major role in enforcing air quality regulations and in estimating the health impact of vehicular emissions.

Health researchers have increasingly found that fine particulate (PM<sub>2.5</sub>; particle size less than 2.5  $\mu\text{m}$  in the aerodynamic diameter) leads to increased risk of cardiovascular and respiratory diseases (Dominici et al., 2015; Gold et al., 2000; Peters et al., 2001). In response to these studies, the U.S. EPA and local agencies within the United States monitor the daily averages of ground-level PM<sub>2.5</sub> and distribute the data through U.S. EPA Air Quality System (AQS) at <http://www.epa.gov/aqs>. However, due to the relatively large horizontal spacing of these monitors (10s – 100s of kilometers), these datasets are not suitable for health risk assessment on the community scale (10s-1000s of meters), which requires concentration estimates at these scales and near high emission areas such as freeways.

Satellite remote sensing provides a potentially cost effective way to estimate PM<sub>2.5</sub> concentrations by using Aerosol Optical Depth (AOD) in areas where monitors are not available or too sparse (Hoff and Christopher, 2009). AOD measures light extinction by aerosol scattering and absorption in an atmospheric column and is related to the loadings of fine particles in the column. AOD products from several satellite sensors such as the Moderate Resolution Imaging Spectroradiometer (MODIS) (Hu et al., 2014; Liu et al., 2007a; Zhang et al., 2009), the Multiangle Imaging SpectroRadiometer (MISR) (Liu et al., 2007a,

2007b, 2007c), and the Geostationary Operational Environmental Satellite Aerosol/Smoke Product (GASP) (Liu et al., 2009; Paciorek and Moreno-macias, 2008) have been used in previous studies for estimating PM<sub>2.5</sub> concentrations.

The MODIS aboard NASA's *Terra* and *Aqua* satellites makes near-global daily observations of the earth in a wide spectral range (0.41 – 15  $\mu\text{m}$ ). These measurements are used to derive AOD over land and ocean. To resolve the spatial spacing problem of the AQS, researchers have used the Dark Target (DT) (Levy et al., 2013) and Deep Blue (DB) (Hsu et al., 2013) products of the MODIS AOD measurements to estimate PM<sub>2.5</sub> surface concentrations (Al-Hamdan et al., 2014; Lee et al., 2016, 2011, Liu et al., 2007a, 2005; van Donkelaar et al., 2006; Van Donkelaar et al., 2013; You et al., 2015). Since releasing the new AOD retrieval algorithm, PM<sub>2.5</sub> surface concentrations can be estimated at the scales of 3 km (Remer et al., 2013). Although spatially continuous, these PM<sub>2.5</sub> surface concentration fields are too coarse to directly represent the community scale, where health risk locally can be much higher than the reported concentration. Thus there is a need for a method that increases the spatial resolution of the 3-km satellite-derived PM<sub>2.5</sub> concentration fields by incorporating results from dispersion models that can estimate concentrations at distances of meters from the relevant sources.

Air pollution concentrations on sub-kilometer to kilometer scales are typically estimated by dispersion models. Since major sources of PM<sub>2.5</sub> emissions in California are freeways (Hasheminassab et al., 2014), it is critical to develop a system that estimates PM<sub>2.5</sub> concentrations due to emissions from freeways at community scale and blends them with the satellite-derived 3-km PM<sub>2.5</sub> concentration fields. The final result of the system yields a finer resolution of total PM<sub>2.5</sub> surface concentrations.

In this thesis, I report development of dispersion models that estimate concentrations near roadways with different geometries, including roadways with a downwind solid barrier, roadways with thick roadside vegetation, and roadways with depressed geometries. I also explain the development of a system that “downscales” 3-km satellite-derived PM<sub>2.5</sub> surface concentrations to community scale for health risk assessments.

## **1.2 Background**

### **1.2.1 The effectiveness of the roadside solid barriers and vegetation to reduce near-road pollutant concentrations**

Several approaches have been suggested to reduce exposure to traffic-related air pollutants near roadways. These approaches include:

1. More stringent vehicle emission standards,
2. Speed reduction mechanisms, including roundabouts,
3. Traffic signal management,
4. Speed limit reductions on high-speed roadways (>55 mph),
5. Adding solid barriers, such as sound walls,
6. Adding vegetation barriers next to roads

The first four approaches are related to reducing vehicle emissions and the last two deal with increasing dispersion of traffic emissions. Solid barriers enhance vertical dispersion by lofting the vehicle emissions and thereby reducing near-road concentrations of vehicle emissions. Vegetation barriers have been suggested as a potential strategy to decrease concentrations near roadways by increasing lofting and filtering some of the particles; however, the impact of vegetation on reducing turbulence in the flow passing through it

may increase concentrations. The porosity and the thickness of vegetation determine whether or not vegetation mitigates concentrations near roads (Ghasemian et al., 2017). In the next section, we discuss the important findings of the effects of solid barriers and vegetation on near-road air quality.

#### **1.2.1.1 Roadside solid barriers**

Major roads in California that have a section with houses next to them are often designed with solid barriers to reduce traffic noise. Since these barriers are already in place, there is a growing need to understand how they affect air quality near freeways and the most important factors determining their degree of concentration mitigation.

The U.S. EPA conducted a comprehensive wind tunnel study on the effects of different road configurations on concentrations near roadways (Heist et al., 2009). They studied twelve different road configurations and simulated a six-lane divided highway in a 1:150 scale. Six of the road configurations contained solid barriers next to the road and one of them had a downwind solid barrier. They found that the roadway with a downwind solid barrier decreases surface concentrations relative to that of flat roadway over multiple downwind distances. They also explained the collected data using a modified Gaussian plume dispersion model. They claimed that the impact of a solid barrier on the surface concentrations downwind of a roadway can be modeled by assuming that addition of the solid barrier is equivalent to shifting the line sources upwind by a distance of several barrier heights.

To confirm the results of the wind tunnel study, a tracer study was conducted in Idaho Falls, ID (Finn et al., 2010). Two measurements were conducted next to each other, one represented flat road and the other contained a downwind solid barrier case along the

simulated flat road. In each measurement, SF<sub>6</sub> tracers were released from 54 m long line sources and the tracer concentrations were measured using bag samplers. Everything in both measurements were identical except that a 6 m solid barrier was present downwind of the line source in the solid barrier case. The measurements were conducted under different atmospheric stability conditions and the results showed that the solid barrier decreases surface concentrations downwind of the freeway under all atmospheric stability conditions.

Two semi-empirical dispersion models, called 'mixed-wake model' and 'source-shift model', were developed to explain the results of the wind tunnel and the tracer study (Schulte et al., 2014). The mixed-wake model assumes that the solid barriers 1) induce a mixed-wake region downwind of the road causing a constant concentration below barrier height and 2) increase the vertical plume spread by a factor  $\alpha$ , which is formulated based on the observed concentrations. The source-shift model is based on the idea developed by Heist et al. (2009) and parameterizes the amount of source-shift by assuming that the vertical plume spread at the location of the barrier is proportional to the barrier height.

While these models provided good descriptions of concentrations measured in both studies, they overestimated concentrations near the barrier during unstable conditions. Furthermore, since these models were formulated based on controlled wind tunnel and tracer studies, their performance against field data collected next to a roadside barrier had to be evaluated and the necessary modifications had to be made to improve their performance, if necessary. This work is discussed in chapter 2.

#### **1.2.1.2 Roadside vegetation barriers**

Vegetation barriers have been suggested as a potential strategy to mitigate near-road air pollution. However, there is still a debate on the effects of vegetation on concentrations

downwind of roadways. Some field studies conducted downwind of the roadside vegetation barriers have shown that presence of vegetation next to a roadway reduces concentrations (Al-Dabbous and Kumar, 2014). Some other studies have shown that depending on the type of the particulates, vegetation may result in lower or the same level of concentrations (Brantley et al., 2014). Some studies have found that the concentrations of PM<sub>2.5</sub> may increase in presence of vegetation barriers due to their effects on reduction of turbulence (Tong et al., 2015). Another field campaign also found that presence of a vegetation barrier can result in higher, lower, or the same concentration levels as those measured in the section without barriers (Hagler et al., 2012).

Computational Fluid Dynamics (CFD) models were developed to study the impacts of roadside vegetation barriers on concentrations in vicinity of roadways. These models assumed that vegetation barriers affect flow field and concentrations in three main ways: 1) they increase vertical mixing by lofting some of the particles, 2) they lower wind speed and lower turbulence behind the vegetation barrier, and 3) they remove some particles by dry deposition. A CFD model developed by Steffens et al. (2012) showed that increases in Leaf Area Density (LAD) increases the amount of depositions that occurs. Another CFD modeling study conducted by Vos et al. (2013) suggested that concentrations are higher in presence of trees in street canyons. Ghasemian et al. (2017) developed a CFD model to estimate concentrations downwind of the roadside solid and vegetation barriers. They first evaluated the model by comparing the estimated concentrations downwind of a solid barrier against the results of the wind tunnel study (Heist et al., 2009). After validation of the numerical methodology, concentrations downwind of vegetation barriers with different LADs were estimated. They concluded that dense canopies behave similar to the solid

barriers and mitigate the pollutant concentrations; while high porosity canopies reduce wind speed and increase pollutant concentrations.

The U.S. EPA conducted a wind tunnel study to examine the effects of roadside vegetation on concentrations near freeways. They studied a model flat roadway case with no structures next to it, a model flat roadway with presence of a 9 m high solid barrier downwind of the line sources, and a model flat roadway with presence of a 9 m × 9 m vegetation barrier downwind of the line sources. They found that vegetation barriers can result in significant increase in surface concentrations relative to the flat roadways. In chapter 3, we use dispersion models to analyze the results of this study and to explain the effects of vegetation on dispersion of emissions from roadways.

### **1.2.2 The effects of depressed roads on concentrations of roadway-emitted air pollutants**

Depressed roadways are one type of roadway configurations. Despite their abundance, only a few studies have focused on dispersion of emissions from depressed roads. An extensive field study was conducted in Los Angeles Air Basin by California Department of Transportation (CalTrans) to collect data to understand the dispersion of primary pollutants emitted from freeways with various configurations, including at-grade, depressed, and elevated (Bemis et al., 1977). The results of this study were incorporated into the development of a dispersion model called CALINE2 (Bemis et al., 1977).

Feeney et al. (1975) measured aerosols and particulate lead concentrations in the vicinity of several road configurations, including a depressed roadway. Samplers were placed 20 m upwind of a freeway and at several distances downwind of the freeway ranging from 27 m to approximately 160 m from the median strip. They found that the mass

concentrations of traffic-derived lead were generally lower downwind of the depressed roadway relative to that predicted by a dispersion model that assumed the emissions occurred at road level.

Heist et al. (2009) conducted a comprehensive wind-tunnel study on dispersion of emissions from model depressed roadways. The studied configurations included a flat roadway, a 6 m and a 9 m deep depressed roadway with vertical sidewalls, a 6 m deep depressed roadway with 30° sloping sidewalls, and a 6 m deep depressed roadway with 30° sloping sidewalls with two 6 m solid barriers on top of the road. They observed that these configurations alter the flow field, increase downwind dispersion, and reduce downwind surface concentrations relative to the flat terrain case. The level of reduction in concentrations depended on the particular configuration.

Wind tunnel studies can provide more information on the processes that govern dispersion in complex situations than field studies can because the governing inputs are controlled and details of the flow fields can be measured. Although they do have the disadvantage of being unable to simulate the effects of atmospheric stability, they provide information that is vital to the development of models for situations in which the effects of source geometry on the flow field are dominant. For example, the wind tunnel results (Heist et al., 2009) on dispersion of pollutants downwind of the roadways in the presence of noise barriers have been incorporated into several dispersion and CFD models (Ahangar et al., 2017b; Amini et al., 2016; Ghasemian et al., 2017; Hagler et al., 2011; Schulte et al., 2014; Steffens et al., 2014).

Baldauf et al. (2013) conducted a field study in Las Vegas, Nevada, to investigate the effects of a depressed roadway on local-scale air quality downwind of the depression. They

measured CO and NO<sub>x</sub> concentrations along a complex urban highway at two sections; a section at-grade with the surroundings and another section that was depressed. The vertical height from the roadbed to the top of the surroundings was 5 m, and the slope of the sidewalls was approximately 20°. The stationary monitors located 20 m from the downwind edge of the freeway at both sections showed that the maximum concentration events occurred at the at-grade site. However, during some mid- and low-concentration events, the monitor downwind of the cut section observed higher concentration levels than that of the at-grade section. The mobile monitoring data collected along the at-grade and cut section transects indicated that the concentrations at the at-grade transect were greater than those at the cut section transect at 35 m from the downwind edge of the freeway, with concentrations then becoming similar along both gradients further downwind of the highway. They also conducted a wind tunnel simulation of the study site to examine the flow field and the concentration distributions in the vicinity of the highway. The wind tunnel simulations revealed that the cut section reduced concentrations of pollutants measured at breathing-level height by 15 – 25% relative to the flat terrain case for receptors located approximately 20 m from the downwind edge of the highway. Although the field data were not conclusive, the data collected under the controlled conditions of the wind tunnel indicated that depressed roadways led to reductions in downwind near-surface concentrations relative to those next to at-grade roadways.

The observed CO concentrations around depressed roads in the CalTrans field study (Bemis et al., 1977) were used to develop the depressed road model in the California Line Source Dispersion Model (CALINE2). CALINE is based on the Gaussian plume model and is used to estimate air pollutant concentrations near roadways. Compared to equivalent at-

grade sites, greater values for initial vertical dispersion are used for depressed roads to explain the observed concentrations in the CalTrans field study (Bemis et al., 1977; Benson, 1992b). Since the U.S. EPA has replaced CALINE<sub>3</sub> with AERMOD for mobile source applications, and AERMOD is unable to estimate concentrations downwind of the depressed roadways, there is a need to develop a dispersion line source model that estimates concentrations downwind of depressed roadways. Our work in chapter 4 provides a foundation for future studies that can result in development of such a model.

### **1.2.3 Downscaling satellite-derived PM<sub>2.5</sub> concentrations to community scale**

Many researchers have attempted to estimate PM<sub>2.5</sub> surface concentrations using data from MODIS instrument aboard NASA's *Terra* and *Aqua* satellites. However, the smallest scale of these concentration fields is 3 km. For the health impact studies, there is a need to estimate PM<sub>2.5</sub> concentrations at much lower scales (10s – 100s of meters). Kloog et al. (2011) incorporated commonly used land use regression (LUR) variables and meteorological variables into a generalized additive mixed model to estimate PM<sub>2.5</sub> concentrations using AOD measurements. To my knowledge, this was the only study that partly enhanced the spatial resolution of the satellite-derived PM<sub>2.5</sub> surface concentrations by using the local (100 m) land use terms to model the difference between grid cell model predictions and measured concentrations.

In the last part of the dissertation we attempt to downscale the satellite-derived PM<sub>2.5</sub> concentrations to a community scale. In order to do so, we first develop a system that connects the satellite-derived concentrations to the concentrations near major roads and we then calibrate the line source dispersion models against a dataset that represents concentrations near a major road in Los Angeles County. Once the line source dispersion

models are calibrated, the system is able to downscale satellite-derived concentrations. The results of this work are discussed in chapter 5.

### **1.3 Objectives and approach**

The major objectives of my research are:

1. Expand the capabilities of currently used roadway dispersion models, such as AERMOD and RLINE, by developing methods to estimate the impact of road configurations and near-road features on dispersion of vehicular emissions in the near-road environment. I focus on the impact of depressed roads and solid/vegetative barriers on dispersion.
2. Incorporate dispersion models in a system that increases the spatial resolution of satellite-derived surface pollution maps to the scales required for health risk assessment in communities.

My technical approach to fulfilling these objectives is based on anchoring the models that are presented here to data from field studies and wind tunnel experiments. This ensures that these models can be used in real-world applications and can be incorporated into regulatory models such as AERMOD. The steps in my technical approach are 1) Formulate a tentative model based on those of existing models, 2) Evaluate the results from the model with data from field studies and wind-tunnel experiments, 3) Use the discrepancies between model results and corresponding measurements to modify model formulation and parameter estimates to yield adequate descriptions of data.

The models developed in this research are the results of the following steps:

1. Evaluating the effectiveness of solid barriers next to roads to reduce near-road pollutant concentrations
  - a. Adapted a dispersion model developed to describe wind tunnel and tracer studies on dispersion of vehicular emissions near roads with presence of a solid barrier (Schulte et al., 2014),
  - b. Planned and performed field measurements of ultrafine particle (UFP) concentrations and the variables that govern dispersion next to a freeway adjacent to the UC Riverside campus,
  - c. Evaluated the performance of the adapted model against the collected data,
  - d. Modified the dispersion model using the discrepancies between model estimates and corresponding measurements,
  - e. Performed sensitivity analysis of the dispersion model to give guidance on the effects of barrier height on near road concentrations.
2. Evaluating the effectiveness of vegetation barriers next to roads to reduce near-road pollutant concentrations
  - a. Incorporated the effects of vegetation barriers on turbulence levels near roadways into a line source dispersion model applicable to at-grade freeways,
  - b. Assessed the model performance against the concentrations observed downwind of a thick roadside vegetation barrier in a wind tunnel,
  - c. Quantified the effects of the vegetation barrier on turbulence field using the modified dispersion model.

3. Evaluating the effects of depressed roadway configurations on concentrations near roadways
  - a. Incorporated the effects of depressed roadways on near-road turbulence levels into a line source dispersion model applicable to at-grade freeways,
  - b. Assessed the model performance against the concentrations observed downwind of the depressed roadways in a wind tunnel (Heist et al., 2009),
  - c. Used the discrepancies between model results and corresponding measurements to modify model formulation and parameter estimates to yield adequate descriptions of data,
  - d. Reformulated the modified model to ensure consistency with current models such as RLINE.
4. Downscaling the satellite-derived 3-km PM<sub>2.5</sub> surface concentrations to community scale using line source dispersion models
  - a. Designed a system that takes the satellite-derived concentration fields and dispersion model outputs to generate the downscaled concentrations,
  - b. Calibrated line source dispersion models to improve their performance against concentration data collected in a field study near a major freeway in Southern California.
  - c. Demonstrated the application of the designed system to show the variations of PM<sub>2.5</sub> within a satellite grid.

## **1.4 Structure of the dissertation**

Chapter 2 describes the field measurements and development of a model that estimates near-road air pollutant concentrations in the presence of solid barrier. Chapter 3 describes the analysis of a wind-tunnel study that examined near-road air pollutant concentrations in the presence of solid/vegetation barriers. Chapter 4 describes the modifications to flat terrain models that enable them to estimate concentrations near depressed road configurations. Chapter 5 describes the application of dispersion models to increase the spatial resolution of satellite-derived surface concentrations maps.

## 2 Effect of Solid Barriers on Dispersion from Roads

### 2.1 Introduction

The majority of the studies conducted to date indicate that solid barriers placed next to roads have a mitigating effect on the impact of vehicular emissions on near-road air quality. The physics that governs this effect has been elucidated through several studies, such as the wind-tunnel study conducted by Heist et al. (2009). Through analysis of wind flow patterns and concentration distributions measured around a 1:150 scale model of a 6 lane divided highway with roadside barriers they showed that the mitigating impact of barriers is governed by two mechanisms: the plume from the road becomes elevated by being forced over the barrier, and vertical dispersion is enhanced by the turbulence created in the wake of the barrier.

The results from the wind tunnel were confirmed in a tracer study conducted by Finn et al. (2010). They studied the effects of a barrier by releasing SF<sub>6</sub> from two identical 54 m long line sources. One source was located 6 m upwind of a 90 m long, 6 m high solid barrier and the other had no structures next to it. Tracer concentrations were measured

simultaneously on identical sampling grids downwind of the sources. Six sonic anemometers measured flow around the barrier. Carefully controlled experiments showed that the barrier reduced downwind concentrations over a wide range of atmospheric stabilities.

Field studies conducted next to roadways confirm that barriers mitigate the impact of vehicle-related emissions. For example, Hagler et al. (2012) found that UFP concentrations at 10 m behind the 6 m barrier were about 50% less than those measured at this distance downwind of road sections without a barrier. Baldauf et al. (2008) found that CO and PM concentrations were reduced by 15% to 50% within 50 m of the 6 m barrier. The effect of the barrier persisted up to at least 20 times the barrier height in these studies, after which the concentration approached the value that would occur without a barrier.

The measurements from the wind tunnel and tracer experiments have been described with a variety of mechanistic models. Hagler et al. (2011) and Steffens et al. (2014) used computational fluid dynamics (CFD) models to produce adequate descriptions of the data from the wind tunnel (Heist et al., 2009). Bowker et al. (2007) used the Quick Urban & Industrial Complex (QUIC) flow model coupled with a Lagrangian particle dispersion model to produce concentration patterns that were roughly consistent with observations from Baldauf et al. (2008).

Schulte et al. (2014) developed a semi-empirical dispersion model to describe data from the wind tunnel and the tracer studies. This model parameterizes the major features of the flow and dispersion effects induced by a barrier to avoid the computational burden of mechanistic CFD models, which have their own set of parameterizations. It is designed to be incorporated into routinely used models such as AERMOD (Cimorelli et al., 2005) or

RLINE (Snyder et al., 2013). The ‘mixed-wake model’ (Schulte et al., 2014) is based on the Gaussian plume formulation for a point source, which gives the concentration as:

$$C(x, y, z) = \frac{Q}{\sqrt{2\pi}\sigma_y(x)} \exp\left(-\frac{y^2}{2\sigma_y^2(x)}\right) F_z(x, z) \quad (2-1)$$

where  $x$ ,  $y$ , and  $z$  are the downwind distance from the source, crosswind distance, and height of the receptor,  $Q$  is the emission rate,  $\sigma_y$  is the horizontal plume spread, and  $F_z$  is the concentration vertical distribution function. For the Gaussian formulation  $F_z$  is:

$$F_z(x, z) = \frac{1}{U(\bar{z})\sqrt{2\pi}\sigma_z(x)} \left[ \exp\left(-\frac{(z - z_s)^2}{2\sigma_z^2(x)}\right) + \exp\left(-\frac{(z + z_s)^2}{2\sigma_z^2(x)}\right) \right] \quad (2-2)$$

where  $\sigma_z$  is the vertical plume spread,  $z_s$  is the source height, and  $U(\bar{z})$  is the wind speed evaluated at the effective plume centerline height,  $\bar{z}$ , defined by:

$$\bar{z} = \frac{\int_0^\infty z C^y(x, z) dz}{\int_0^\infty C^y(x, z) dz} \quad (2-3)$$

where  $C^y(x, z)$  is the crosswind integrated concentration. The expression for  $\bar{z}$  when the source height is zero is  $\bar{z} = \sqrt{2/\pi} \sigma_z$ .

The roadways are treated as line sources consisting of sets of point sources. The concentration due to a line source is calculated by integrating equation 2-1 along the source. Because the integral cannot be evaluated in closed form when the wind direction is not perpendicular to the source, Venkatram and Horst (2006) used an analytical approximation to the integral which results in:

$$C(x, y, z) = \frac{1}{2} \frac{q}{\cos \theta} F_z\left(\frac{x}{\cos \theta}, z\right) [\text{erf}(t_1) - \text{erf}(t_2)] \quad (2-4)$$

where  $t_i$  is:

$$t_i = \frac{(y - y_i) \cos \theta - x \sin \theta}{\sqrt{2}\sigma_y(x \cos \theta + (y - y_i) \sin \theta)} \quad (2-5)$$

and the subscripts refer to the two ends of the source,  $x$  is the perpendicular distance of the receptor from the source,  $y - y_i$  is the distance of the receptor from the two ends of the source along the direction parallel to the source,  $\theta$  is the angle between the wind direction and the perpendicular to the source, and  $q$  is the line source emission rate per unit length (Figure 2-1). This expression performs well for all wind directions, with errors less than 1% except when  $\theta = \pm 90^\circ$  (Venkatram and Horst, 2006).

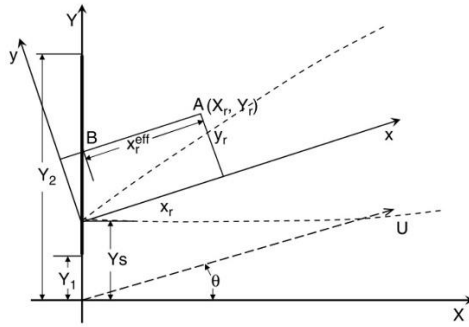


Figure 2-1- Co-ordinate systems used to calculate contribution of point source at  $Y_s$  to concentration at  $(X_r, Y_r)$ . The system  $x$ - $y$  has the  $x$ -axis along the mean wind direction, which is at an angle  $\theta$  to the fixed  $X$ -axis. Adapted from (Venkatram and Horst, 2006).

The plume spreads are calculated using new plume spread formulations (Venkatram et al., 2013) by modeling the concentrations measured at the open terrain site of the Idaho Falls study (Finn et al., 2010). These equations are as follows:

$$\sigma_z = 0.57\alpha \frac{u_*}{U(\bar{z})} x \frac{1}{1 + 3 \frac{u_*}{U(\bar{z})} \left(\frac{x}{L}\right)^{\frac{2}{3}}} \quad L > 0 \quad (2-6a)$$

$$\sigma_z = 0.57\alpha \frac{u_*}{U(\bar{z})} x \left(1 + 2 \frac{u_*}{U(\bar{z})} \frac{x}{|L|}\right) \quad L < 0 \quad (2-6b)$$

$$\sigma_y = 1.6 \frac{\sigma_v}{u_*} \sigma_z \left(1 + 1.5 \frac{\sigma_z}{L}\right) \quad L > 0 \quad (2-7a)$$

$$\sigma_y = 1.6 \frac{\sigma_v}{u_*} \sigma_z \left( 1 + 0.5 \frac{\sigma_z}{|L|} \right)^{-1/3} \quad L > 0 \quad (2-7b)$$

where  $\sigma_v$  is the standard deviation of horizontal velocity fluctuations, and  $L$  is the Monin-Obukhov length. The factor  $\alpha$  was included in vertical plume spread equations by Schulte et al. (2014) to account for increase in vertical plume spread due to presence of the solid barrier.

The mixed-wake model assumes that the concentrations behind the barrier is well-mixed from the surface to the barrier height and the concentration above the barrier follows a Gaussian distribution (Figure 2-2). Thus, the surface concentration associated with an infinitely long line source can be expressed as:

$$C_s = \frac{q}{U \left( \frac{H}{2} \right) \cos \theta H + U(\bar{z}) \cos \theta \sqrt{\frac{\pi}{2}} \sigma_z} \quad (2-8)$$

where  $H$  is the barrier height.

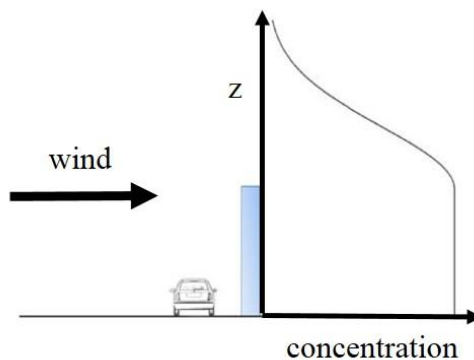


Figure 2-2- Schematic of concentration profile in the mixed-wake model.

The factor that accounted for increase in vertical spread ( $\alpha$ ), was formulated based on the measurements during Idaho Falls study (Finn et al., 2010):

$$\alpha = 1 + 0.005 \frac{\left(\frac{U(H)}{u_*}\right)^2}{1 + \left(\frac{x}{20H}\right)^{0.5}} \quad (2-9)$$

While model predictions compare well with the observed data in the wind tunnel and the tracer study, they are greater than the observed concentrations during unstable case of the Idaho Falls study.

In this chapter, we evaluate the performance of the mixed-wake model with field data collected next to a real world roadside barrier to answer the question: Can a model developed with data from controlled experiments conducted with well-characterized sources and meteorology be used to estimate the impact of a road-side barrier next to a multilane highway on which the magnitudes of the distributed sources are highly uncertain?

Section 2.2 describes the field study that was conducted to examine the effects of a roadside solid barrier on dispersion of traffic-related air pollution. Section 2.3 explains the results of the field study. In section 2.4, I describe the development of two barrier models. The performance of the developed models are evaluated against the observed concentrations and sensitivity analysis is conducted in section 2.5.

## **2.2 Field study**

### **2.2.1 Site description**

A field study was conducted adjacent to CA-60, U.S. Interstate 215 (I-215) freeway in Riverside, California. The highway has a barrier section located on the University of California, Riverside campus (Figure 2-3). The freeway has average traffic flow rate of 200,000 vehicles/day. The meteorological data collected from UC Riverside Meteorological

Station, which is 1 km away from the barrier site, indicates a dominant wind from west/southwest during the daytime. Thus, the wind blows close to perpendicular to the freeway during the daytime, which makes it convenient to study barrier effects during daytime unstable conditions. During the night, the wind blows from east, and the barrier is located upwind of the road.



Figure 2-3- Map of the selected site. Adapted from Google Map.

The barrier, which is 3 m away from the edge of the road, is 4.5 m high and 1 km long. There are three lanes and one High Occupancy Vehicle (HOV) lane on the north bound side and four lanes and one HOV lane on the south bound side of the freeway. There is an entrance to the north bound lanes and an exit on the south bound side of the freeway. The lanes are 3.5 m wide and the median is 10 m across. The freeway is at the same level as the adjacent streets. There is no major source of pollution within a 3.5 km radius of the barrier site except the freeway. The heading of the freeway is  $140^\circ$ . Therefore, the wind direction perpendicular to the freeway is  $230^\circ$  true to north. Two parking lots are located behind the barrier, which provide convenient locations for sampling.

The largest obstacles in the parking lots downwind of the barrier are widely scattered trees. There are no other major obstacles within 170 m of the barrier. A 2-lane street, West Campus Drive, runs parallel to the freeway between the parking lots. The street is mainly used to access the parking lots and the traffic is mainly passenger cars travelling during the morning hours, 8 A.M. to 10 A.M., and in the evening, 4 P.M. to 6 P.M. Another parking lot extends for 300 m west of the freeway. There is no major obstacle in this parking lot and trees are sparser and shorter than in the eastside parking lots.

### **2.2.2 Measurements**

Ultrafine particles (UFPs) were used as the tracer in this study for several reasons. First, because they have adverse health effects, the levels of UFP concentrations next to a major highway are of public interest. Second, their concentrations next to major highways are well above background levels, and can be measured continuously with readily available instruments. Gidhagen et al. (2005) and Zhang et al. (2004) show that at the 100 m scale being considered here, deposition and coagulation play a minor role relative to turbulent dispersion in reducing particle number concentrations. Thus, UFP can be treated as a passive tracer by using particle number concentrations to characterize dispersion. One major problem with using UFP as a tracer is that UFP emission factors from vehicles are highly uncertain. Thus, it is necessary to treat the emission factor as an unknown whose value is obtained by fitting model estimates to measurements. This process is discussed in more detail in a later section.

Fifteen tests were conducted on different days and at different times of day from July 2014 to May 2015 but due to the malfunction of instruments and unfavorable meteorological

conditions, only six tests were selected for analysis. Table 2-1 shows the dates and duration of measurements. The total duration of the 6 tests is 27 hours.

Table 2-1- Overview of dates and duration of measurements.

Test	UFP measurement dates	Time of Measurement
1	07/22/2014	12:00-17:00
2	08/11/2014	20:00-23:30
3	08/18/2014-08/19/2014	20:00-00:30
4	08/19/2014-08/20/2014	20:00-01:00
5	04/07/2015	12:30-17:00
6	05/05/2015	14:00-18:30

#### 2.2.2.1 Air quality measurements

UFP number concentrations were measured using TSI Condensation Particle Counters (CPC), Model 3022A. The cutoff size of these CPCs is 7 nm. The measured concentration range was  $5 \times 10^3 - 10^5$  particles/cm<sup>3</sup>. According to the CPC manual, accuracy within this range of concentrations is  $\pm 10\%$ . The CPC concentrations were stored on custom-designed JackRabbit data loggers.

Several CPCs were used to measure background UFP concentrations and downwind UFP concentrations at several downwind distances. All CPCs were co-located for 30 minutes before starting each test to derive inter-instrument calibration factors used to adjust the data (Figure 2-4). A CPC was placed at the upwind side of the freeway (assuming that the wind is blowing WSW) to measure background UFP number concentrations. The rest of the CPCs were deployed behind the barrier (Figure 2-5). The downwind CPCs were placed at least 250 m away from the barrier edge to avoid barrier edge effects. CPC locations were

changed from one test to another to avoid any systematic bias in measurements. The background concentrations were subtracted from the downwind concentrations to estimate contributions from vehicles on the highway.



Figure 2-4- Co-location of CPCs before start of tests.



Figure 2-5- Approximate location of instruments.

#### 2.2.2.2 Meteorology

Campbell Scientific CSAT3 3-D (three dimensional) Sonic Anemometers were used to measure flow properties. These sonic anemometers record the three components of wind speed and the sonic temperature at a sampling frequency of 10 Hz. The data is processed using the method described in Kaimal & Finnigan (1994) to yield the 30-minute-averaged values of the turbulent heat flux, surface friction velocity, standard deviation of the vertical and horizontal turbulent velocities, wind speed, wind direction, temperature, and Monin-Obukhov Length. The measured data were stored on Campbell Scientific CR1000, CR3000, and CR5000 data loggers.

Two 3-D sonic anemometers were employed to measure upwind and downwind flow characteristics. A sonic anemometer was attached to a light post on the upwind side of the freeway (parking lot 30; assuming wind is WSW) at 4 m height above ground level (AGL) to capture upwind flow characteristics. The UC Riverside Community Garden is located on the west side of the anemometer, which ensured the absence of any major obstacles to upwind wind flow. Another sonic anemometer was attached to a light post 12 m away from the barrier at 4 m AGL to record flow characteristics behind the barrier (Figure 2-6).

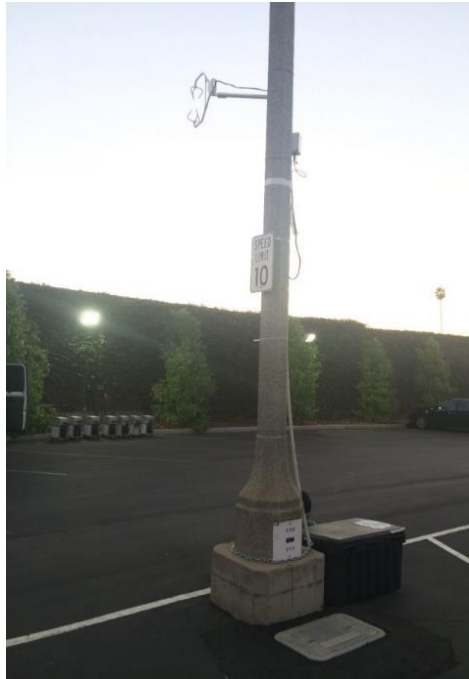


Figure 2-6- Sonic anemometer attached to a light post behind the barrier.

### **2.2.2.3 Traffic activity**

The number of cars passing each lane of the freeway was downloaded from the CalTrans Performance Measurement System<sup>1</sup>. The detectors record the number of cars and trucks separately.

## **2.3 Experimental results**

The air quality data, micrometeorological data, and traffic data were averaged over 30-minute periods for analysis. In this section, these observed data are discussed.

### **2.3.1 Air quality**

Figure 2-7 shows the time-series of UFP number concentrations measured at upwind and downwind at 13 m and 101 m between 4 pm and 5 pm of test 6. Background

---

<sup>1</sup> [www.pems.dot.ca.gov](http://www.pems.dot.ca.gov)

concentration remained almost constant indicating that the background location is not affected by any source of air pollution. The concentrations measured downwind of the barrier were clearly greater than background concentrations and the concentrations measured closer to the barrier were highest.

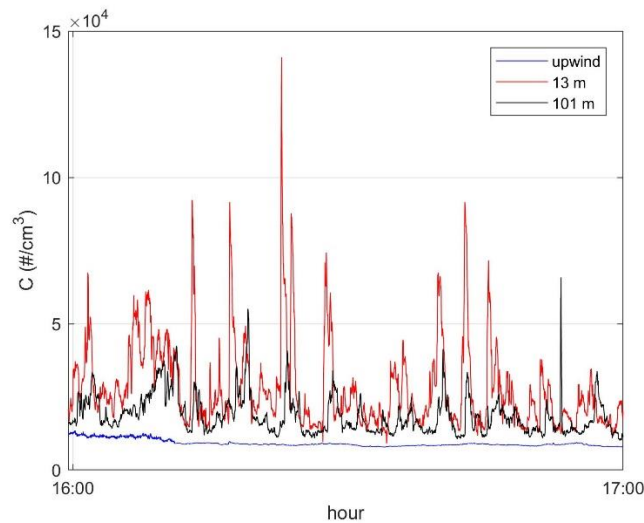


Figure 2-7- Time series of UFP number concentrations between 4 pm and 5 pm of test 6.

The background concentrations were subtracted from the downwind concentrations in analyzing the UFP concentrations. The background concentration was around  $10^4$  #/cm<sup>3</sup>. Figure 2-8 shows the spatial distributions of the averages over the concentrations measured in the six tests. The concentrations always decrease with distance behind the barrier and do not show the peak away from the barrier observed by Ning et al. (2010). We next examine whether these concentration measurements can be described with a dispersion model that was evaluated with data from controlled experiments conducted in the wind tunnel (Heist et al., 2009) and in the tracer field study (Finn et al., 2010).

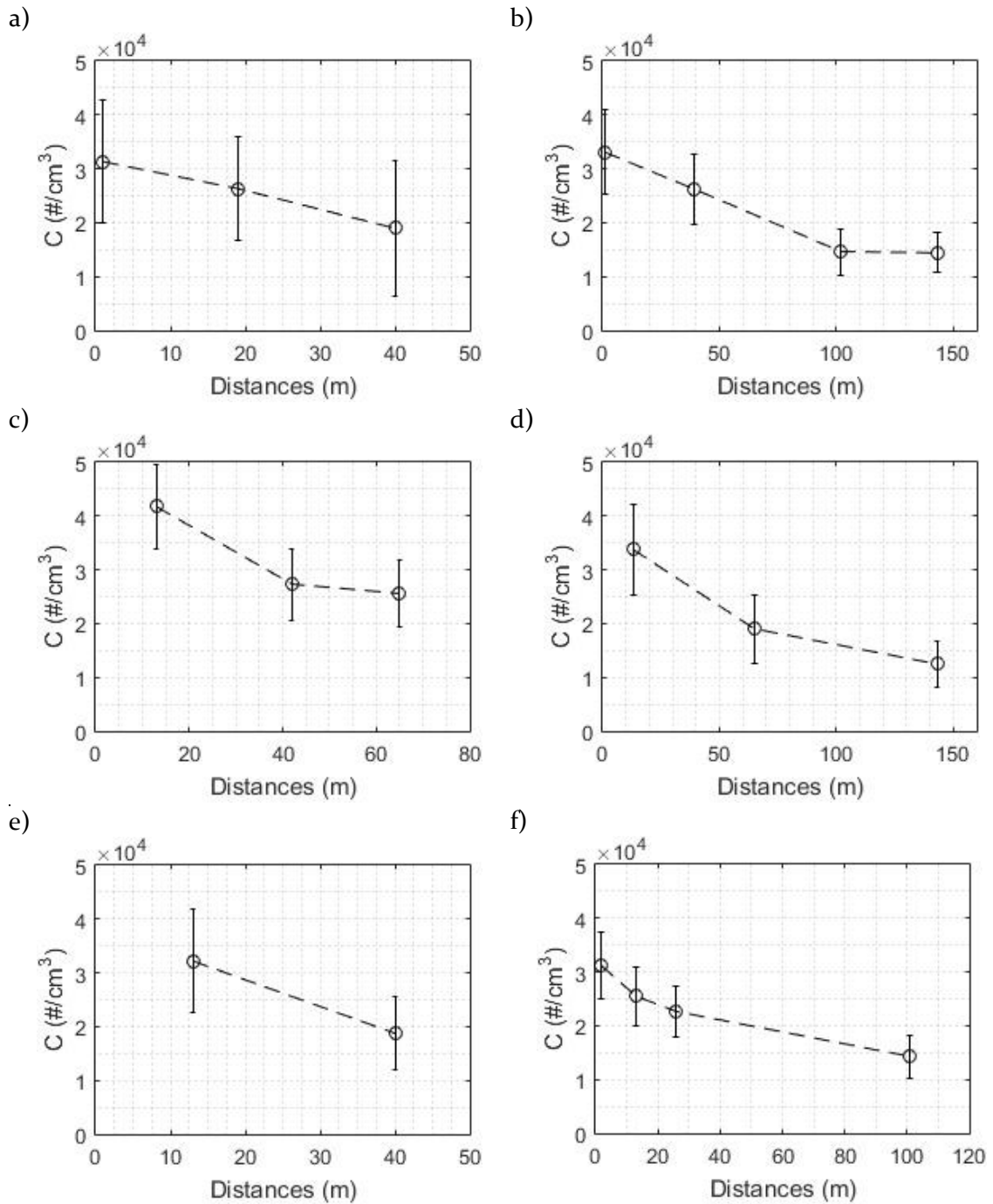


Figure 2-8- Averaged particle concentrations at different distances behind the barrier for a) Test 1, b) Test 2, c) Test 3, d) Test 4, e) Test 5, and f) Test 6.

### 2.3.2 Meteorology

The wind direction during all the tests was within 45° of perpendicular to the freeway. The observed wind rose of all tests measured by the upwind sonic anemometer is shown in Figure 2-9. The wind direction perpendicular to the freeway is 230° true to north. The meteorological data measured by the UCR meteorological station were consistent with the on-site sonic anemometer data, which indicated that the upwind anemometer was not affected by local obstacles.

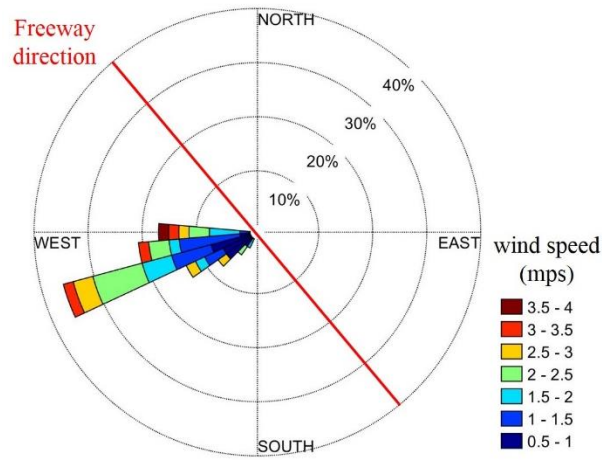


Figure 2-9- Observed wind rose measured by the upwind 3-D sonic anemometer along with freeway direction.

In addition, the effect of solid barrier on turbulence levels was investigated. Comparison between the wind speed measured by the downwind sonic anemometer and that measured by the upwind sonic anemometer showed that the wind speed decreases downwind of the solid barrier by 64% (Figure 2-10a). Since top of the solid barrier is a source of turbulence, it is expected that the turbulence levels downwind of the barrier at the barrier height be greater than those observed upwind of the road. The standard deviation of vertical velocity fluctuations ( $\sigma_w$ ) downwind of the barrier was observed to be greater than that

upwind of the freeway by 60% (Figure 2-10b). These results are consistent with the observations in the wind tunnel study (Heist et al., 2009).

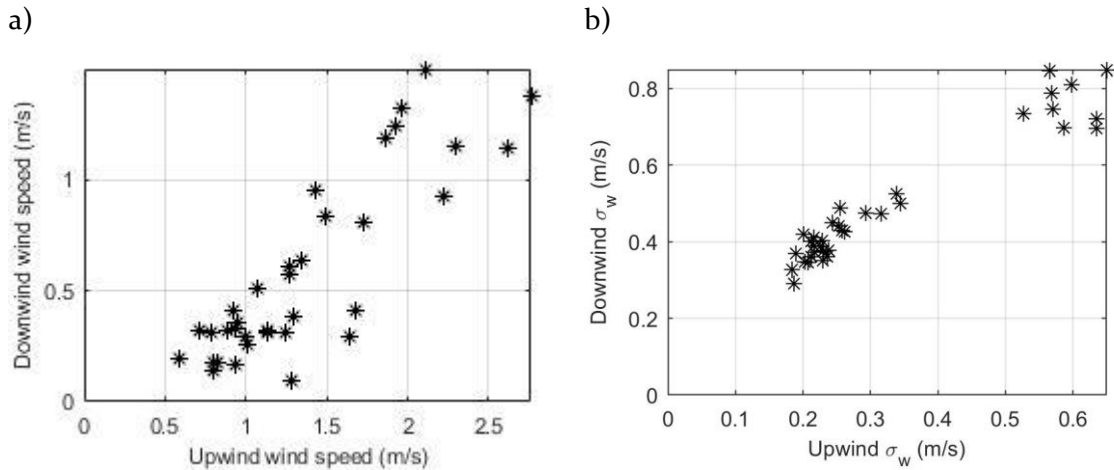


Figure 2-10- Comparison of observed a) wind speed and b) standard deviation of vertical velocity fluctuations ( $\sigma_w$ ) downwind of the barrier against upwind of the freeway.

The meteorological conditions used to analyze the data correspond to the upwind 3-D sonic anemometer, which are shown in Table 2-2.

Table 2-2- Meteorological conditions.

Test	# of data points	Mean Monin-Obukhov Length (m)	Mean Wind Direction (deg true N)	Mean Wind Speed ( $ms^{-1}$ )	Mean Friction Velocity ( $ms^{-1}$ )	Cloud Cover
1	10	-11.5	254°	2.72	0.31	Clear
2	7	-15.7	256°	1.37	0.17	Clear
3	9	-9.1	238°	1.00	0.14	Clear
4	10	-5.8	254°	1.14	0.14	Clear
5	9	-38.8	238°	2.45	0.44	Mostly Cloudy
6	9	-43.0	268°	2.83	0.47	Partly Cloudy

Tests 1 through 4 were conducted in unstable conditions. Winds were moderate during test 1 and very light during tests 2, 3, and 4. No major variability in wind direction was

observed during the first 4 tests and the wind directions were almost always favorable with respect to the freeway orientation. Skies were clear during the first 4 tests.

Notice that the surface boundary layer was unstable even during tests 2, 3, 4, which were conducted in the late evening and night when the sun had set. Tests 5 and 6 were conducted in near neutral conditions. Winds were moderate and the wind direction was steady. Wind directions were almost always favorable during these two tests. Skies were mostly cloudy in test 5 and partly cloudy in test 6.

## 2.4 Framework for the barrier models

We developed two models to explain the collected data. The developed models assume that the mixed-wake region behind the barrier results in constant concentrations from surface to the barrier height. These models are based on equation 2-8.

### 2.4.1 Simple barrier model

We can derive a simplified version of equation 2-8 by using the neutral expression for the product of the effective wind speed and  $\sigma_z$  (Venkatram et al., 2013):

$$U(\bar{z}) \cos \theta \sqrt{\frac{\pi}{2}} \sigma_z = 0.57 * \sqrt{\frac{\pi}{2}} u_* x = 0.71 u_* x \quad (2-10)$$

where  $u_*$  is the surface friction velocity and  $x$  is the distance of a receptor from the barrier.

Equation 2-8 then becomes:

$$C_s = \frac{q}{U\left(\frac{H}{2}\right) \cos \theta H + a u_* x} \quad (2-11)$$

where  $a$  is 0.71.

Since the width of the road is comparable to the downwind distances being considered here, we treat the road as an area source with width  $W$ . Then, the concentration at a downwind distance  $x$  from the barrier becomes:

$$C_s = \int_x^{x+W} \frac{\frac{q}{W}}{U \left(\frac{H}{2}\right) \cos \theta H + au_* x} dx$$

$$= \frac{q}{au_* W} \ln \left( 1 + \frac{W}{H \frac{U \left(\frac{H}{2}\right) \cos \theta + x}} \right) \quad (2-12)$$

This simple model, which applies primarily to neutral conditions, serves as a reference model whose performance against observations will be compared with that of an improved version.

#### 2.4.2 Modified mixed-wake model

The second model considered here modifies equation 2-8 to improve its performance during unstable conditions when this equation overestimates concentrations close to the source in the Idaho Falls tracer experiment (Finn et al., 2010). As shown in Figure 2-11, the modified model assumes that the maximum concentration occurs above barrier height to be consistent with the wind tunnel data (Heist et al., 2009).

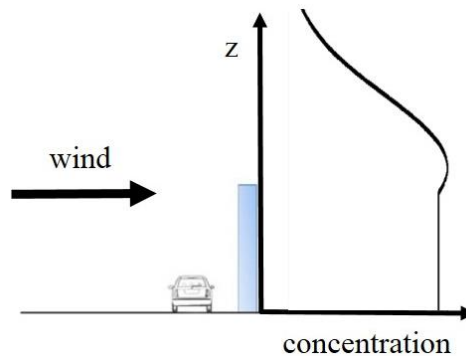


Figure 2-11- Schematic of concentration profile in the modified mixed-wake model.

The second modification is an entrainment factor,  $f_m$ , that reduces entrainment into the barrier wake during unstable conditions. This is an empirical modification to account for the overestimation of concentrations close to the source under the unstable conditions of the Idaho Falls experiment. The factor reduces entrainment behind the barrier as the absolute value of the Monin-Obukhov length decreases. It is also a function of downwind distance, starting at values below unity just downwind of the barrier and approaches unity at large downwind distances.  $f_m$  is taken to be:

$$f_m = f_c + (1 - f_c) \left( 1 - \exp\left(-\frac{x}{L_s}\right) \right) \quad (2-13)$$

where  $f_c$ , the entrainment factor at  $x = 0$ , is taken to be:

$$f_c = \exp\left(-\frac{L_s}{|L_{MO}|}\right) \quad (2-14)$$

where  $L_s = 10H$  and  $H$  is the barrier height.  $f_c$  decreases as the absolute value of Monin-Obukhov length decreases.

The third modification is the effect of barrier on surface friction velocity. Surface friction velocity is enhanced based on an empirical model for the development of a neutral boundary layer after a roughness change,

$$u_{*w} = u_* \left( \frac{z_{0w}}{z_0} \right)^{0.17} \quad (2-15)$$

where the effective roughness of the wall is taken to be  $z_{0w} = H/9$ .

Assuming that the barrier does not modify the upwind heat flux, the Monin-Obukhov length is taken to be proportional to  $u_*^3$ . Then, the Monin-Obukhov length behind the barrier is:

$$L_w = L_{MO} \left( \frac{u_{*w}}{u_*} \right)^3 \quad (2-16)$$

The velocity below the barrier height is assumed to be uniform with height given by its value at  $z = H$ . With these parameterizations, the surface concentration can be expressed as

$$C_s = f_m C_{max} [\exp(-p_1^2) + \exp(-p_2^2)] \quad (2-17)$$

where  $C_{max}$  is the maximum concentration is

$$C_{max} = \frac{\frac{q}{\cos \theta}}{f_m U(H) \cdot H \cdot [\exp(-p_1^2) + \exp(-p_2^2)] + U(z) \sqrt{\frac{\pi}{2}} \sigma_z \cdot [2 - \text{erf}(p_1) - \text{erf}(p_2)]} \quad (2-18)$$

In this equation,  $U(H)$  is the velocity at barrier height,  $p_1 = (H - H_p)/\sqrt{2}\sigma_z$ ,  $p_2 = (H + H_p)/\sqrt{2}\sigma_z$ , and  $H_p$  is the height of maximum concentration, taken to be:

$$H_p = H + \frac{\sigma_{zB}}{2} \quad (2-19)$$

where  $\sigma_{zB}$  is the vertical plume spread right behind the barrier. This model performs better than the model presented in Schulte et al. (2014) in describing concentrations close to the barrier in the Idaho Falls experiment (Finn et al., 2010) during unstable conditions, which correspond to those considered in the current field study.

## 2.5 Comparison with observations

As indicated earlier, the UFP number emission factor is highly uncertain. The literature reports a large range  $10^{12} \sim 10^{14} \# / (\text{veh.km})$  (Kumar et al., 2011; Morawska et al., 2008). In this study, we treat the emission factor as an unknown parameter whose value is obtained by fitting model estimates to measured UFP concentrations. Because we wanted to evaluate the performance of the model in describing the impact of the barrier on downwind concentrations, we excluded data points at distances less than 40 m from the barrier in deriving the emission factor.

The ratio of UFP High Duty Vehicle (HDV) emission factor to that of Light Duty Vehicle (LDV) was taken to be 25. This ratio was found using  $PM_{2.5}$  emissions from the EMFAC Model inventory data (California Air Resources Board, 2011). Car and truck emission factors were averaged over mileage for the fleet operating in Riverside County.

For the simple barrier model, the fitted emission factor is  $7.90 \times 10^{13}$  #/(veh.km) averaged over the six tests and a standard deviation of  $2.88 \times 10^{13}$  #/(veh.km). The corresponding statistics for the modified mixed-wake model are a mean of  $7.09 \times 10^{13}$  #/(veh.km) and a standard deviation of  $2.56 \times 10^{13}$  #/(veh.km). The mean emission factors of both models lie within the range reported in literature (Kumar et al., 2011; Morawska et al., 2008).

The performance of the models are evaluated using the geometric mean ( $m_g$ ), standard deviation of the residuals between the observations and predictions ( $s_g$ ), the fraction of data points that lie within a factor of two of the observations (fact2), and the correlation coefficient between the observations and predictions ( $r^2$ ). The geometric mean and standard deviation are defined as:

$$\ln m_g = \sum_i \frac{\epsilon_i}{N} \quad (2-20)$$

$$\ln s_g = \sqrt{\frac{\sum_i (\epsilon_i - \ln m_g)^2}{N - 1}} \quad (2-21)$$

where  $\epsilon = \ln C_{obs.} - \ln C_{pred.}$  is the residual between the observed concentration and the predicted one, and  $N$  is the number of data points.

The performance of the models using the average emission factor for the six tests is shown in Figure 2-12. The  $r^2$  are similar for the two models using a barrier height of 4.5 m.

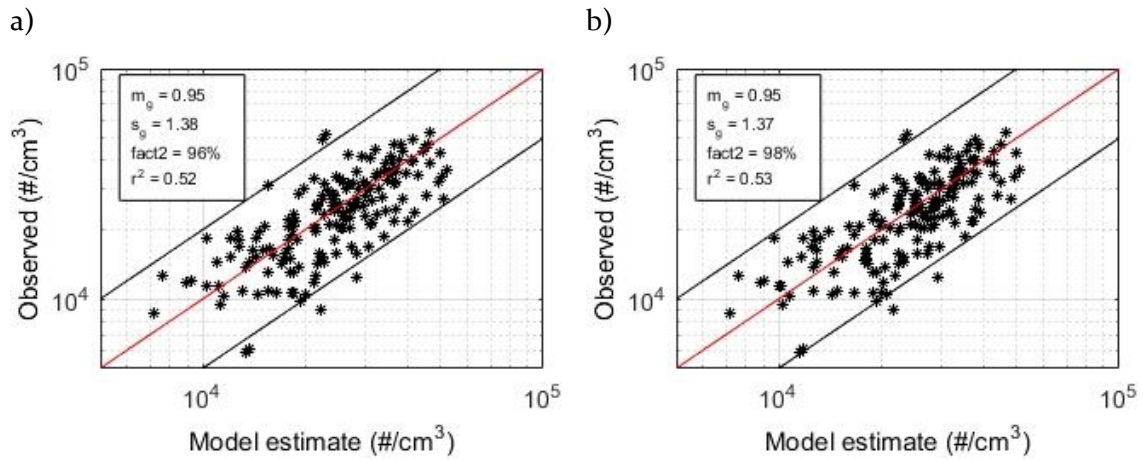


Figure 2-12- Comparison of observations and a) simple barrier model estimates and b) the modified mixed-wake model estimates.

To distinguish between the two models, we investigated the sensitivity of model performance to different barrier heights using fractional bias (Chang and Hanna, 2004) to measure their relative performance. Figure 2-13 shows the fractional bias versus barrier heights for both models. The bias is close to zero for both models when the barrier height is close to its actual value of 4.5 m, which indicates that both models capture the essential effects of barriers on downwind concentrations. The simpler barrier model is more sensitive to barrier height, reflecting the role of this variable in its formulation. It would be necessary to conduct experiments with varying barrier heights to check whether this sensitivity is real.

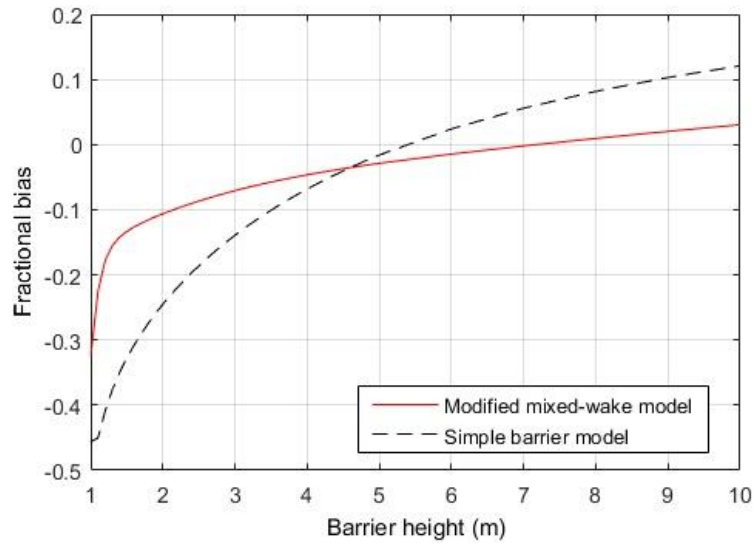


Figure 2-13- Fractional bias versus barrier height for modified mixed-wake model (red solid line) and for simple barrier model (black dashed line).

Figure 2-14, which compares measured concentration gradients with model estimates from test 3, the day with the lowest wind speed, test 4, the most convective day, and test 6, the most neutral day, indicates that both models provide a realistic depiction of the gradients over a wide range of stabilities.

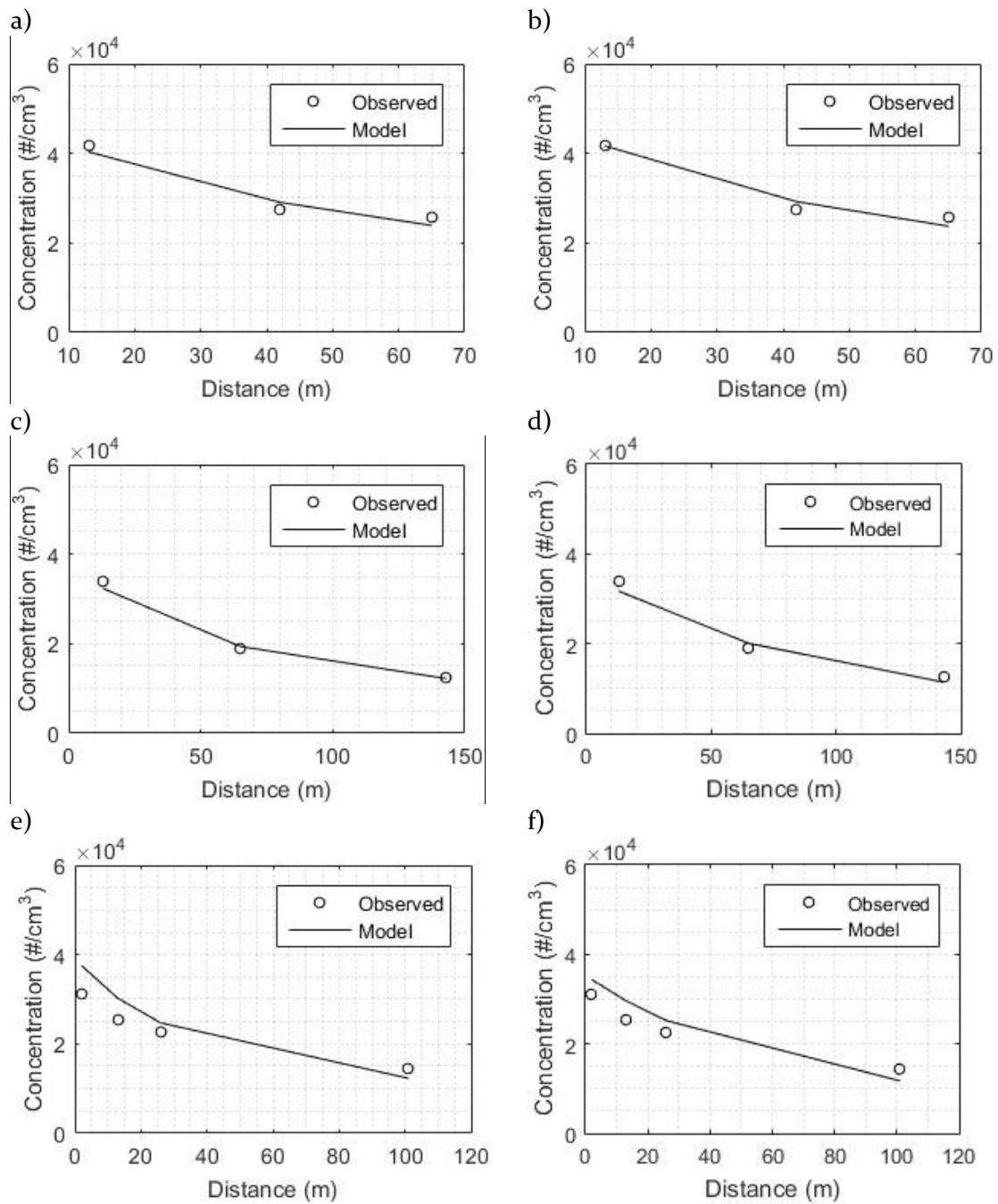


Figure 2-14- Concentration gradients for observations and a) simple barrier model for test 3, b) the modified mixed-wake model for test 3, c) simple barrier model for test 4, d) the modified mixed-wake model for test 4, e) simple barrier model for test 6, and f) the modified mixed-wake model for test 6. (Emission factors are calculated for each day using the data measured beyond 40 m from the barrier.)

Because the wind directions during all the tests were within 45° perpendicular to the freeway, we cannot quantify the performance of the model when the wind direction is close to parallel to the road.

Figure 2-15 shows the spatial variation of the ratio of UFP concentrations in the presence of a barrier to those in the absence of the barrier as a function of barrier height; the micro-meteorological inputs correspond to test 6. In the simpler model, the no-barrier concentrations were estimated by treating the vehicles on the freeway as a 1 m barrier. The concentrations in modified mixed-wake model were estimated by assuming that the vehicles induce an initial vertical spread of 1 m. The concentration reduction, relative to the no-barrier concentration, just next to the 4 m barrier is 50-60%. This reduction increases to 65-75% by doubling the barrier height. The concentration reduction decreases with distance to about 25% at 40 m for the 4 m barrier. This reduction is 45% for the 8 m barrier. The average concentration reduction from 0-40 m is around 35% for a 4 m barrier. This average reduction increases to 55% with a doubling of the barrier height to 8 m.

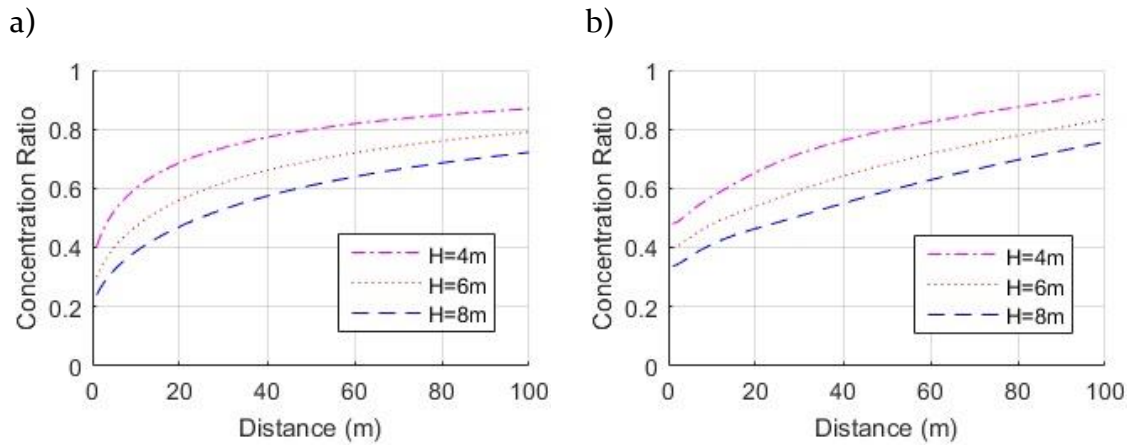


Figure 2-15- Comparison of estimated normalized concentrations, to no-barrier case, behind barriers with different heights for a) simple barrier model and b) the modified mixed-wake model.

## 2.6 Summary and conclusions

We used data from a field study to evaluate a dispersion model that parameterizes the effects of roadside barriers on dispersion. This model was developed using data from experiments conducted in the wind tunnel and measurements from a tracer study in which concentrations were sampled simultaneously downwind from two line sources, one behind a 6 m barrier and the other located in open terrain. The primary question this paper addresses is whether a semi-empirical dispersion model based on data from controlled experiments can be used to interpret data collected downwind of a sound barrier next to a real-world urban highway with distributed sources whose magnitudes are uncertain.

Six tests were conducted next to a congested freeway, which had several factors that aided the interpretation of the data: 1) absence of a major source of pollution, except the freeway, in the neighborhood, 2) absence of a major obstacles on the east and west sides of the freeway, except the noise barrier, 3) absence of a busy street behind the barrier, 4) presence of a single barrier downwind of the freeway, and 5) presence of parking lots on

both sides of the freeway to provide the opportunity to place several CPCs to measure UFP concentrations.

Two models were evaluated with the data from the field study. The first is a simplified version of model presented in Schulte et al. (2014), which assumes neutral conditions. The second is a modification of the model described in Schulte et al. (2014) to account for reduced entrainment in the immediate wake of the barrier during unstable conditions. Both models performed well in estimating the pollutant concentrations. Because the emission factor for UFP is highly uncertain, we treated it as a model parameter whose value was obtained by fitting model estimates to observations of UFP concentrations measured at distances where the barrier impact is small. The emission factors were found to have a mean of  $7.90 \times 10^{13}$  #/(veh.km) and a standard deviation of  $2.88 \times 10^{13}$  #/(veh.km) for the simple barrier model and a mean of  $7.09 \times 10^{13}$  #/(veh.km) and a standard deviation of  $2.56 \times 10^{13}$  #/(veh.km) for the modified mixed-wake model for all of the six tests. These values are well within the range reported in the literature (Kumar et al., 2011; Morawska et al., 2008).

Both models provide adequate estimates of the magnitudes and the spatial variation of near-road concentrations associated with vehicle-related emissions. The models were evaluated under unstable conditions when exposure to vehicle emissions is likely to be the highest for people living close to highways. Their applicability to stable conditions, when near-road concentrations are relatively high, has not been evaluated. The models have also not been tested when the wind direction departs significantly from normal to the road.

The models predict that a 4 m barrier results in a 35% reduction in average concentration within 40 m (10 barrier heights) of the barrier, relative to the no-barrier site. This concentration reduction is 55% when the barrier height is doubled. The good

performance of the simple barrier model reinforces the conclusion from Schulte et al. (2014) that the primary impact of the barrier is equivalent to shifting the line sources on the road upwind by a distance of about  $HU/u_*\cos\theta$ .

# 3 Effect of Vegetation Barriers on Dispersion from Roads

## 3.1 Introduction

Vegetation barriers have been suggested as a potential strategy to mitigate the near-road air pollution. However, there is still a debate among scientists on the effects of vegetation on concentrations downwind of roadways. Some field studies have shown that presence of a vegetation barrier or adding vegetation to an existing solid barrier results in concentration reduction downwind of the barrier. For example, a field study in Guildford (Surrey, UK) showed that presence of a 2.2 m wide vegetation results in a 37% reduction of particles with 5 – 560 nm size range under cross-road wind conditions (Al-Dabbous and Kumar, 2014). Baldauf et al. (2008) observed in a field study in Raleigh, NC that adding vegetation to a solid barrier further lowers PM number concentrations downwind of the barrier. The same observation was reported for PM<sub>2.5</sub> and UFP by Lee et al. (2018) and Ahangar et al. (2017a), who compared UFP and PM<sub>2.5</sub> concentrations downwind of a solid barrier with those of a combination of solid-vegetation barrier. Another field study in Detroit, MI showed that presence of vegetation results in 12% reduction in concentration of

Black Carbon (BC); however, it does not change the particle counts in the fine and coarse particle size range (0.5 – 10  $\mu\text{m}$  aerodynamic diameter) (Brantley et al., 2014).

On the other hand, some researchers have reported an increase in downwind concentrations in the presence of a vegetative barrier next to a road. For example, Tong et al. (2015) measured higher  $\text{PM}_{2.5}$  concentrations downwind of trees due to decreased Turbulent Kinetic Energy (TKE). However, they claimed that deposition obscures the dominant effect of aerodynamics on local concentrations. In another field study, the impacts of evergreen and deciduous trees on near road air quality were examined in North Carolina, USA (Hagler et al., 2012) and it was concluded that vegetation can result in higher, lower, or the same concentrations as in the section without a barrier. The observations of Hagler et al. (2012) were analyzed in another study that found vegetation barriers with full foliage reduce UFP and CO concentrations by 37.7 – 63.6% and 23.6 – 56.1%, respectively and vegetation barriers with reduced foliage showed no significant change in UFP concentration before and after the barrier (Lin et al., 2016).

Many modeling studies have been conducted to simulate the effects of vegetation barriers on urban air quality. These studies are also as inconclusive as field studies. Steffens et al. (2012) incorporated particle aerodynamics and deposition mechanisms into the Comprehensive Turbulent Aerosol Dynamics and Gas Chemistry (CTAG) model and examined the effects of vegetation on near-road air quality by comparing the model results against the Chapel Hill, NC dataset developed by Hagler et al. (2012). Their model assumed that vegetation barriers affect the flow field and concentration patterns in three ways: 1) they increase vertical mixing by lofting some of the particles, 2) they lower wind speed and lower turbulence behind the vegetation barrier, and 3) they remove some particles by dry

deposition. The equation governing the TKE included a source term corresponding to the creation of TKE by tree elements, and a sink term, which results from the drag due to vegetation. Their model showed adequate agreement with concentrations of particles larger than 50 nm, but tended to overpredict concentrations of particles less than 50 nm behind a vegetation barrier. Tong et al. (2016) developed a model by incorporating Large Eddy Simulation (LES) into the CTAG model and evaluated model performance against the dataset developed by Hagler et al. (2012). Then, they compared common vegetation barrier configurations near roadways to find the most effective configurations to provide mitigation of highway emissions. They concluded that a wide vegetation barrier with high Leaf Area Density (LAD), and also vegetation-solid barrier combinations work best as mitigation strategies.

Ghasemian et al. (2017) developed a CFD model to estimate concentrations downwind of the roadside solid and vegetation barriers. They first evaluated the model by comparing the estimated concentrations downwind of a solid barrier against the results of the wind tunnel study (Heist et al., 2009). After validation of the numerical methodology, concentrations downwind of vegetation barriers with different LADs were estimated. They found that dense canopies behave similar to the solid barriers and mitigate the pollutant concentrations; while high porosity canopies reduce wind speed and increase pollutant concentrations. While these results are qualitatively consistent with the results from the wind tunnel, the CFD model was unable to describe the measured vertical profiles of concentrations downwind of the vegetative barrier.

This chapter investigates the effects of vegetative barriers on near-road air quality by using a semi-empirical dispersion model to interpret results from the wind-tunnel

experiment conducted to compare the effects of vegetation and solid barriers on concentrations near roadways. This interpretation relies on dispersion models that describe the two effects independently: 1) enhancement of vertical dispersion, and 2) reduction of turbulence levels downwind of the barrier. The comparison of the observed concentrations with results from these models provides insight into the relative roles of these counteracting effects as a function of distance from the vegetative barrier. This analysis has not yet resulted in a model that provides a satisfactory description of the measured vertical profiles of concentrations.

The details and the results of the wind tunnel experiment are described in section 3.2 and the analysis of the collected data is described in section 3.3.

## **3.2 Wind tunnel experiments**

### **3.2.1 Experiment description**

US EPA researchers performed a wind-tunnel study to examine the effects of vegetative barriers on dispersion of roadway-emitted pollutants using EPA's Fluid Modeling Facility meteorological wind tunnel (Snyder, 1979). The wind tunnel test section is 3.7 m wide, 2.1 m high, and 18.3 m long. The boundary layer used in this experiment was designed to simulate flow in an urban area. To condition and maintain the boundary layer, the floor of the test section was covered with roughness blocks, aligned in lateral rows (Figure 3-1).

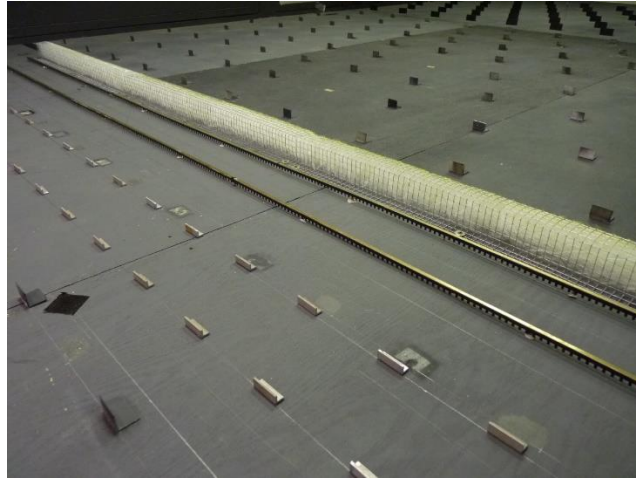


Figure 3-1- Illustration of line sources, roughness blocks, and filter material representing vegetation (view from upwind).

Roadway emissions were modelled using two line sources at 1:150 scale. The basic length scale used to non-dimensionalize distances in the results presented in this chapter is denoted by  $H$  with a full-scale equivalent of 6 m. The lengths of the model line sources were 2.73 m i.e. full-scale equivalent length of 410 m. The line sources were located at  $x = \pm 1.65H$ , assuming that the origin is located at the middle of the line sources, with  $x$  positive in the streamwise direction,  $y$  along the axis of the roadway, and  $z$  vertically upward. Three different cases were studied, a flat terrain case, a full-scale 9 m high solid barrier case (i.e.  $1.5H$ , assuming  $H = 6\text{ m}$ ), and a full-scale 9 m  $\times$  9 m vegetative barrier case. Vegetation was simulated by using a filter material. The heights of the barriers are denoted by  $H_w$ , which correspond to the full-scale value of 9 m.

Laser Doppler Velocimetry (LDV) was used for all velocity measurements in this study, details of which are described in Heist et al. (2009). The air speed in the section was fixed at 2.98 m/s ( $U_r$ ) at a full-scale equivalent height of 30 m.

The line sources emitted ethane as tracer gas with total emission rate  $Q = 1.87 \text{ gr/min}$  at a full-scale equivalent height of  $1.5 \text{ m}$  above the ground and were placed perpendicular to the air flow. Ethane was emitted from small holes with  $0.1 \text{ cm}$  diameter that were spaced  $1 \text{ cm}$  apart on the bottom side of each source bar. To simulate the vehicle-induced turbulence, tabs were mounted on the upwind side of each hole. The tabs were  $0.3 \text{ cm}$  wide and protruded  $0.5 \text{ cm}$  below the source bar (Figure 3-2). All samples were drawn through Rosemount Model 400A hydrocarbon analyzers. The concentrations of ethane were normalized to give the non-dimensional concentration  $\chi = CU_r/(Q/L_xL_y)$ , where  $C$  is the mass concentration with background concentration subtracted,  $Q$  is the total emission rate ( $1.87 \text{ gr/min}$  of ethane),  $L_x$  is the alongwind dimension of the roadway segment ( $24 \text{ cm}$ ,  $36 \text{ m}$  full scale), and  $L_y$  is the lateral length of the source segment ( $273 \text{ cm}$ ,  $410 \text{ m}$  full scale).

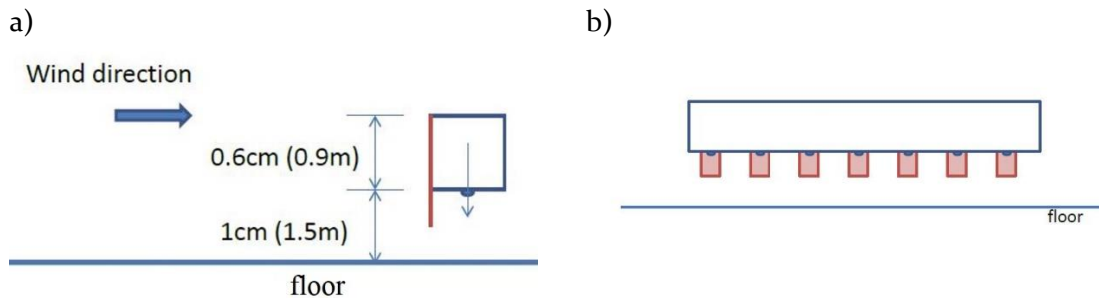


Figure 3-2- Schematic of the line sources in the wind tunnel study; a) looking crosswind, and b) looking upwind.

The barriers started at  $x = 3H$  and were as long as the line sources. The vegetation was extended to  $x = 4.5H$ . Due to its thickness, optical porosity of the porous barrier is close to zero. Turbulence statistics and concentrations were measured at several downwind distances along the centerline of the sources. The static pressures right before and after the vegetation were measured, too. The static pressure drop over the porous media was used to estimate the screen pressure coefficient:

$$\lambda = \frac{\Delta p_{st}}{\frac{1}{2}\rho u^2 d} \quad (3-1)$$

where  $\Delta p_{st}$  is the static pressure drop over the porous media,  $\rho$  is the air density,  $u$  is the mean wind speed, and  $d$  is the streamwise thickness of the filter material. The measurements showed that  $\lambda = 2 \text{ m}^{-1}$  for the filter material. The screen pressure coefficient can be related to the bulk drag coefficient using the following equation (Raupach et al., 2001):

$$C_d = \frac{\Gamma_{b1}\lambda}{\lambda + \Gamma_{b1}\lambda_1} \quad (3-2)$$

where  $\Gamma_{b1}$  is the bulk drag coefficient for a solid fence here taken as  $\Gamma_{b1} = 1.07$  according to (Jacobs, 1983) and  $\lambda_1 = 1.5$  is the empirical constant. Using  $\lambda = 2 \text{ m}^{-1}$  in this equation results in  $C_d = 0.6$ .

### 3.2.2 Experimental results

Wind tunnel measurements of three different cases can provide a useful dataset to examine the effects of vegetation and solid barriers on near-road air quality. In fact, observations in presence of vegetation with low porosity are expected to approach the observations in presence of a solid barrier, and that of vegetation with high porosity to approach the observations in flat-terrain case.

#### 3.2.2.1 Impact of vegetation and solid barriers on the flow field

The roughness length ( $z_0$ ), the friction velocity ( $u_*$ ), and the displacement height ( $dh$ ) were assessed by fitting the standard logarithmic velocity profile to the undisturbed boundary layer so that the computed friction velocity matched the value found from the

constant turbulent shear stress region, i.e. from  $z = 12 \text{ m}$  to  $z = 30 \text{ m}$  full-scale (Heist et al., 2009):

$$U(z) = \frac{u_*}{\kappa} \ln\left(\frac{z - dh}{z_0}\right) \quad (3-3)$$

where  $\kappa$  is the von Karman constant, and was taken to be 0.4.  $u_*$  and  $z_0$  were found to be  $0.25 \text{ m/s}$  and  $0.27 \text{ m}$ , respectively.

Contours of the observed velocity magnitudes as well as the velocity fields in vegetation and solid barrier cases are shown in Figure 3-3. The velocity behind barriers in both cases decreases substantially. A strong recirculation zone is formed behind the solid barrier which extends to a point between  $4H_w$  and  $8H_w$  from the barrier with a reverse velocity as strong as a third of the reference velocity. A significant upward deflection in upstream airflow is observed in the solid barrier case.

On the other hand, a low-air-speed zone is observed behind the vegetative barrier in which a reverse velocity is not detected. Thus, no recirculation zone forms behind the vegetation. A slight upward deflection in upstream airflow is observed. The TKE behind the vegetation barrier is measured to be smaller than that of the solid barrier because of the formation of a recirculation zone behind the solid barrier. The CFD simulations (Ghasemian et al., 2017; Steffens et al., 2012; Tong et al., 2015) are consistent with these measurements.

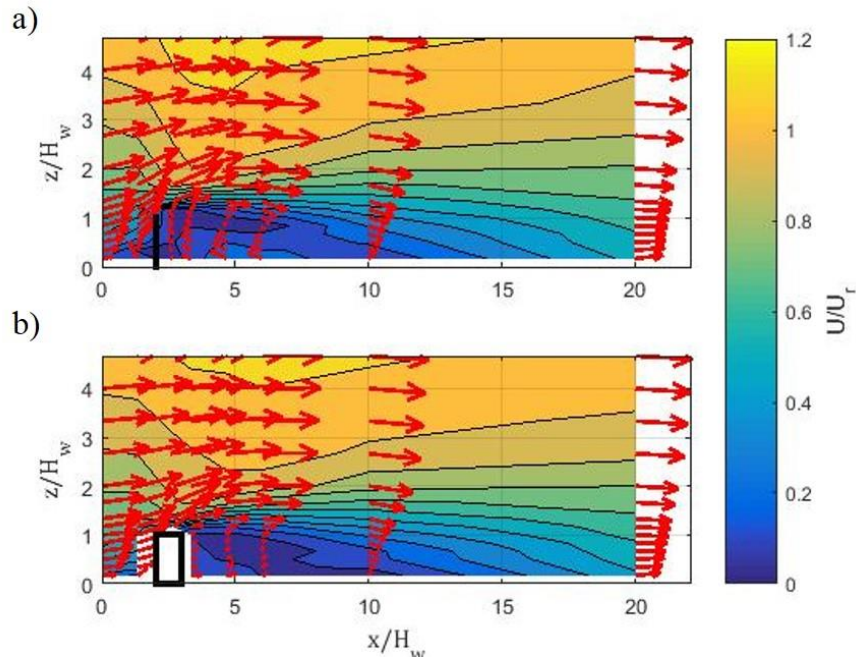


Figure 3-3- Magnitudes of observed velocity and velocity fields for a) solid barrier case and b) vegetation barrier case. Barriers are represented by black rectangles.

Turbulence levels, including longitudinal and vertical velocity fluctuations ( $\sigma_u$  and  $\sigma_w$ ) and cross-correlation of vertical and longitudinal velocities, were measured at different points above the height  $H$ . Longitudinal velocity fluctuations were also measured at heights below  $H$ .

Contours of the vertical velocity fluctuations ( $\sigma_w$ ) for solid and vegetation barriers are shown in Figure 3-4. We see that  $\sigma_w$  is highest at the center of the recirculation zone in the solid barrier case. This center is located  $4H_w$  from the barrier. It is evident that the top of the barrier acts as a zone of shear production of turbulence (Figure 3-4a).

Turbulence levels are relatively low behind the vegetative barrier because turbulence is dissipated behind the barrier. However, the top of the vegetation acts as a shear source of turbulence (Figure 3-4b). In this case, the highest turbulence level occurs at  $7H_w$  from the

leeward edge of vegetation (Figure 3-4b). It should be noted that the magnitude of the maximum  $\sigma_w$  is larger for the solid barrier case.

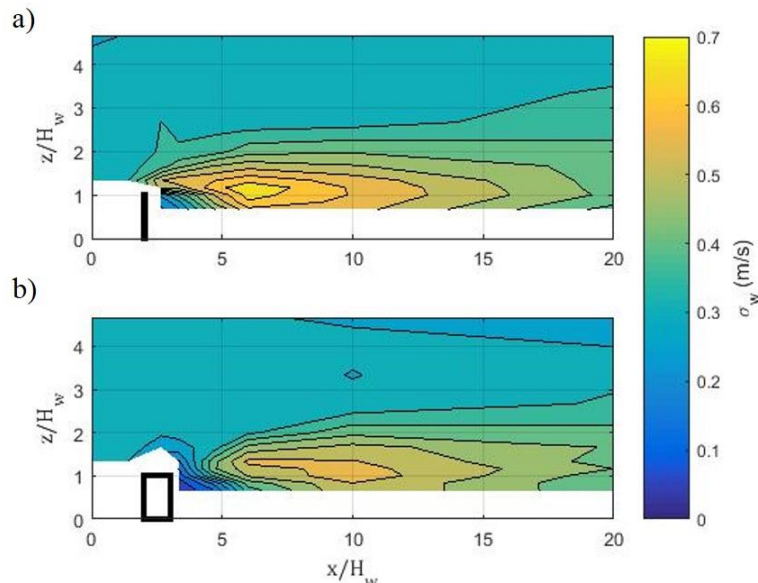


Figure 3-4- Contours of vertical velocity fluctuations for a) solid barrier case and b) vegetation barrier case. Barriers are represented by black rectangles.

Contours of longitudinal velocity fluctuations ( $\sigma_u$ ) are also shown in Figure 3-5. The overall trend of the variation of  $\sigma_u$  is similar to that of  $\sigma_w$ . Figure 3-6 shows scatterplots comparing  $\sigma_u$  with  $\sigma_w$  at all the points that both parameters were measured. The values of  $\sigma_w$  and  $\sigma_u$  in the undisturbed boundary layer are 0.3 m/s and 0.5 m/s, respectively. The two turbulence levels are correlated well for both solid and vegetation cases with correlation coefficients of  $r^2 = 0.82$  and  $r^2 = 0.69$ , respectively.

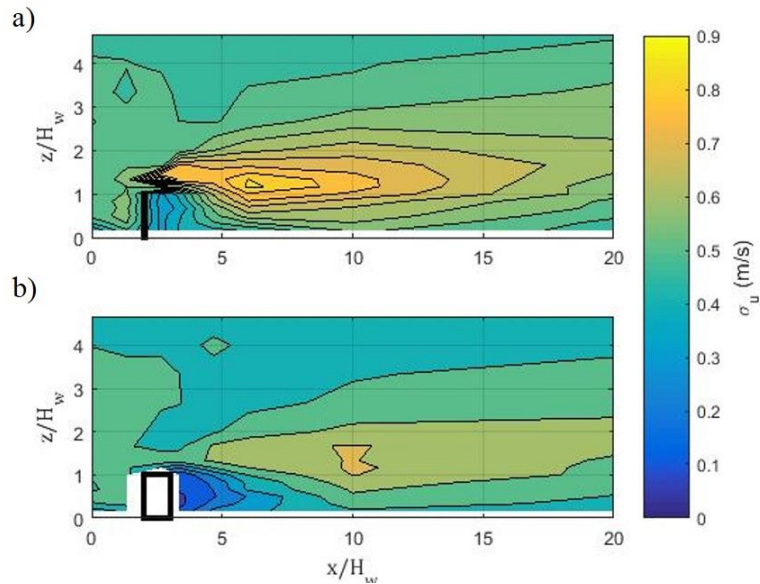


Figure 3-5- Contours of longitudinal velocity fluctuations for a) solid barrier case and b) vegetation barrier case. Barriers are represented by black rectangles.

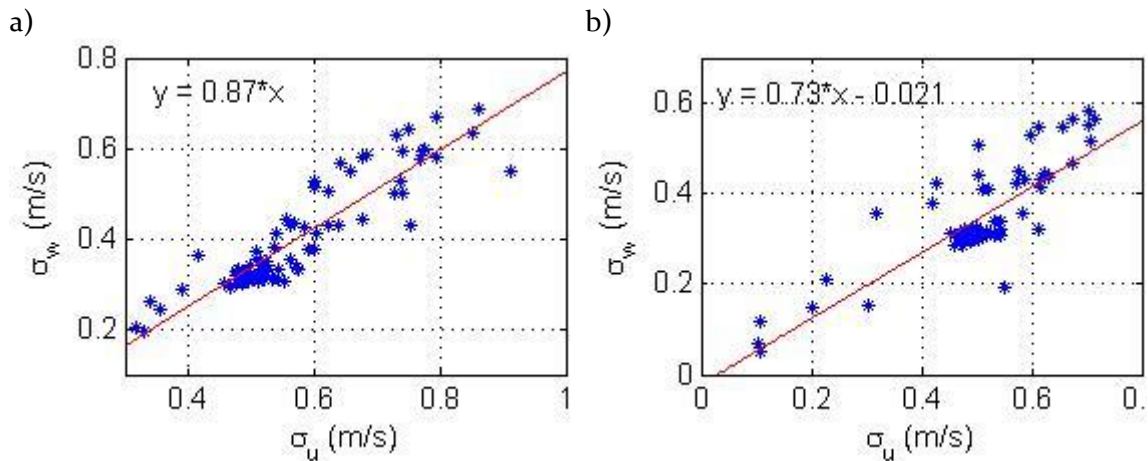


Figure 3-6- Scatterplots comparing  $\sigma_u$  values with  $\sigma_w$  values at different points within the wind tunnel for a) solid barrier case, and b) vegetation case.

### 3.2.2.2 Impact of vegetation and solid barriers on the concentration field

As discussed earlier, the concentrations were normalized to give the non-dimensional concentration  $\chi = CU_r L_x / (Q/L_y)$ . Contours of concentration fields for the 3 cases are shown in Figure 3-7. Ground-level concentrations behind the solid barrier are smaller than the corresponding concentrations in the flat terrain case (Figure 3-7b), as seen in many

previous studies (Baldauf et al., 2008; Finn et al., 2010; Hagler et al., 2011; Heist et al., 2009). Thus, solid barriers reduce ground-level concentrations downwind of the roads.

However, ground-level concentrations behind the vegetative barrier are higher than the corresponding concentrations in the flat terrain case, which suggests that the vegetative barriers can increase ground-level concentrations next to the roadways (Figure 3-7c). For example, the  $\chi = 20$  contour in vegetation case extends up to  $x = 6H_w$ , whereas that of flat terrain extends only up to  $x = 3H_w$ . On-road concentrations for solid barrier were not measured. On-road concentrations are larger in the vegetative barrier case than those in the flat terrain case. Lower air speeds on the windward side of vegetation could lead to the larger on-road concentrations.

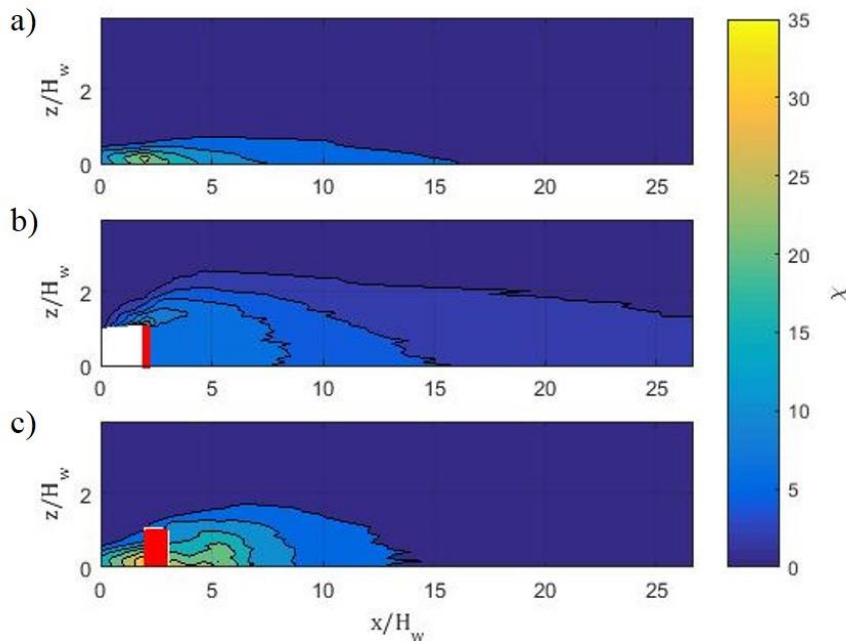


Figure 3-7- Concentration contours for a) flat terrain, b) solid barrier, and c) vegetation cases. Barriers are represented by red rectangles.

Figure 3-8 shows vertical profiles of concentrations at six downwind distances for all cases. As expected, the solid barrier reduces concentrations below the barrier height. The

concentration is well-mixed from the surface to the barrier height behind the solid barrier and it peaks at some height above the barrier, as was incorporated into the modified mixed-wake model developed by Amini et al. (2016).

On the other hand, vegetation seems to increase concentrations from the surface to the barrier height for several barrier heights downwind of the road. The difference among concentrations of three cases vanishes as the plume travels downwind and the effects of solid and vegetation barriers diminish.

The question that still remains is that why surface concentrations behind vegetation are larger than those of flat terrain case within several barrier heights downwind of vegetation barrier.

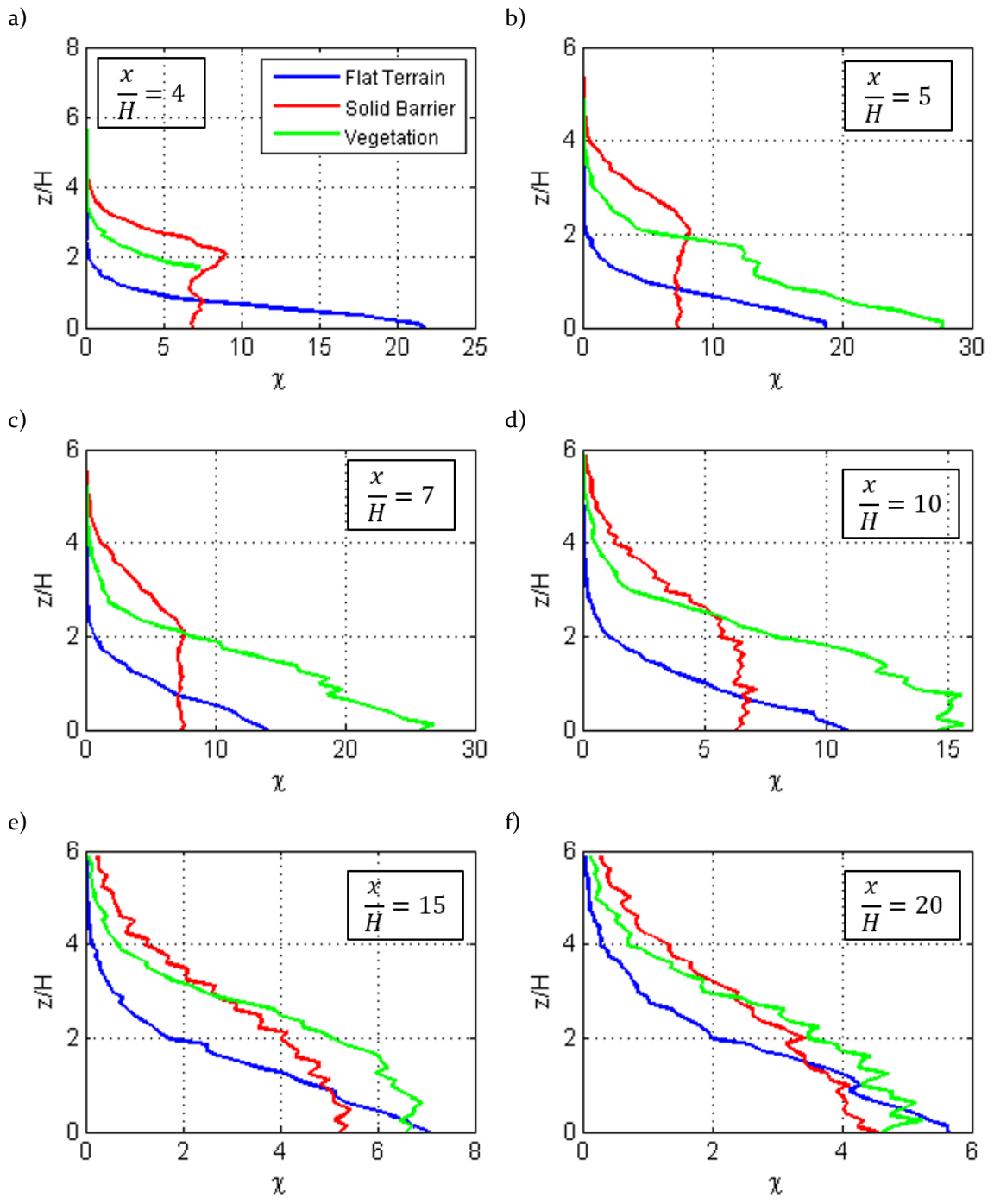


Figure 3-8- Vertical profiles of concentrations for all 3 case at six different downwind distances.

### 3.3 Data analysis

The surface concentration data behind the vegetative barrier were analyzed by modifying the analytical line source model in two different ways; first, we assume that the only effect of the vegetative barrier is to increase initial plume spread (first scenario), which simulates the effect of a solid barrier in reducing concentrations relative to those in flat terrain. Second, we assume that while increasing the initial plume spread, vegetation decreases turbulence levels behind the barrier as well (second scenario).

Vertical profiles of the ratio of  $\sigma_u$  behind the vegetative barrier to  $\sigma_u$  in the undisturbed boundary layer are shown in Figure 3-9. This figure shows that turbulence levels below the vegetation height are reduced downwind of the barrier and then recover with distance as the turbulent kinetic energy is entrained from above. The reduction of  $\sigma_u$  at receptors below vegetation height and within  $3H_w$  from vegetation has a mean value of 50% and a standard deviation value of 23%. Using the  $\sigma_u$  reduction level, we assume that the surface friction velocity at the area close to the vegetation reduces by 55%, resulting in  $u_{*2} = 0.11 \text{ m/s}$ . This reduction in turbulence is likely to be larger with increasing vegetation height and/or decreasing porosity.

Initial vertical dispersion of the flat terrain case is found to be  $h_0 = 0.8 \text{ m}$  by comparing the modeled surface concentration gradients against the observed ones (Figure 3-10). Initial vertical dispersion of the vegetation case is assumed to increase to  $h_0 = 3 \text{ m}$ .

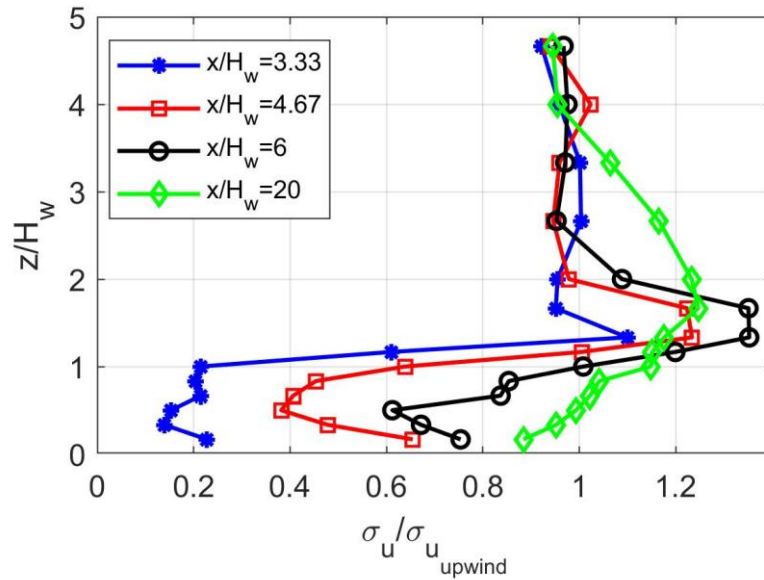


Figure 3-9- Vertical profiles of the ratio of  $\sigma_u$  behind vegetation barrier to  $\sigma_u$  in undisturbed boundary layer. The vegetation extends from  $x = 2H_w$  to  $x = 3H_w$ .

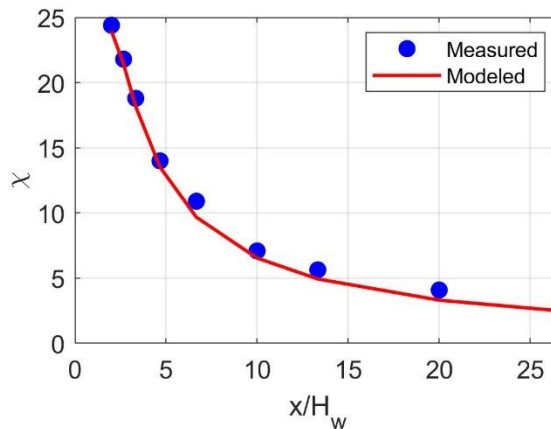


Figure 3-10- Comparison of measured surface concentrations with estimated surface concentrations versus downwind distance in the flat terrain case.

We incorporate the resulting values of the surface friction velocity and initial vertical dispersion for vegetation into the line source model to estimate surface concentrations downwind of the vegetation. Figure 3-11 compares the estimated surface concentrations behind vegetation using the two scenarios against the measured surface concentrations. The measured surface concentrations in vegetation case lie within the limits of the two scenarios. The data close to the vegetation are explained well by the decrease in turbulence

levels and increase in initial vertical dispersion, and the data far from the vegetation barrier are explained well only by the increase in initial vertical dispersion. The shift between these two scenarios occurs within  $[3H_w, 7H_w]$  from the leeward edge of vegetation, which is consistent with the observations in Figure 3-9. Thus, the effect of vegetation on reducing turbulence does not go beyond  $7H_w$ . Observed flat terrain surface concentrations are also shown for reference. The surface concentrations measured in the flat terrain case converge to those of the vegetation barrier case around  $17H_w$  from the downwind edge of the vegetation; surface concentrations downwind of the vegetation barrier at  $17H_w$  from the edge of the vegetation is 15% less than that of the flat terrain.

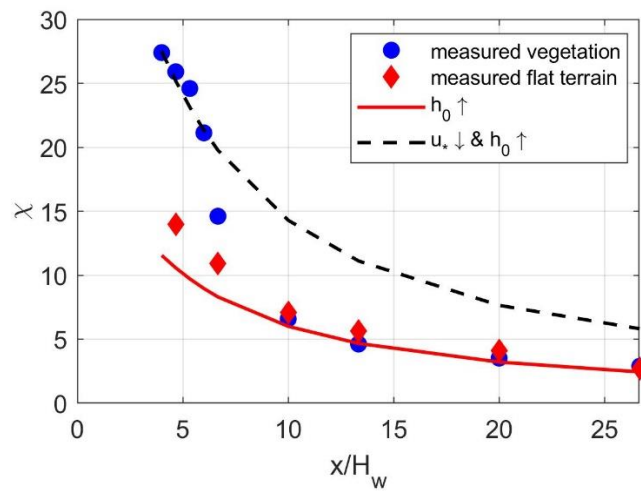


Figure 3-11- Comparison of the measured surface concentrations with estimated surface concentrations versus downwind distance. Vegetation ends at  $3H_w$ .

### 3.4 Conclusions and summary

We analyzed the results from a wind-tunnel study to examine the impacts of vegetative and solid barriers on near-road air quality. The solid barrier decreased ground-level concentrations downwind of the barrier compared to flat terrain by up to 0.3. However, the study showed that presence of vegetation can result in up to 50% increase in surface

concentrations for several barrier heights downwind of vegetation compared to corresponding receptors in flat terrain.

The concentration data behind vegetation were analyzed by using a semi-empirical dispersion model that incorporates the effects of vegetation on the turbulence and velocity fields. The measured ground-level concentrations lie between two limits; the first limit assumes that vegetation only increases the vertical plume spread, and the second limit assumes that vegetation, in addition to increasing vertical plume spread, decreases surface friction velocity. Measured concentrations within  $[0, 3H_w]$  from the leeward edge of vegetation are close to the second limit, while measured concentrations beyond  $7H_w$  from the leeward edge of vegetation are close to the first limit. It should be noted that the effect of the initial vertical plume spread on total vertical plume spread ( $\sigma_z$ ) diminishes as the downwind distance increases; thus, the surface concentrations downwind of vegetation barrier eventually converges to those of the flat terrain.

This analysis indicates that vegetative barriers influence dispersion of air pollutants close to the roadways in two counteracting ways: 1) they decrease turbulence behind the barrier, 2) they increase vertical mixing. These two opposing effects can lead to a decrease or increase in concentrations relative to those in the absence of the barrier. This is the main reason of the inconclusiveness of past research on the effects of vegetation on roadway-emitted pollutants, including Hagler et al. (2012) and Brantley et al. (2014). Further research is needed to determine the dominant effect under different conditions. This depends on multiple parameters such as geometry, porosity, and pressure loss coefficient of vegetation, stability of the atmosphere, and turbulence properties of the incoming flow.

# 4 Modeling Dispersion of Emissions from Depressed Roadways

## 4.1 Introduction

A small number of studies have examined dispersion of emissions from depressed roadways. The most notable of these is a field study conducted in Los Angeles air basin by California Department of Transportation (CalTrans) to collect data to understand dispersion of primary pollutants emitted from freeways with various configurations, including at-grade, depressed, and elevated highways (Bemis et al., 1977). Air pollutants sampled included CO, reactive and unreactive hydrocarbons, NO<sub>x</sub>, O<sub>3</sub>, SO<sub>2</sub>, and H<sub>2</sub>S. Particulate sampling was also conducted to obtain total particulates and lead. The results of this study were incorporated into the development of a dispersion model called CALINE2 (Bemis et al., 1977).

Feeney et al. (1975) measured aerosols and particulate lead concentrations in the vicinity of several road configurations, including a depressed roadway. Samplers were placed 20 m upwind of a freeway and at several distances downwind of the freeway ranging from 27 m to approximately 160 m from the median strip. They found that the mass

concentrations of traffic-derived lead were generally lower downwind of the depressed roadway relative to that predicted by a dispersion model that assumed the emissions occurred at road level.

Heist et al. (2009) conducted a comprehensive wind-tunnel study on dispersion of emissions from model depressed roadways. The studied configurations included a flat roadway, a 6 m and a 9 m deep depressed roadway with vertical sidewalls, a 6 m deep depressed roadway with 30° sloping sidewalls, and a 6 m deep depressed roadway with 30° sloping sidewalls with two 6 m solid barriers on top of the road. They observed that these configurations alter the flow field, increase downwind dispersion, and reduce downwind surface concentrations relative to the flat terrain case. The level of reduction in concentrations depended on the particular configuration.

Wind tunnel studies can provide more information on the processes that govern dispersion in complex situations than field studies can because the governing inputs are controlled and details of the flow fields can be measured. Although they do have the disadvantage of being unable to simulate the effects of atmospheric stability, they provide information that is vital to the development of models for situations in which the effects of source geometry on the flow field are dominant. For example, the wind tunnel results (Heist et al., 2009) on dispersion of pollutants downwind of the roadways in the presence of noise barriers have been incorporated into several dispersion and CFD models (Ahangar et al., 2017b; Amini et al., 2016; Ghasemian et al., 2017; Hagler et al., 2011; Schulte et al., 2014; Steffens et al., 2014).

Baldauf et al. (2013) conducted a field study in Las Vegas, Nevada, to investigate the effects of a depressed roadway on local-scale air quality downwind of the depression. They

measured CO and NO<sub>x</sub> concentrations along a complex urban highway at two sections; a section at-grade with the surroundings and another section that was depressed. The vertical height from the roadbed to the top of the surroundings was 5 m, and the slope of the sidewalls was approximately 20°. The stationary monitors located 20 m from the downwind edge of the freeway at both sections showed that the maximum concentration events occurred at the at-grade site. However, during some mid- and low-concentration events, the monitor downwind of the cut section observed higher concentration levels than that of the at-grade section. The mobile monitoring data collected along the at-grade and cut section transects indicated that the concentrations at the at-grade transect were greater than those at the cut section transect at 35 m from the downwind edge of the freeway, with concentrations then becoming similar along both gradients further downwind of the highway. They also conducted a wind tunnel simulation of the study site to examine the flow field and the concentration distributions in the vicinity of the highway. The wind tunnel simulations revealed that the cut section reduced concentrations of pollutants measured at breathing-level height by 15 – 25% relative to the flat terrain case for receptors located approximately 20 m from the downwind edge of the highway. Although the field data were not conclusive, the data collected under the controlled conditions of the wind tunnel indicated that depressed roadways led to reductions in downwind near-surface concentrations relative to those next to at-grade roadways.

The observed CO concentrations around depressed roads in the CalTrans field study (Bemis et al., 1977) were used to develop the depressed road model in the California Line Source Dispersion Model (CALINE2). CALINE is based on the Gaussian plume model and is used to estimate air pollutant concentrations near roadways. Compared to equivalent at-

grade sites, greater values for initial vertical dispersion are used for depressed roads to explain the observed concentrations in the CalTrans field study (Bemis et al., 1977; Benson, 1992b). As discussed in chapter 1, there is a need to develop a dispersion line source model that estimates concentrations downwind of different road configurations, including depressed roadways, to add to the capabilities of the RLINE (Snyder et al., 2013). In this chapter, we modify a flat terrain line source dispersion model to account for dispersion from depressed roads.

In this chapter, we analyze the concentrations and turbulence levels measured in the wind tunnel study downwind of the at-grade and depressed roads (Heist et al., 2009) to gain insight into the processes that govern dispersion of pollutants from a depressed highway. Based on this insight, we propose a method to incorporate the dominant effects of the depressed roadway into a flat terrain model. These effects are first parameterized in a model proposed by van Ulden (1978) which not only provides a good description of ground-level concentrations but also the vertical profiles measured during the Prairie Grass experiment (Barad, 1958). We then suggest how our findings can be incorporated into RLINE model, a Gaussian dispersion model, that focuses on ground-level concentrations. The results and the approach of this chapter are partly addressed in conference papers of Venkatram and Amini (2017), Schulte et al. (2017), and Amini et al. (2017).

## **4.2 Wind tunnel experiments**

### **4.2.1 Experiment description**

Heist et al. (2009) performed an experimental study in the U.S. EPA's Meteorological Wind Tunnel (Snyder, 1979) to explore the effects of different road configurations on the

dispersion of traffic-related pollutants downwind of roads. The wind tunnel test section is 3.7 m wide, 2.1 m high, and 18.3 m long. A simulated atmospheric boundary layer was generated using three truncated triangular (Irwin, 1981) spires mounted near the entrance to the test section. To maintain the boundary layer, the floor of the test section downwind of the spires was covered with roughness blocks. The position of spires and roughness blocks are shown in Figure 4-1. There are no roughness blocks in the proximity of the line sources where turbulence and concentration measurements are conducted. The modelled freeway is a six lane divided highway at 1:150 scale. The width of the modelled freeway is 36 m full scale. The origin of the coordinate system is at the center of the roadway on the wind tunnel floor, with the positive  $x$  in the stream wise direction,  $y$  along the axis of the roadway, and  $z$  vertically upward. The wind-tunnel study examined twelve roadway configurations. In this paper, we focus on three depressed roadway configurations and compare the results to those of a flat roadway.

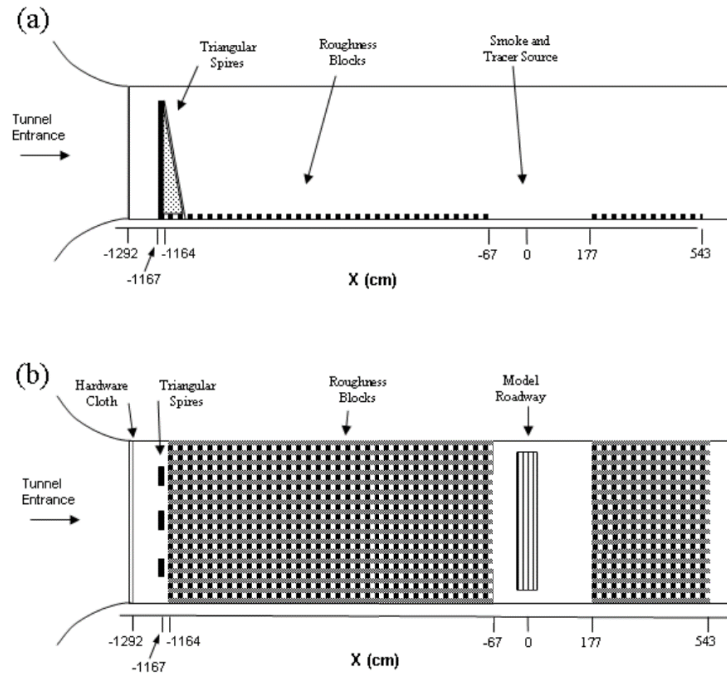


Figure 4-1- Schematic of near roadway wind tunnel setup: a) elevation and b) plan view.

Laser Doppler Velocimetry (LDV) was used for all velocity measurements in this study, details of which are described in Heist et al. (2009). The roughness length ( $z_0$ ), the friction velocity ( $u_*$ ), and the displacement height ( $dh$ ) were assessed by fitting the standard logarithmic velocity profile to the near surface measured upwind velocity profile in the FLAT case at  $x = -16.75H$ :

$$U(z) = \frac{u_*}{\kappa} \ln\left(\frac{z - dh}{z_0}\right) \quad (4-1)$$

where  $\kappa$  is the von Karman constant, taken to be 0.4. The values of  $u_*$ ,  $z_0$ , and  $dh$  were calculated to be 0.17 m/s, 0.10 m and 0 m, respectively.

The configurations that were studied in this paper are shown in Figure 4-2. We examine a 6 m deep depressed roadway with vertical sidewalls (D690), a 6 m deep depressed roadway with 30° angled sidewalls (D630), and a 9 m deep depressed roadway with vertical sidewalls (D990). Observations of flow and dispersion for these configurations were compared with

those from the flat roadway case (FLAT). The width of the road in all cases is 36 m (full scale) and the width of the opening in D630 case is around 57 m (full scale). The letter 'D' in a case name stands for 'Depressed', the first single digit number represents the depth of the road in meters, and the two-digit number at the end of a case name denotes the angle between the sidewalls and the roadbed, in degrees.

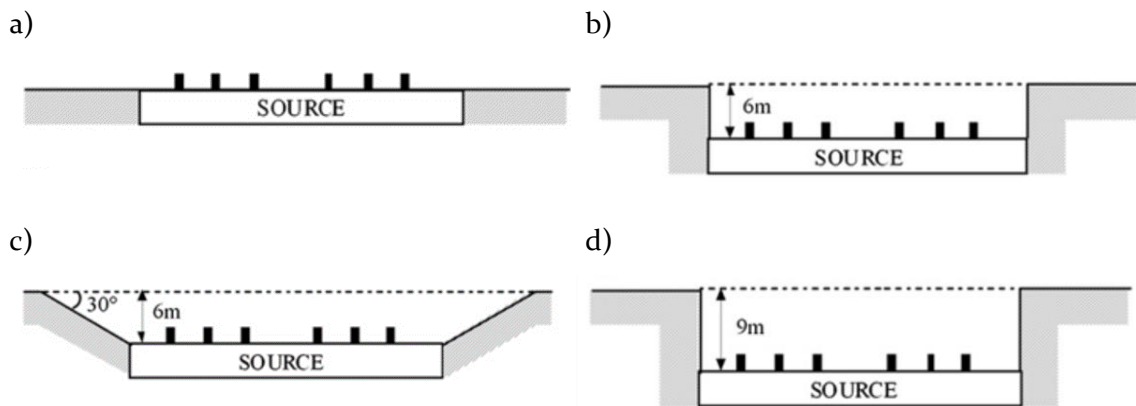


Figure 4-2- Elevation view showing cross sections through the different roadway designs studied; a) flat terrain roadway (FLAT), b) 6 m deep depressed roadway with vertical sidewalls (D690), c) 6 m deep depressed roadway with 30° sloping sidewalls (D630), and d) 9 m deep depressed roadway with vertical sidewalls (D990). The small black rectangles indicate the location of the tracer emission lines. The width of the road in all cases is 36 m. Adapted from Heist et al. (2009).

The tracer gas used in the study was high-purity ethane ( $C_2H_6$ ) which is only slightly heavier than air. The flow rate of the tracer gas is 1500 cc/min. All samples were drawn through Rosemount Model 400A hydrocarbon analyzers. The concentrations of ethane were normalized to give the non-dimensional concentration  $\chi = CU_r/(Q/L_xL_y)$ , where  $C$  is the concentration (a fraction by volume) with background concentration subtracted,  $U_r$  is the reference wind speed (equal to 2.46 m/s, measured at a full-scale equivalent height of 30 m),  $Q$  is the volumetric effluent rate (1500 cm<sup>3</sup>/min of ethane),  $L_x$  is the alongwind dimension of the roadway segment (24 cm, 36 m full scale), and  $L_y$  is the lateral length of the source segment (48 cm, 72 m full scale). In this study, we focus on concentrations

associated with infinitely long line sources. As explained by Heist et al. (2009), the infinite line source results are constructed by superposition of concentrations resulted from five finite line segments placed laterally next to each other. Finally, the length scale,  $H$ , used throughout the study is 6 m (full scale).

#### **4.2.2 Experimental results**

##### **4.2.2.1 Impact of road depression on the velocity field**

The impact of road configurations on the flow field is shown in Figure 4-3. We see that the depressions modify the flow field relative to that of the FLAT case. Roadways with vertical sidewalls (D690 and D990) create recirculating flow in the depressed regions, with a stronger recirculation in the deeper road cut case (D990). The D630 case, with angled sidewalls, has the least effect on the flow field, showing little evidence of recirculation in the depressed region.

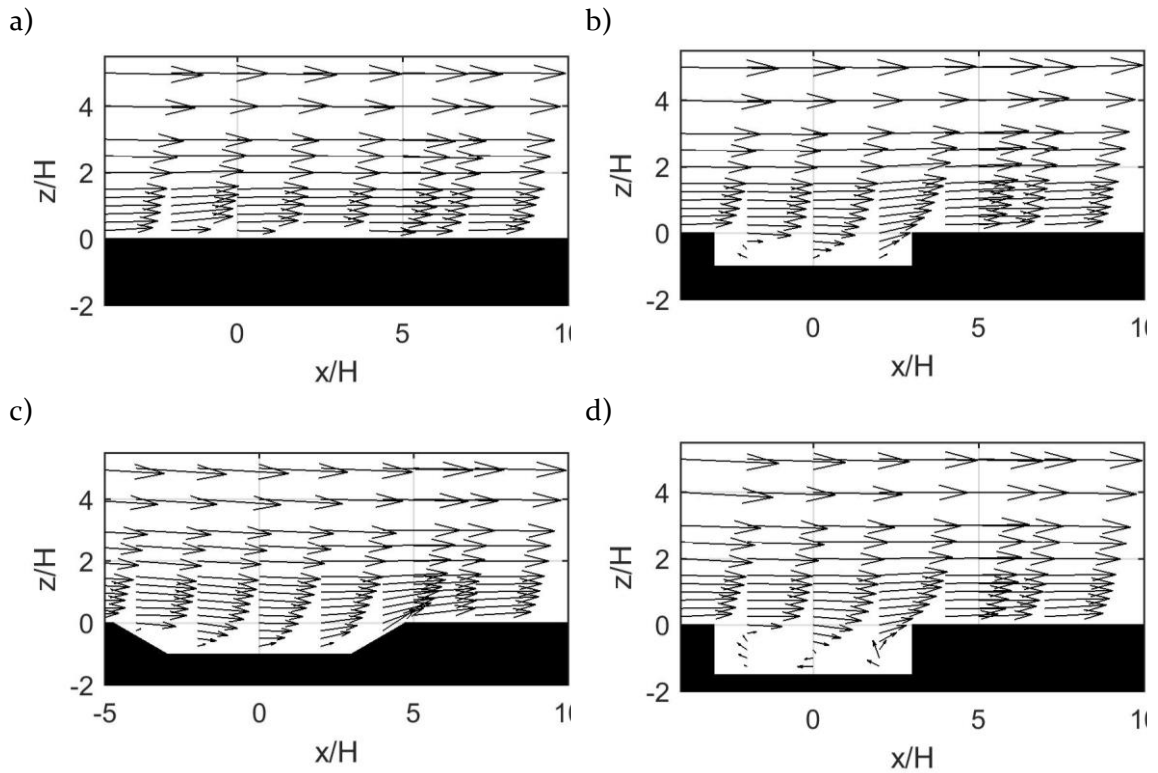


Figure 4-3- Observed mean velocity vectors for a) FLAT, b) D690, c) D630, and d) D990 cases.

The vertical profiles of horizontal velocity in the FLAT case, shown in Figure 4-4, indicate that the horizontal wind speed increases with downwind distance from the road. This acceleration is caused by the absence of roughness blocks in the region  $-16.75H$  to  $44.25H$ , which includes the measurement zone. Due to conservation of ethane mass, the acceleration of the air flow causes a reduction in concentration over downwind distance that adds to that caused by vertical dispersion. The reduction in concentration due to the acceleration occurs in all cases; thus we can assume that the concentration reduction in depressed cases compared to the flat case is approximately only due to the effects of the depression.

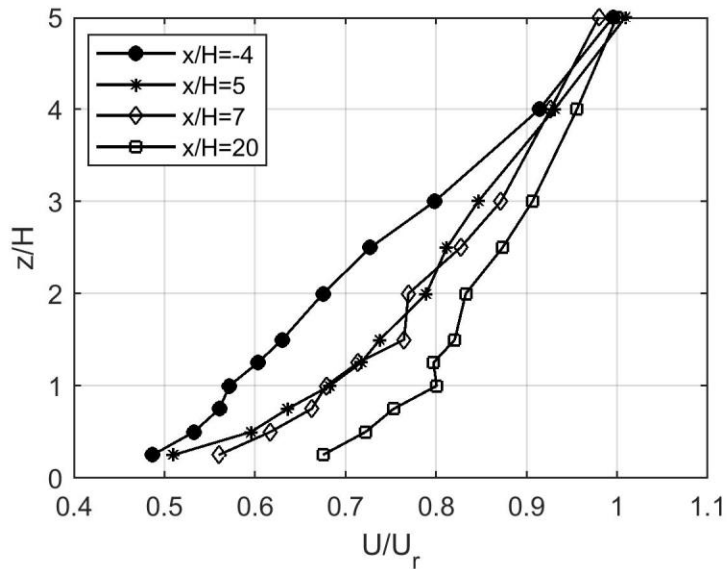


Figure 4-4- Vertical profiles of horizontal velocity at multiple downwind locations in FLAT case. The air speed increases as air travels downwind.

#### 4.2.2.2 Impact of road depression on the turbulence field

Since the turbulence field plays a significant role in dispersion of traffic-related emissions (Tong et al., 2015), it is useful to examine the impact of different road configurations on Turbulent Kinetic Energy (TKE) values relative to those for the FLAT case. Figure 4-5 shows the downwind variation of the square root of the ratio of TKE of depressed cases to that of flat terrain at  $z = H/2$ . This figure clearly indicates that the depression in the road is a source of shear generated turbulence, which causes the TKE to remain larger than that of flat terrain for the entire domain. As expected, the TKE of D990 is almost always larger than that of D690. The TKE in the D630 case exceeds that of D990 beyond  $x = 20H$ .

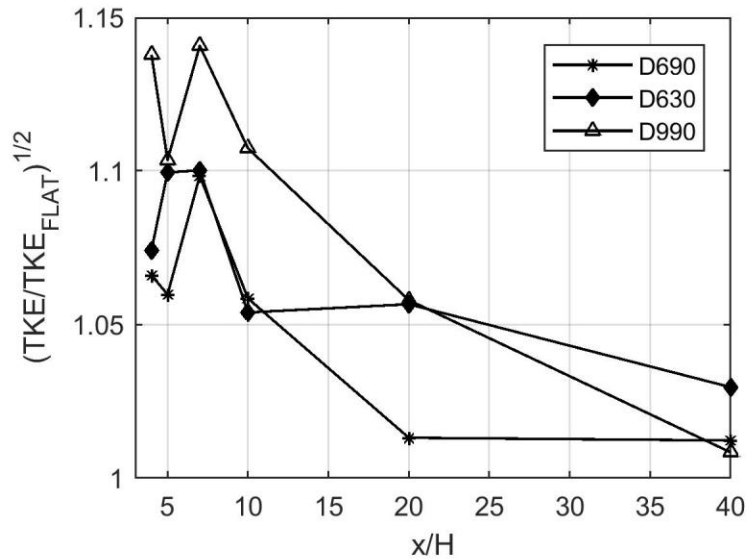


Figure 4-5- Gradient of square root of TKE values of a) D690, b) D630, and c) D990 cases, normalized by the corresponding values observed at flat terrain case.

#### 4.2.2.3 Impact of road depression on the concentration field

Concentrations considered in this study are concentrations observed downwind of the simulated freeways and at the same level with surroundings. For FLAT, D690, and D990 cases, it corresponds to concentrations measured at  $x \geq 3H$ , and for D630 case, it corresponds to those at  $x \geq 4.75H$ . Figure 4-6 shows the variation of surface concentrations with downwind distance for the different cases. The left panel shows the differences between the surface concentrations of the FLAT case and the depressed cases as a function of downwind distance. The right panel focuses on the differences in surface concentrations among the depressed roadway cases close to the road. All configurations decrease surface concentrations relative to those in the flat terrain case. The relative concentration reduction is highest for D990 case with the value of 80% very close to the road,  $x = 3H$ . As expected, the surface concentrations in D990 are lower than those in D690. The surface concentrations downwind of the road in D630 are higher than those of D990 everywhere except at  $x = 15H$ , where the surface concentration of D630 case is 95% of that of D990. As

expected, the effects of road configurations on dispersion of roadway-emitted pollutants decreases with downwind distance from the edge of the depression. For example, the surface concentration reduction of D990 relative to the flat terrain at  $x = 3H$  is 80%, while that at  $x = 40H$  is only 24%. But the scale over which the concentration approaches the flat terrain case varies with road configuration. For example, the surface concentration ratio of D990 case to D690 case at  $x = 3H$  is 0.83, where the effect of configuration is large, while that at  $x = 40H$  is 0.95.

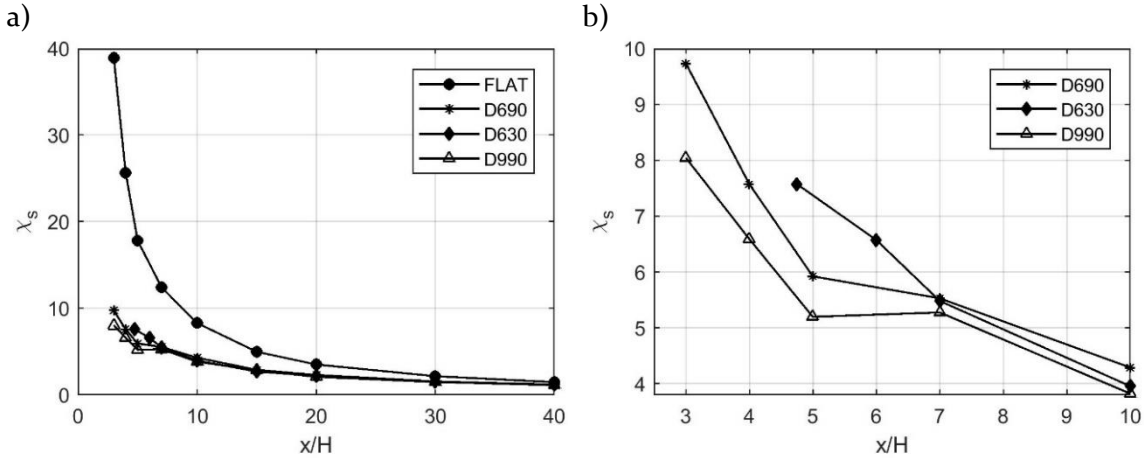


Figure 4-6- Surface concentration as a function of downwind distance for different road configurations. Left plot includes flat terrain concentrations.

## 4.3 Framework for the depressed road models

### 4.3.1 Modified van Ulden model

#### 4.3.1.1 Model development

The wind tunnel results show that the depressed roadways 1) induce complex patterns, which includes recirculation within depressed roadways with vertical walls and 2) increase turbulence levels downwind of the depression relative to the FLAT case. In our modeling approach, we do include these effects explicitly, but examine parameterizing them within the framework of a dispersion model applicable to flat terrain. As we will show later, only

two parameters are needed to describe the distance evolution of both ground-level as well as vertical profiles of concentrations. Our primary result is that a flat terrain model can be modified in a simple manner to capture the dominant effects of a depression on the dispersion of pollutants emitted from it. We show that there is a qualitative relationship between the geometry of the depression and the values of the parameters. The data from the wind tunnel studies have not yet yielded a quantitative relationship although we can interpolate between the values presented in this paper.

Our first analysis of the experimental results is based on a model proposed by van Ulden (1978) which has been evaluated with observations from the Prairie Grass experiment (Barad, 1958). This model, which is the analytical solution of the eddy diffusivity-based mass conservation equation, expresses the concentration associated with a point source with strength  $Q$  (unit:  $g \cdot s^{-1}$ ). We use this model to estimate the concentration associated with an infinitely long line source with strength  $q$  (unit:  $g \cdot s^{-1} m^{-1}$ ), as

$$C(x, z) = \frac{Aq}{\bar{U}\bar{z}} \exp\left(-\left(\frac{Bz}{\bar{z}}\right)^s\right) \quad (4-2)$$

where the value of  $s$  depends on stability (Nieuwstadt and van Ulden, 1978).  $A$  and  $B$  values are constant and depend only on  $s$  (van Ulden, 1978),  $\bar{z}$  is the mass-weighted plume height defined as

$$\bar{z}(x) = \frac{\int_0^\infty zC(x, z)dz}{\int_0^\infty C(x, z)dz} \quad (4-3)$$

and  $\bar{U}$  is the mass-weighted plume velocity defined by

$$\bar{U}(x) = \frac{\int_0^\infty U(z)C(x, z)dz}{\int_0^\infty C(x, z)dz} \quad (4-4)$$

We found that the shape of the observed vertical concentration profiles of all cases at various downwind distances are best reproduced by  $s = 1.3$ . This value of  $s$  agrees well with the values reported for neutral conditions by Nieuwstadt and van Ulden (1978). The comparison of the observed vertical concentration profiles of the FLAT case with estimates of the formulation with  $s = 1.3$  and  $s = 2$  are shown in Figure 4-7 and Figure 4-8, respectively. Throughout this section, we assume that  $s = 1.3$  which results in  $A = 0.8$  and  $B = 0.74$ . The plume spread is related to the mean plume height by

$$\sigma_z = f_z \bar{z} \quad (4-5)$$

where  $f_z$  is also a function of the shape factor with the value of  $f_z = 1.34$  for  $s = 1.3$  (Venkatram, 2004). The growth of  $\bar{z}$  with  $x$  is given by the equation derived by van Ulden (1978)

$$\frac{d\bar{z}}{dx} = \frac{K(q\bar{z})}{U(q\bar{z})q\bar{z}} \quad (4-6)$$

where  $K(z)$  is the eddy diffusivity for heat and  $q = 1.54$  when  $s = 1.3$  (Venkatram, 2004).

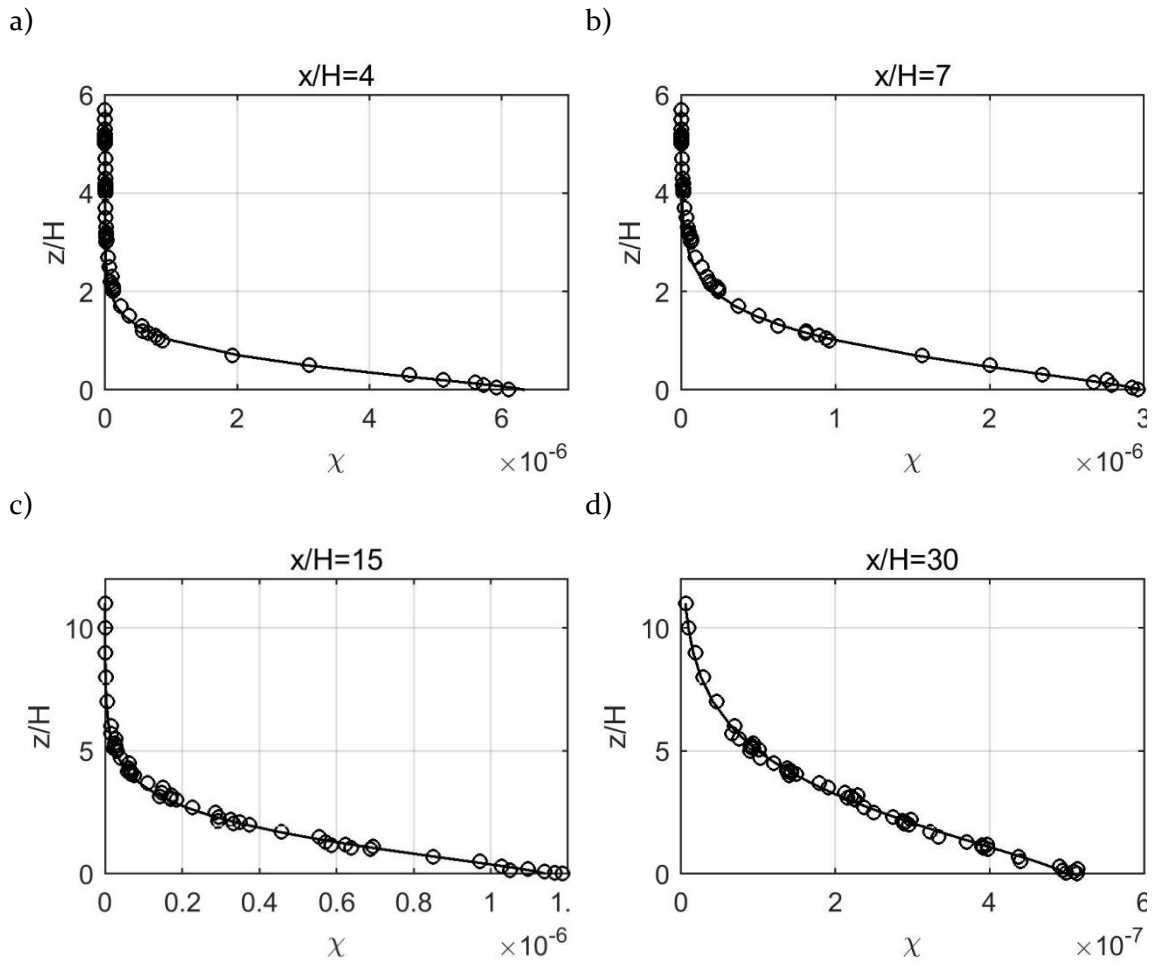


Figure 4-7- Performance of a vertical distribution function with exponent  $s=1.3$  in estimating vertical concentration profiles of the FLAT case at different downwind distances.

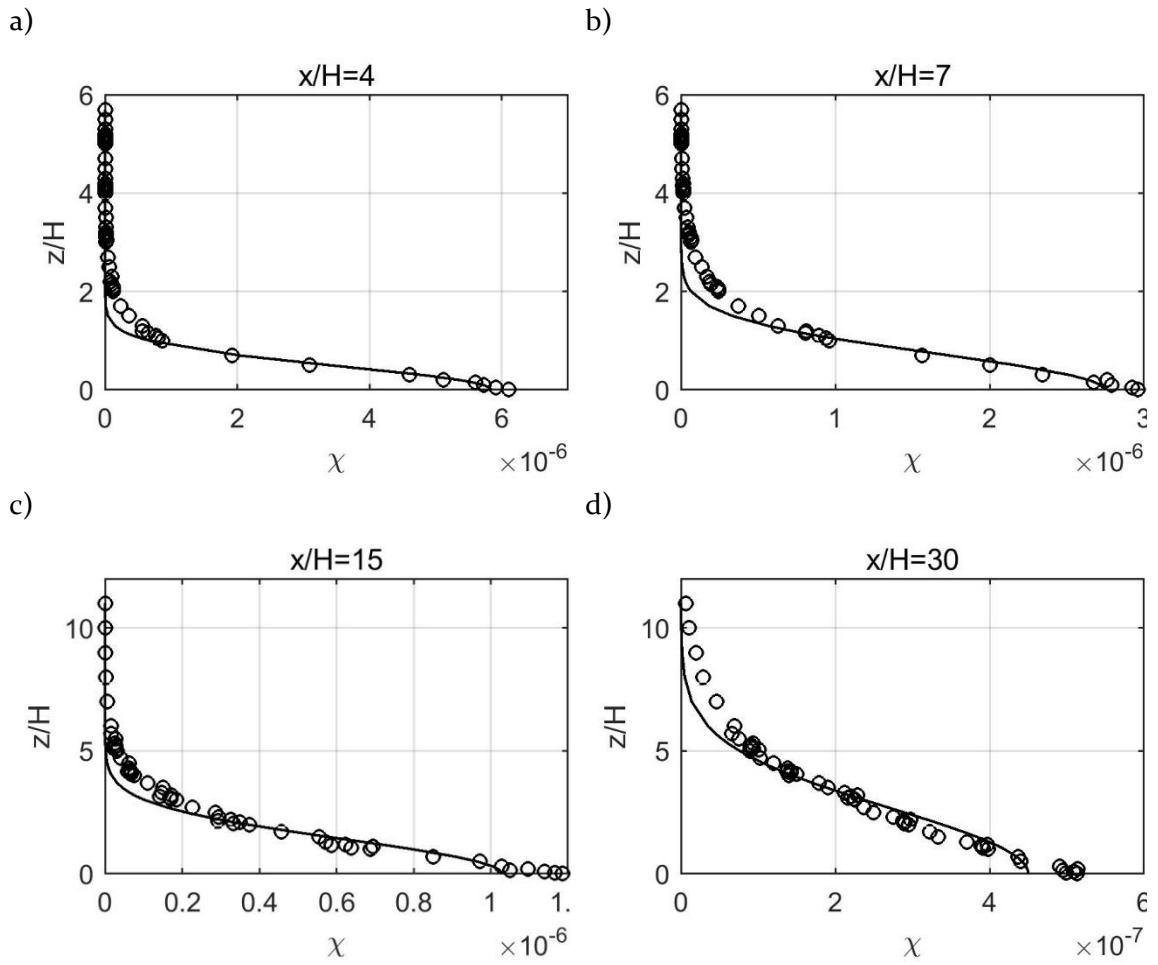


Figure 4-8- Performance of a vertical distribution function with exponent  $s=2$  in estimating vertical concentration profiles of the FLAT case at different downwind distances.

Following van Ulden (1978), we assume that the wind speed,  $U(z)$ , can be written by a power law

$$U(z) = U_r \left( \frac{z}{z_r} \right)^p \quad (4-7)$$

where  $U_r = 2.46 \text{ m/s}$  is the reference velocity at the reference height  $z_r = 30 \text{ m}$  (full scale) above the wind tunnel floor. We obtain the value of  $p$  by fitting equation 4-7 to the vertical profiles of wind speed in the wind tunnel. As discussed in section 4.2.2.1, the absence of roughness blocks results in change in the shape of the vertical profiles of horizontal velocity, which in turn results in  $p$  varying over distance. It turns out that the upwind velocity follows

a power law with  $p = 1/4$  and velocity profiles at different downwind distances follow power law functions with  $p$  ranging from  $1/7$  to  $1/4$ ;  $p$  decreases with increasing downwind distance. We use  $p = 1/7$  for the rest of our analysis. It is shown that the final conclusions of our analysis remain the same if  $p = 1/4$  (Table 4-1). However, we should note that the model uses a constant  $p$  value while velocity measurements show that  $p$  varies over distance.

Table 4-1- Values of empirical parameters of different cases that form the  $\sigma_z$  expression ( $s=1.3$  and  $p = 1/4$ ).

Case	$h_0(m)$	$\beta/\beta_{flat}$
FLAT	1.00	1.00
D690	4.20	1.17
D630	3.90	1.38
D990	5.60	1.25

By substituting equation 4-64-7 into 4-6 and assuming that the eddy diffusivity corresponds to the neutral expression  $K(z) = \kappa u_* z$ , where von Karman constant is  $\kappa = 0.4$ , we can integrate equation 4-6, assuming that the initial vertical plume spread is  $h_0$ ,

$$\bar{z} = \left[ \beta \frac{(p+1)}{q^p} \kappa \frac{u_*}{U_r} z_r^p x + \left( \frac{h_0}{f_z} \right)^{p+1} \right]^{\frac{1}{p+1}} \quad (4-8)$$

Although it is not used explicitly in our analysis, we present the associated equation for the more familiar measure of vertical spread,  $\sigma_z$ , as a function of  $x$  and  $h_0$ ,

$$\sigma_z = \left[ \beta \frac{(p+1)f_z^{p+1}}{q^p} \kappa \frac{u_*}{U_r} z_r^p x + h_0^{p+1} \right]^{\frac{1}{p+1}} \quad (4-9)$$

Note that  $p = 1/7$  results in  $\sigma_z \sim x^{7/8}$  when  $h_0$  is small.

We account for the effects of the depressed road through two parameters: a factor  $\beta$  which multiplies the flat terrain friction velocity in equation 4-9 and an initial vertical

plume spread  $h_0$ . The values of these parameters are obtained by fitting results from the modified van Ulden model to the near-surface concentration measurements made in the wind tunnel. It is important to note that that only two parameters are used to fit entire range of concentrations associated with each of the road configurations.

#### **4.3.1.2 Estimation of the empirical parameters**

Concentrations downwind of the freeway were modeled as the sum of concentrations due to six individual line sources, the same number of line sources in the wind tunnel (Heist et al., 2009). For each case, we fit the near-surface concentrations estimated by the modified van Ulden model to those observed in the wind tunnel to obtain the values of the two parameters,  $\beta$  and  $h_0$ . The values of these parameters are listed in Table 4-2. These values suggest that it is necessary to use an initial vertical dispersion of 1.2 m to describe the concentrations for the flat terrain case. A 6 m depressed roadway with straight edges adds 3.7 m to the initial vertical dispersion of flat terrain, while a 9 m depressed roadway with straight edges adds 4.8 m. The D630 case adds 2.4 m to the flat terrain initial vertical dispersion, indicating the smaller role of turbulent mixing in the presence of sloping walls. This suggests that one effect of the road depression is to increase the initial vertical dispersion. This is consistent with the method used in CALINE2 to account for the roadway depression (Benson, 1992b).

The second effect of the road depression is an increase of  $\beta$ , which is interpreted as an increase in the rate of vertical plume spread or turbulence levels. The D690, D630, and D990 cases result in increases of 12%, 37%, and 31% in this rate compared to those of flat terrain, respectively. This is consistent with the results shown in Figure 4-5, where larger values of TKE were observed in depressed cases compared to the FLAT case. The highest rate for the

D630 case could be attributed to the vertical velocities induced by the upward slope of the downwind edge of the depression. Figure 4-3 appears to support this hypothesis. It should be noted that the model does not take into account the impacts of vertical components of the wind velocity on downwind concentrations. Therefore, these effects may represent themselves into other factors of the model, such as increase in turbulence levels.

Table 4-2- Values of empirical parameters of different cases that form the  $\sigma_z$  expression ( $s=1.3$  and  $p = 1/7$ ).

Case	$h_0(m)$	$\beta$
FLAT	1.2	1.00
D690	4.8	1.12
D630	3.6	1.37
D990	5.9	1.31

#### 4.3.2 Modified RLINE model

##### 4.3.2.1 Model development

As discussed earlier, one of the objectives of this research is to enable RLINE model to estimate concentrations downwind of the depressed roadways. In this section we suggest modifications to RLINE model to account for the effects of depressed roads on dispersion. RLINE (Snyder et al., 2013) is designed for estimating surface concentrations close to roadways. It is based upon a steady-state Gaussian formulation and treats a line source as a set of point sources and integrates over the differential concentrations at the receptor due to each point source (Snyder et al., 2013). This model is different from the van Ulden model in two ways: 1) it assumes that the vertical distribution of concentration is a normal (Gaussian) distribution, and 2) the velocity profile follows a logarithmic profile (equation 4-1).

As shown in Figure 4-8, the model, based on the Gaussian vertical distribution with the  $z$  exponent, is not able to estimate concentrations measured in the wind tunnel at all heights. We estimate near-surface concentrations by modifying RLINE using the two parameters described in a similar manner to the previous section.

RLINE, as we have modified it, computes the vertical spread of the plume using the following formula for neutral conditions:

$$\sigma_z = \sqrt{h_0^2 + \sigma_{zF}^2}; \sigma_{zF} = 0.57\alpha \frac{u_*}{U(\bar{z})} x \quad (4-10)$$

where  $\sigma_{zF}$  is computed using the formulations derived by (Venkatram et al., 2013b) for neutral conditions. We account for the effects of the depressed road through two parameters: a factor  $\alpha$  for increasing turbulence, and initial vertical dispersion,  $h_0$ , in the presence of the road depression. We will adjust  $\alpha$  and the initial vertical dispersion value for each case to find the best fit to near-surface observed concentrations. This will be done in the next section.

#### 4.3.2.2 Estimation of the empirical parameters

Following the procedure in section 4.3.1.2, the magnitudes of  $h_0$  and  $\alpha$  for each case are calculated in such a way that the near-surface concentrations estimated by the modified RLINE model reproduce the observed values (Table 4-3). Increase in initial vertical dispersion and friction velocity of depressed cases in the modified RLINE follow the same trend as those in the modified van Ulden model, although the magnitudes are different in the two models. The differences in magnitudes are related to describing the velocity profile using the logarithmic function and the concentration profile using the Gaussian distribution in the RLINE model. While the initial vertical dispersion is calculated to be

0.4 m for the FLAT case, the value of this parameters increases to 4.0 m, 3.5 m, and 4.8 m for the D690, D630, and D990 cases. As in the modified van Ulden model, the largest increase in turbulence levels is observed in the D630 case ( $\alpha = 1.87$ ), while the slightest increase occurs in the D690 case ( $\alpha = 1.67$ ).

Table 4-3- Values of empirical parameters of different cases that form the  $\sigma_z$  expression in RLINE model.

Case	$h_0$	$\alpha$
FLAT	0.4	1.00
D690	4.0	1.67
D630	3.5	1.87
D990	4.8	1.83

#### 4.4 Comparison of the modified models with observations

After obtaining the empirical values of the modified models' parameters for each case, that were determined to reproduce near-surface concentrations, we evaluate the models' capability to explain the concentration data at all heights. It is worth noting that for each case, the empirical values of these parameters do not vary over downwind distance.

To compare the modeled concentrations at all heights to the corresponding observed values, we used the following statistical parameters: the logarithmic mean of the ratios of the observed concentration to the estimated concentration,  $m_g$ , the logarithmic standard deviation of the ratios,  $s_g$ , the fraction of estimated concentrations that lie between 0.5 and 2 times the observed concentrations (fac2), the correlation coefficient ( $r^2$ ) (Venkatram, 2008), and normalized mean square error (NMSE) (Chang and Hanna, 2004).

#### 4.4.1 Modified van Ulden model

The performance of the model to explain observed concentrations at all elevations is shown in Figure 4-9. This figure indicates that the modified van Ulden model is able to explain the concentrations at all heights measured downwind of the roadway very well. The correlation coefficients between the estimated concentrations at all elevations and their corresponding observed values are  $r^2 = 0.99$  for all cases. The model tends to underestimate low values of concentrations in the FLAT case and to overestimate low values of concentrations in the D690 and the D990 cases. These low values of concentrations correspond to the concentrations measured at high elevations and model's deficiency is attributed to the deviation of the estimated vertical concentration profiles from the observed ones.

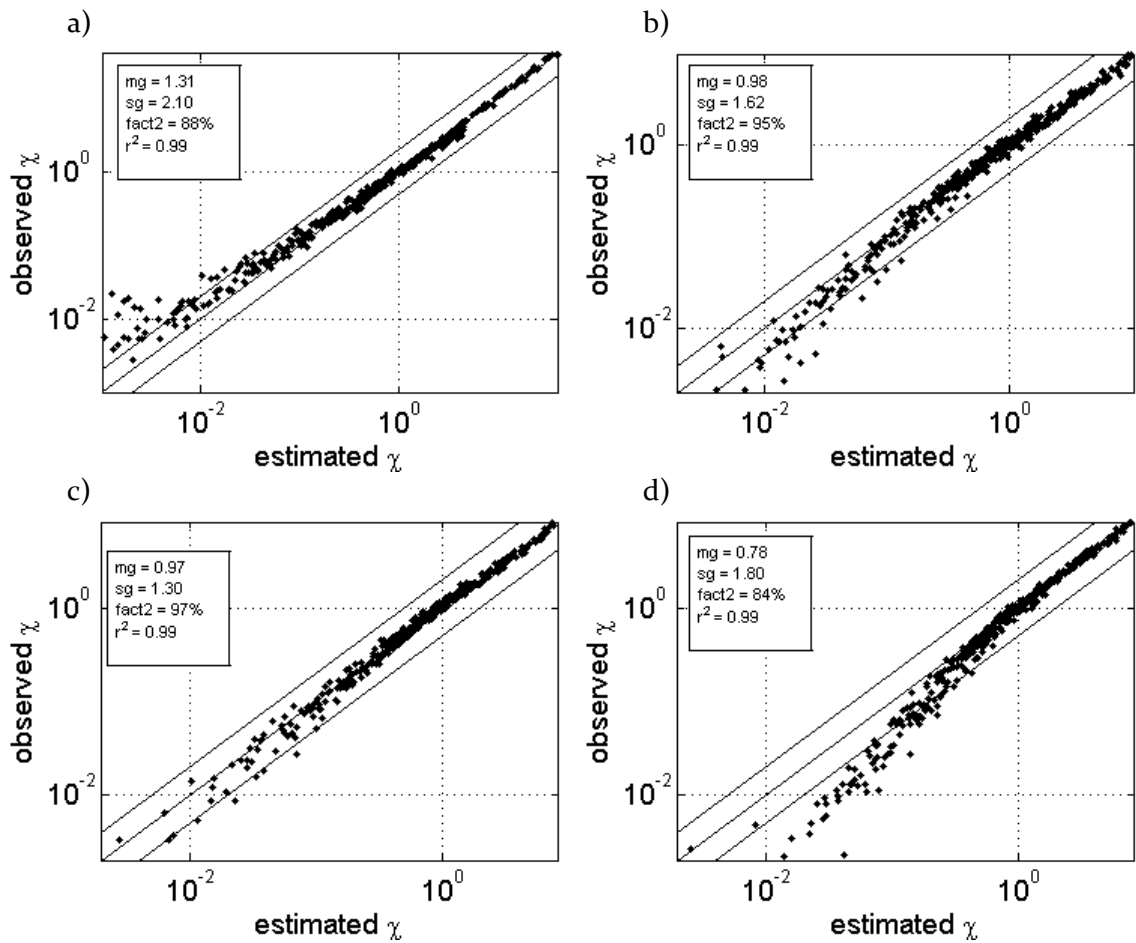


Figure 4-9- Comparison of modified van Ulden model estimates (with  $s=1.3$  and  $p=1/7$ ) with observed concentrations; a) FLAT case, b) D690 case, c) D630 case, and d) D990 case.

To investigate the model's capability to explain the vertical concentration profiles at multiple downwind distances, we plotted the estimated vertical concentration profiles against the observed ones at different downwind distances for the D690 case (Figure 4-10). This figure reinforces the fact that by modifying only two parameters, we are able to explain the observed concentrations downwind of the depressed roads at all heights.

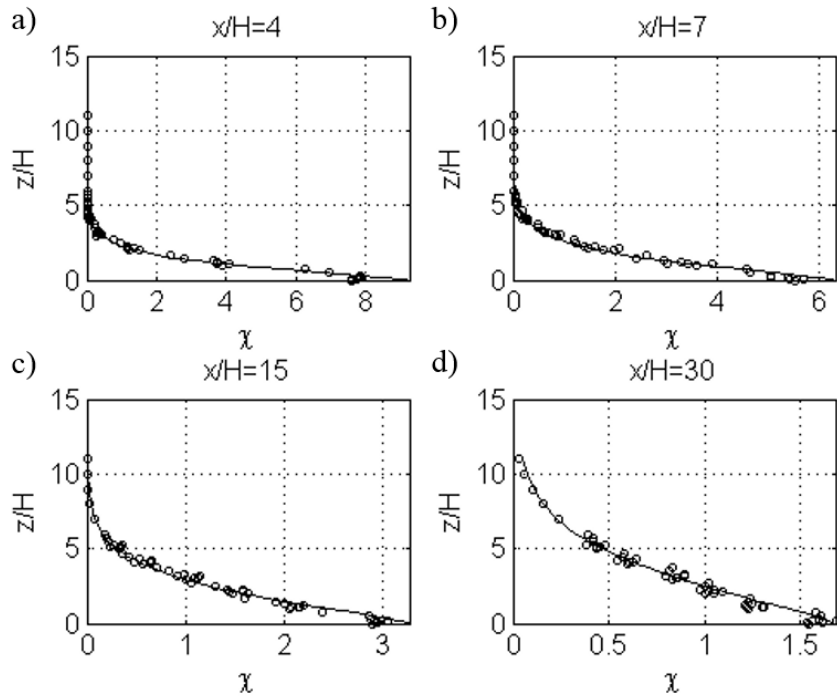


Figure 4-10- Comparison of the vertical concentration profiles at multiple downwind locations predicted by the modified van Ulden model (with  $s=1.3$  and  $p=1/4$ ) with those of the observations (D690 case).

Figure 4-11 compares the variation in the observed vertical concentration profiles of the FLAT and D690 cases at  $x = 3H$  with the corresponding modeled values. As expected, the model is able to capture the differences in vertical concentration profiles of different cases. The NMSE corresponding to the FLAT case is 0.05 and that for the D690 case is 0.02.

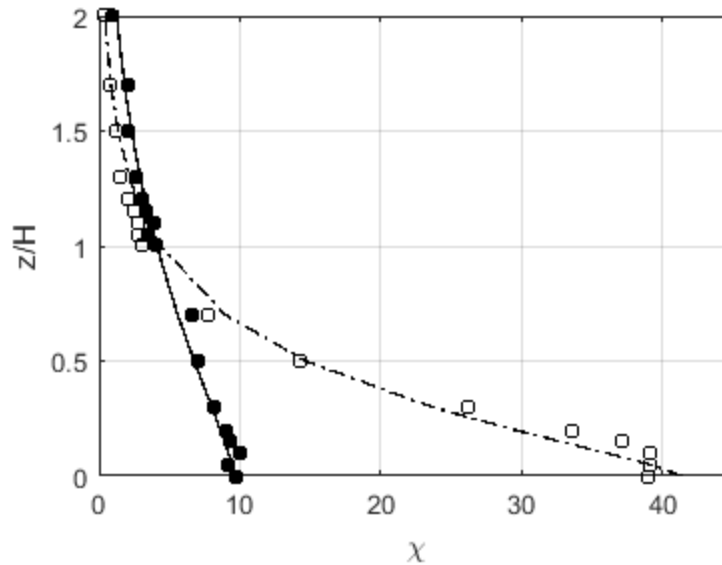


Figure 4-11- Performance of the modified van Ulden model in predicting concentration vertical profiles of different cases at  $x=3H$  (Open squares – measured flat terrain, solid circles – measured D690, dashed line – modeled flat terrain, and solid line – modeled D690).

#### 4.4.2 Modified RLINE model

As shown in Figure 4-8, concentrations estimated by a Gaussian dispersion model ( $s = 2$ ) deviate from observed concentrations at high elevations. However, from the exposure studies' point of view, it is important for a model to estimate concentrations at the breathing-level height. Therefore, we compare the modified RLINE model predictions with the concentrations observed below  $z = 6\text{ m}$  using the values listed in Table 4-3 (Figure 4-12). The results of this comparison show that the modified RLINE model is able to explain the concentrations measured below 6 m. The correlation coefficients between these estimated concentrations and their corresponding observed values are  $r^2 = 0.97$  or  $r^2 = 0.98$  for all cases.

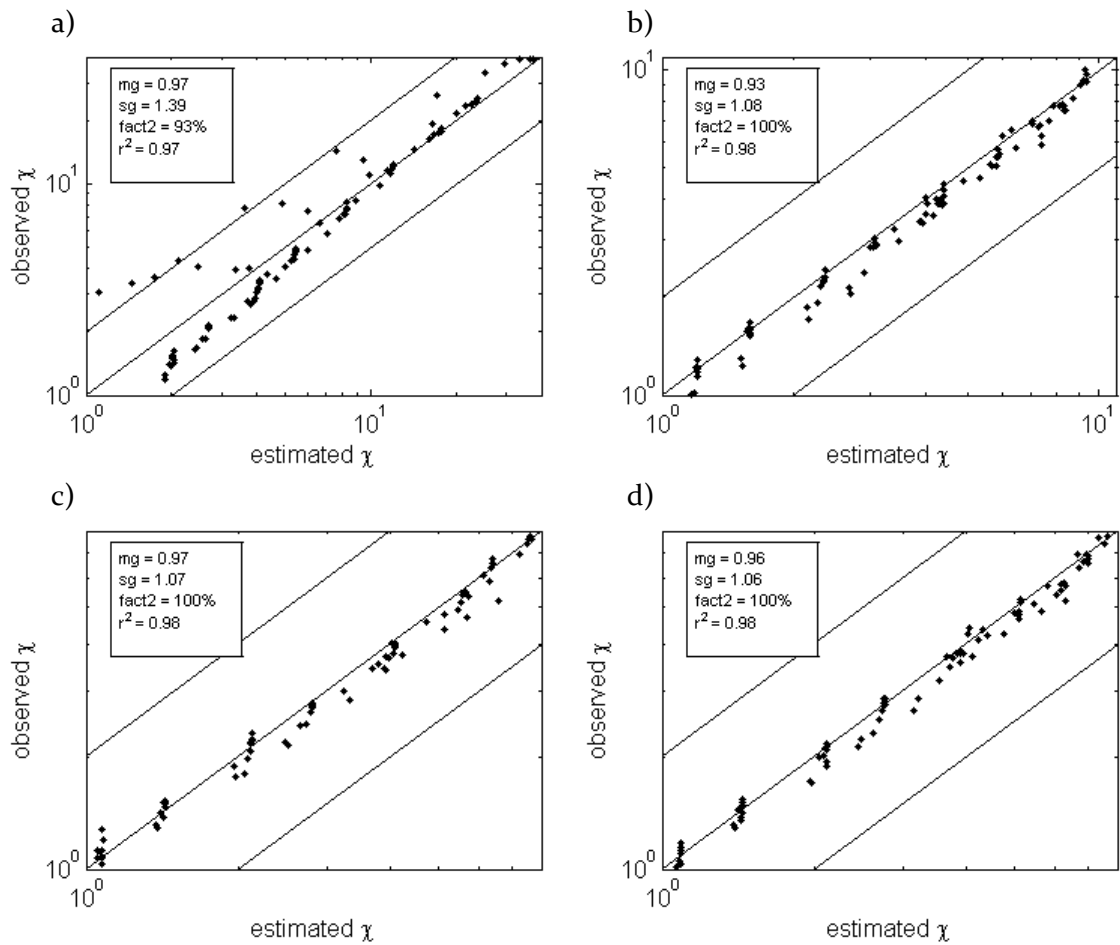


Figure 4-12- Performance of modified RLINE model in estimating concentrations below 6 m height for all downwind distances.

We also examined the modified RLINE model's capability to explain the measured vertical concentration profiles at multiple downwind distances for the D690 case (Figure 4-13). Comparing this figure with Figure 4-10 reinforces the fact that while the modified RLINE model is able to explain the downwind concentrations measured near ground-level, it does not perform well in estimating concentrations at higher elevations.

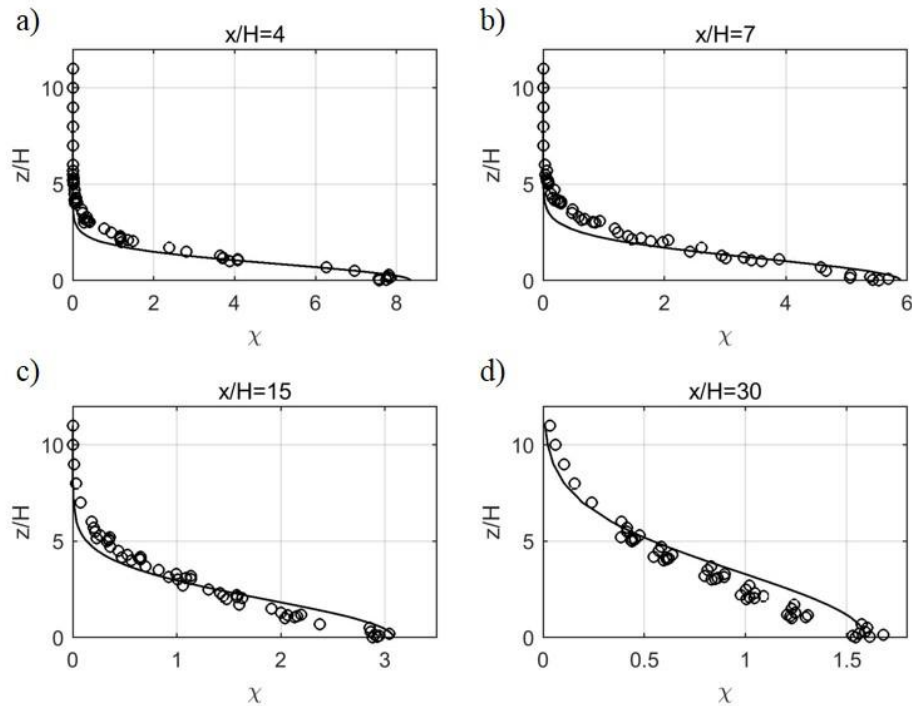


Figure 4-13- Comparison of the vertical concentration profiles at multiple downwind locations predicted by the modified RLINE model with those of the observations (D690 case).

## 4.5 Discussions

The major point made in this paper is that the effects of the complex flow patterns induced by the depressed road on dispersion can be simulated through simple modifications to a flat terrain model such as RLINE. This conclusion is supported by CALINE2 approach (Benson, 1992b) and another study (Venkatram et al., 2013a) that modeled concentrations measured next to a depressed highway in Las Vegas (Baldauf et al., 2013). Venkatram et al. (2013a) used a model to estimate the concentrations due to a line source (Venkatram and Horst, 2006) located on flat terrain with one modification: they accounted for the increase in vertical mixing of the plume by the depression by assuming that the initial vertical dispersion of the plume is equal to the depression of the road, which was approximately 5 m at the location of the measurements.

It is informative to compare the relative magnitudes of the mitigation effects induced by the depressed road with those related to solid barriers (Heist et al., 2009). We consider a road with one 6 m tall barrier downwind of the road and another with a 6 m tall solid barrier on each side of the road. Figure 4-14 shows the ratio of surface concentrations downwind of roads with one (two) sound barrier(s) to those downwind of the road in the D690 case, where the width of all roads are  $6H$  and the origin is located at the center of the simulated roads. The ratio of surface concentrations downwind of two sound barriers to those of the depressed road ranges from 0.80 to 1.08, while the ratio for the single downwind solid barrier ranges from 0.96 to 1.15 (Figure 4-14). The 6 m double sound barrier is more effective than the depressed road close to the road (up to  $x = 10H$ ) because of the strong recirculation zone behind the downwind solid barrier. The depressed road is more effective further downwind. The 6 m deep depressed road is more effective than a single 6 m downwind solid barrier for most downwind distances.

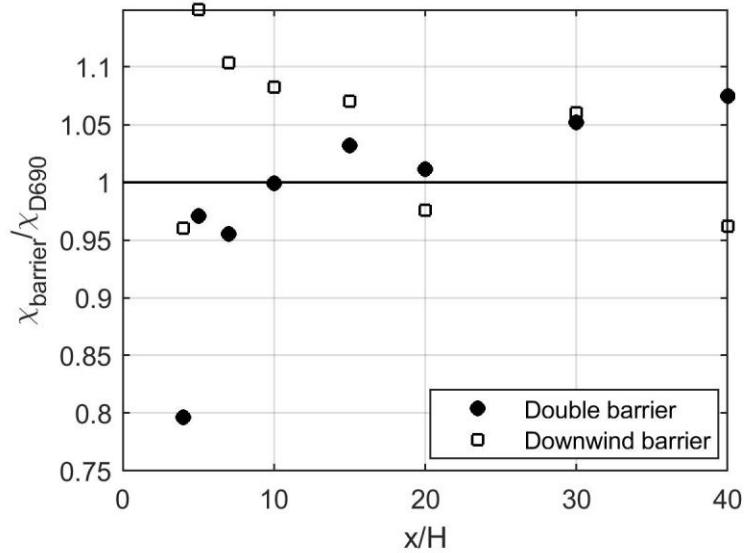


Figure 4-14- Ratio of surface concentrations downwind of barrier cases to those of D690 case. (Solid circle corresponds to 6 m double solid barriers and open square corresponds to 6 m downwind barrier).

## 4.6 Summary and conclusions

We analyze data from a wind-tunnel study (Heist et al., 2009) to suggest modifications to flat terrain dispersion models to account for the effects of depressed roadways on dispersion. By taking advantage of the detailed concentration and turbulence measurements in the wind tunnel, we first modify the parameters of a general flat terrain model (van Ulden, 1978) to explain the downwind concentration data. We then incorporate aspects of the first model into the more familiar RLINE (Snyder et al., 2013) model in an effort to add a depressed roadway algorithm.

We show that increasing the friction velocity and initial vertical dispersion in a flat terrain model proposed by van Ulden (1978) captures most of the effects induced by depressed roadways. It is observed that the van Ulden model with  $s = 1.3$  provides the best fit to the vertical concentration profiles observed downwind of roadways under neutral conditions.

Similar modifications to the RLINE model also provide good descriptions of near-surface concentrations measured downwind of the depressed roadway configurations in the wind tunnel (Heist et al., 2009). The friction velocity and initial vertical dispersion used to account for the effects of the depressed roadway increase with the depth of the depressed roadway. At this point, we do not have enough data to suggest a general formula to estimate these increases. However, the empirical results from our study are relevant to modeling the effects of depressed roadways that lie in the range of 6-9 m. The concentrations associated with emissions from these roadways can be estimated by increasing the friction velocity corresponding to flat terrain by a factor of 1.8 and using an initial vertical dispersion of about

4 m. This work provides a foundation for future studies that can result in development of a depressed roadway dispersion model formulation.

It should be noted that the results reported in this paper might be functions of atmospheric stability, a topic that is not examined in this paper. The width of the depression and the width of the roads are not taken into account in the model formulation because the widths of the roads in all cases were the same. But we expect that the mitigation effects of depressed roadways decrease as the ratio of the width to the depth of the depression ( $W/D$ ) becomes large, and street canyon effects become important when this ratio becomes small (Berkowicz, 2000; Schulte et al., 2015). For example, the height of the initial plume spread can be modeled using the approach in Schulte et al. (2015) so that  $h_0 = aD/(b + a_r)$  where  $a$  and  $b$  are empirical constants, and the aspect ratio,  $a_r = D/W$ . This formulation ensures that the initial plume spread is controlled by the depth,  $D$ , when  $W$  is large, and by  $W$  when  $D$  is relatively large as in a deep street canyon. For the depressed roads considered in this study, the empirical constants work out to be  $a = 0.30$  and  $b = 0.21$  for the data in Table 4-2 corresponding to the van Ulden model. Note that these are tentative values that only demonstrate the feasibility of the approach.

Concentrations on the road are not addressed in this study. However, previous studies have reported that channeling and eddy effects decrease the rate of pollutant transport out of the depressed zone, causing an increase of on highway concentrations (Benson, 1992). To evaluate the results of this study and to develop a complete dispersion model that estimates concentrations downwind of the depressed roads, it is necessary to assess the larger data sets that include a variety of aspect ratios.

# 5 Downscaling Satellite-Derived PM<sub>2.5</sub> Surface Concentration Fields Using Dispersion Models

## 5.1 Introduction

As discussed in chapter 1, researchers have attempted to estimate PM<sub>2.5</sub> surface concentrations using data from MODIS (Moderate Resolution Imaging Spectroradiometer) sensors. These sensors provide global AOD (Optical Aerosol Depth) on a twice-daily basis over land and ocean. They are located on NASA's Terra and Aqua polar-orbiting satellite platforms with daytime overpasses at 10:30 a.m. and 1:30 p.m. local time, respectively. However, the best resolution of these concentration fields is 3 km whereas for the health impact studies, estimation of PM<sub>2.5</sub> concentrations at much finer scales (10s – 100s of meters) are required. Kloog et al. (2011) incorporated land use regression (LUR) variables and meteorological variables into a generalized additive mixed model to estimate PM<sub>2.5</sub> concentrations using 10-km AOD measurements. They used the following parameters to estimate PM<sub>2.5</sub> concentrations at 10-km scale: percent of open spaces, elevation, major roads length, meteorological data, PM<sub>2.5</sub> point emissions, and area-source PM<sub>2.5</sub> emissions. Then they regressed the residuals for each air quality monitor against the local

land use (100 m) parameters specific for each monitor. These local land use parameters included traffic density, elevation, population density, and percent urban. This approach separated the regional and local PM<sub>2.5</sub> sources and partly enhanced the spatial resolution of the satellite-derived PM<sub>2.5</sub> surface concentrations; however, the performance of the method was not quantified. However, the land use regression models are not able to handle changes in emissions and cannot be used to examine the effects of emission changes on concentrations.

In this chapter, we describe a novel ‘downscaling’ method that adapts roadway dispersion models to yield the concentration gradients that are not captured by satellite maps. The approach depends on estimating emission factors by calibrating line source dispersion models against the observed concentrations of different air pollutants downwind of a major freeway in Los Angeles County. After calibrating the dispersion models, we incorporate them into the proposed downscaling system.

## **5.2 System design**

### **5.2.1 System overview**

The components of the system for enhancing the spatial resolution of the satellite-derived 3-km PM<sub>2.5</sub> concentration fields are shown in Figure 5-1. The proposed system has two main algorithms; first, B-Spline algorithm that generates daily 3-km PM<sub>2.5</sub> concentration fields from MODIS AOD, U.S. EPA ground-level monitor data, and North American Land Data Assimilation System (NLDAS) data products (Al-Hamdan et al., 2014); and second, a spatially-resolved dispersion model that estimates concentrations near roads. The B-Spline algorithm integrates data from the remote sensing satellite systems with the

monitoring network data to fill the temporal and spatial gaps found in ground-level monitor data. This algorithm has been exclusively discussed by Al-Hamdan et al. (2014) and only its final products are used in the proposed system. The second algorithm contains line source dispersion models that estimate concentrations near roads by using vehicle emissions and meteorological parameters. The dispersion models outputs are blended with the satellite-derived 3-km PM<sub>2.5</sub> concentration fields using the method that is described next. From now on, we refer to the 3-km grid that is generated by the first algorithm as ‘the grid’.

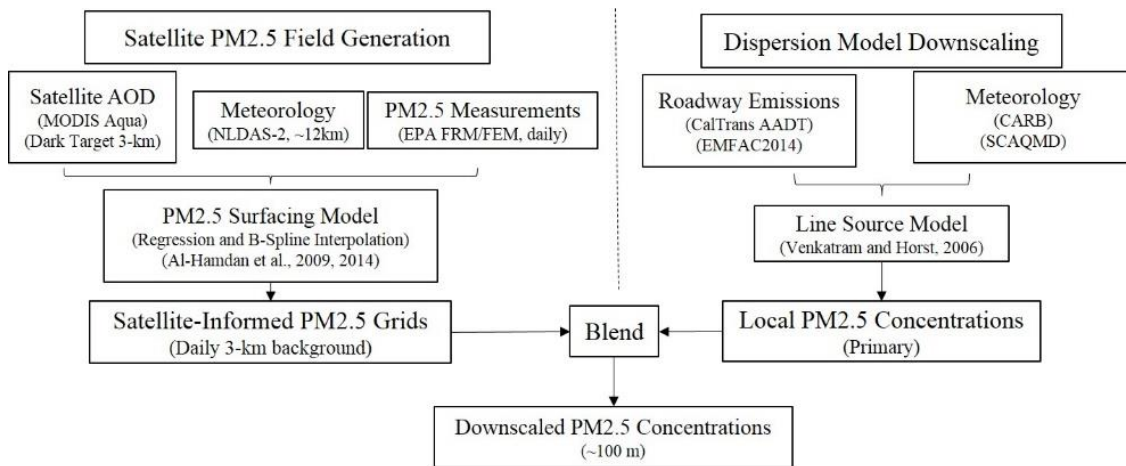


Figure 5-1- Overview of the system resulting in downscaled concentrations.

### 5.2.2 System description

The concentration at a receptor has two components: a regional component which is the contribution from sources outside the grid (regional sources), and a local component which is the contribution from sources within the grid (local sources). The main assumption of the downscaling system is that the regional components of all receptors within the grid are the same and the spatial variation of PM<sub>2.5</sub> concentrations within the grid is only due to the variation of the primary local components. Thus, if the grid is divided into  $n \times n$  subgrids, the total PM<sub>2.5</sub> concentration at the center of each subgrid (receptor) is:

$$C_i = C_{base} + \Delta C_i \quad (5-1)$$

where ‘ $i$ ’ denotes the subgrid number,  $C_{base}$  is the PM<sub>2.5</sub> regional component at the grid, and  $\Delta C_i$  is the local component at each subgrid. Note that  $C_{base}$  is the same for all receptors within the grid. To avoid double counting the contribution of primary PM<sub>2.5</sub> local sources, the spatial average of the PM<sub>2.5</sub> local components within the grid is subtracted from  $C_{sat}$ :

$$C_{base} = C_{sat} - \overline{\Delta C_i} \quad (5-2)$$

To model the PM<sub>2.5</sub> local component ( $\Delta C_i$ ) at the center of each subgrid, dispersion models are used to model local sources. PM<sub>2.5</sub> local sources consist of vehicular emissions and industrial emissions, while industrial emissions in urban areas are less than 3% of vehicular emission (Hasheminassab et al., 2014). Neglecting the role of industrial sources, the vehicular emissions within the grid are incorporated into the line source dispersion models to estimate daily average primary local PM<sub>2.5</sub> concentrations at the center of each subgrid. The development of the line source dispersion models is discussed in the next section.

It should be noted that the temporal resolution of a satellite-derived PM<sub>2.5</sub> concentration is 24 hours and that of the output of the dispersion models is 1 hour. Thus, the hourly concentrations are averaged over entire day and then incorporated into the system. In later sections, a full example of the system will be discussed in detail.

### 5.2.3 Dispersion models formulations

Two line source dispersion models were used to analyze the data collected near I-710 freeway. The first model is based on the simple barrier model introduced in section 2.4.1. The second model is based on the analytical approximation of the integral of a set of point

sources (Venkatram and Horst, 2006), which was discussed in section 2.1. We discuss the formulations of both dispersion models next.

### 5.2.3.1 Simple line source model

Based on equation 2-12, concentration at distance  $x$  downwind of a roadway with width  $W$  and presence of a solid barrier with height  $H$  is equal to:

$$C_s = \frac{q}{au_*W} \ln \left( 1 + \frac{W}{H \frac{U(H/2)}{au_*} \cos \theta + x} \right) \quad (5-3)$$

where  $q$  is the emission rate per unit length,  $u_*$  is surface friction velocity,  $H$  is the barrier height,  $U(H/2)$  is wind speed evaluated at middle of the barrier,  $\theta$  is the angle between wind direction and perpendicular to the road, and  $a = 0.71$  is a constant. Although this model was developed for concentrations downwind of roads with solid barriers, we use it as a reference model by assuming that the concentrations are well-mixed below  $h_0$ , the initial vertical plume spread, instead of  $H$ . Therefore, the concentration is equal to:

$$C_s = \frac{q}{au_*W} \ln \left( 1 + \frac{W}{h_0 \frac{U(h_0/2)}{au_*} \cos \theta + x} \right) \quad (5-4)$$

where the width of the I-710 freeway was 40 m at the study area, and  $h_0$  was assumed to be 2 m.

Additionally, for light wind, stable conditions, when  $u_*$  is generally small (less than 0.1 m/s), the friction velocity is adjusted based on the work of Qian and Venkatram (2011). Qian and Venkatram recommended the following modification to the friction velocity for cases of low  $u_*$  and stable atmospheric conditions ( $L > 0$ ):

$$u_{*new} = \frac{u_*}{1 - \exp\left(-\frac{2}{r}\right)} \quad (5-5)$$

where  $r$  is:

$$r = \frac{U_{crit}}{U_r} \quad (5-6)$$

$$U_{crit} = \frac{2u_0}{C_{DN}^{1/4}} \quad (5-7)$$

$$u_0 = \sqrt{\frac{\beta g(z_r - dh - z_0)T_*}{T_0}} \quad (5-8)$$

and

$$C_{DN} = \frac{\kappa^2}{\left(\ln\left(\frac{z_r - dh}{z_0}\right)\right)^2} \quad (5-9)$$

In these equations,  $U_r$  is the wind speed measured at the reference height,  $z_r$ ,  $\beta = 4.7$ ,  $g = 9.81 \text{ m/s}^2$  is the gravitational acceleration,  $dh$  is the canopy displacement height,  $z_0$  is the roughness length,  $T_* = \overline{w'T'}/u_* = 0.08 \text{ K}$  where  $\overline{w'T'}$  is the mean vertical temperature flux,  $T_0$  is the temperature measured at the reference height, and  $\kappa = 0.4$  is the von Karman constant. This simple model which assumes neutral atmospheric stability conditions during all times serves as a reference model.

### 5.2.3.2 Analytical line source model

This model is based on the work of Venkatram and Horst (2006), which analytically approximates concentrations downwind of a line source. This model was discussed in section 2.1. Concentration is estimated based on equations 2-2, 2-4, and 2-5:

$$C(x_r, y_r, z_r) = \frac{1}{2} \frac{q}{\cos \theta} F_z \left( \frac{x_r}{\cos \theta}, z_r \right) [\text{erf}(t_1) - \text{erf}(t_2)] \quad (5-10)$$

where

$$t_i = \frac{(y_r - y_i) \cos \theta - x \sin \theta}{\sqrt{2} \sigma_y (x_r \cos \theta + (y_r - y_i) \sin \theta)} \quad (5-11)$$

and

$$= \frac{1}{U(\bar{z})\sqrt{2\pi}\sigma_z(x_r)} \left[ \exp\left(-\frac{F_z(x_r, z_r)}{2\sigma_z^2(x_r)}\right) + \exp\left(-\frac{(z_r + z_s)^2}{2\sigma_z^2(x_r)}\right) \right] \quad (5-12)$$

The vertical and horizontal plume spread formulations are based on the work of Venkatram et al. (2013) (equations 2-6 and 2-7). Since the road is considered to be very long compared to the distance of receptors from highway,  $\text{erf}(t_1) - \text{erf}(t_2) = 1 - (-1) = 2$  and equation (5-10) is simplified to:

$$C(x_r, y_r, z_r) = \frac{q}{\cos \theta} F_z\left(\frac{x_r}{\cos \theta}, z_r\right) \quad (5-13)$$

For small wind speeds under stable conditions,  $u_*$  is adjusted based on the work of Qian and Venkatram (2011).

After comparison of the model estimates to the observed concentrations, it is found that the model performance improves if the atmospheric stability is assumed to be neutral during all the time, similar to the assumption in the simple line source model.

## 5.2.4 Dispersion models inputs

### 5.2.4.1 Roadway emissions

One of the inputs to the line source dispersion models is the roadway emissions. Increase in roadway emissions leads to increase in traffic related concentrations next to the roadway. The unit of the roadway emission is [# of species.m<sup>-1</sup>.vehicle<sup>-1</sup>] or [mass of species.m<sup>-1</sup>.vehicle<sup>-1</sup>] and its magnitude is given by  $T_r e_f$  where  $T_r$  (vehicle.s<sup>-1</sup>) is the traffic flow rate and  $e_f$  is the emission factor (# of species.m<sup>-1</sup> or mass of species.m<sup>-1</sup>) per vehicle. Therefore, in order to estimate roadway emissions, it is essential to estimate the traffic flow rate and the emission factor of the species of interest.

Traffic flow rates in the form of Annual Average Daily Traffic (AADT) for all traffic sensors on the California state highway system, along with their locations are stored on the CalTrans GIS data library<sup>1</sup>. AADT is defined as the total volume of vehicle traffic of a freeway for a year divided by 365 days. Currently, the latest uploaded AADT data correspond to the year 2015. Using the locations of the traffic sensors, we determine the freeway locations within California. Figure 5-2a shows the major roadways within the South Coast air basin by simply drawing straight lines between the adjacent traffic sensors on each freeway. Figure 5-2b focuses on the freeways in vicinity of Riverside, CA. In the downscaling system, the AADT data are used to estimate the primary PM<sub>2.5</sub> emissions from roadways.

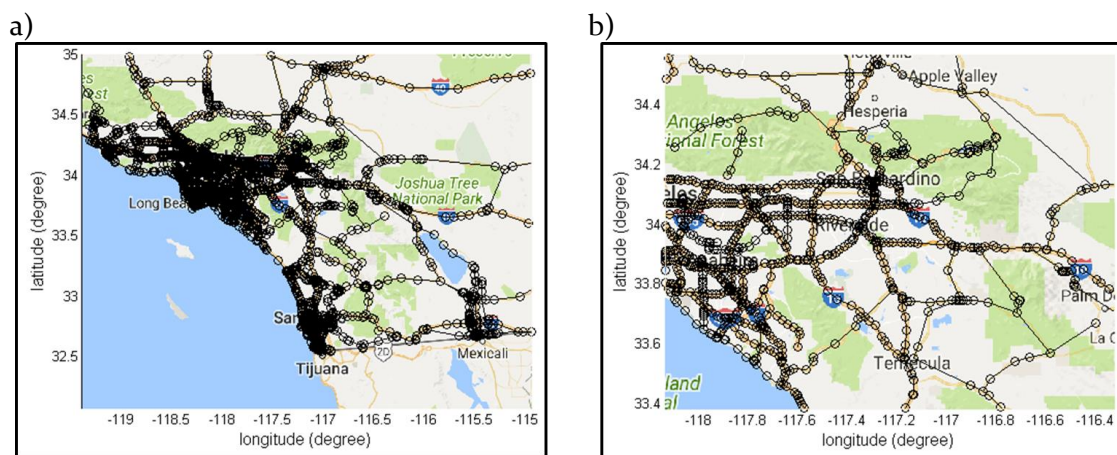


Figure 5-2- Major line sources implemented into the line-source dispersion model for the South Coast air basin. Circles indicate locations of mileposts where AADT is measured. Left panel, entire area; Right panel, zoomed-in over area around Riverside, CA.

Additionally, five-minute averages of traffic flow rates passing each lane of major roads within California are stored on the CalTrans Performance Measurement System<sup>2</sup>. The detectors record the number of cars and trucks separately. For the purpose of assessing the

<sup>1</sup> <http://www.dot.ca.gov/hq/tsip/gis/datalibrary/#Highway>

<sup>2</sup> [www.pems.dot.ca.gov](http://www.pems.dot.ca.gov)

dispersion models performances, we use the traffic flow rate reported by the CalTrans PeMS.

Because of the large uncertainty in emission factors of different species, we treat the emission factors as unknown parameters whose values are obtained by fitting the model estimates to measured concentration values. If the estimated emission factors fall within the range reported by literature, model performance is deemed to be acceptable.

#### **5.2.4.2 Meteorological parameters**

The line source dispersion models use the surface meteorology provided by the AERMET model (the meteorological preprocessor for AERMOD; (Cimorelli et al., 2005)). The South Coast Air Quality Management District (SCAQMD) website hosts these surface meteorology data<sup>1</sup> from 24 stations throughout the South Coast air basin. These files are developed using the U.S. EPA's AERMET processor and pre-processors AERMINUTE Version 15181 and AERSURFACE Version 13016.

For assessment of the line source dispersion models, we use the SCAQMD data for winter 2009. We also run AERMET to produce the surface meteorology data for summer 2009. This will be discussed in more detail in later sections.

#### **5.2.5 Dispersion model outputs**

The output of the line source dispersion models are the local primary component of the PM<sub>2.5</sub> concentrations. The outputs can be estimated at any point (receptor) within the 3-km grid. Depending on the sparseness of the receptors within the 3-km grid, the final spatial resolution of the system's output is determined.

---

<sup>1</sup> <http://www.aqmd.gov/home/air-quality/air-quality-data-studies/meteorological-data/data-for-aermod>.

### 5.3 I-710 field study

To calibrate the line source dispersion models, we used the data collected in a field study conducted next to a busy freeway in Long Beach, CA. This field study had two main advantages over data from the U.S. EPA air quality monitors: 1) near-road concentrations of different pollutants were measured (at 15 m and 80 m away from the east edge of the freeway), and 2) background concentrations of the pollutants were measured far from the influence of the freeway. Thus, by using this dataset we are able to explore the contribution of freeway emissions to near-road concentrations and to assess the performance of the line source dispersion models, which estimate concentrations due to freeway vehicular emissions.

In the winter and summer of 2009, South Coast Air Quality Management District (SCAQMD) conducted two field studies in the vicinity of the Interstate 710 freeway (I-710), near the intersection with North Long Beach Boulevard (Figure 5-3). Sampling was conducted at two monitoring stations located 15 meters and 80 meters east of the freeway ('near' and 'far' site, respectively). A third station, far from the influence of the I-710 was operated in Carson, CA, next to Del Amo Elementary School. This station was 1.8 km east and 1 km north of the I-405 freeway. It was expected that this station represents background concentrations in the area of study.



Figure 5-3- Aerial view of the sampling area showing the locations of the two monitoring stations near the I-710 freeway (“near” and “far” sites), and the background site in Del Amo. Adapted from (Polidori and Fine, 2012).

Carson and Long Beach are located in southwestern Los Angeles County. The I-710 freeway is a nine-lane freeway with 40 m width at the study site and connects the ports of Long Beach and San Pedro to the shipping yards in East Los Angeles. It has average traffic flow rate of 185,000 vehicles/day. On this freeway, heavy duty diesel trucks account for about 20% of the total number of vehicles (Polidori and Fine, 2012). On the I-405 freeway, the other major freeway in the area, the local traffic mix includes predominantly light-duty gasoline-powered vehicles.

The I-710 freeway is at the same level as the surroundings. The heading of the freeway is  $30^\circ$  and thus the wind direction perpendicular to the freeway is  $300^\circ$  true to north. The historical wind data collected by weather stations near the study site indicated a dominant westerly wind during the daytime which meant that the east-side of the freeway can be considered downwind.

Winter campaign occurred from 01/29/2009 to 03/11/2009 and summer campaign was conducted from 06/30/2009 to 08/19/2009. Both continuous and integrated measurement techniques were used to monitor the ambient concentration of the particle and gaseous

pollutants listed in Table 5-1. It should be noted that integrated 24-hour PM<sub>2.5</sub>, PM<sub>10</sub>, EC, and OC samples were collected daily. Thus, the temporal resolution of the PM<sub>2.5</sub> and PM<sub>10</sub> concentrations is 24 hours. On the other hand, continuous measurements of NO<sub>x</sub>, CO, and UFP concentrations were made every minute and those of BC were made every five minutes. The continuous data were averaged to hourly concentrations to facilitate comparison among sites. Hourly BC data obtained from an Aethalometer with a PM<sub>2.5</sub> selective inlet were used to measure the black carbon content of the PM<sub>2.5</sub>. The details of the measurements and the instruments used in this study are explained in detail in Polidori and Fine (2012).

Table 5-1- List of the particle and gaseous species monitored during this study. Both continuous and integrated measurement techniques were used to collect/monitor all targeted pollutants. Adapted from Polidori and Fine (2012).

<b>Measured Pollutants</b>			
<i>Integrated Measurements</i>		<i>Continuous Measurements</i>	
PM <sub>10</sub> mass	PM <sub>2.5</sub> mass	Nitrogen Oxides (NO, NO <sub>2</sub> , NO <sub>x</sub> )	Black Carbon (BC)
Organic Carbon (OC)	TSP Lead	Ultrafine Particle number (UFP)	Carbon Monoxide (CO)
Elemental Carbon (EC)	Volatile Organic Compounds (VOC)		

Wind speed and wind direction were also measured by a meteorological tower during the summer campaign at the ‘far’ site.

The traffic activity data were taken from the CalTrans PeMS website<sup>1</sup>. Since traffic activity data were not available at the time of the study, we used the traffic flow values corresponding to the same time period of 2011, when the sensors were operational. However, it should be noted that the traffic profiles are not similar for all days. Traffic data are

<sup>1</sup> [www.pems.dot.ca.gov](http://www.pems.dot.ca.gov)

separated into weekday traffic data and weekend traffic data and are averaged over each group. The traffic data at any time during the measurements can be estimated by using the average traffic flow rate of 2011. The average and standard deviation of diurnal variation of average vehicle and truck traffic flow rate for weekdays and weekends of summer and winter 2011 are shown in Figure 5-4. This figure clearly indicates that the LDV flow rate during weekdays peaks at 7 AM in the morning and at 4 PM in the evening. During weekends, the LDV traffic flow peaks at 2 PM during winter 2011 and sometime between 1 PM and 4 PM during summer 2011. In winter, LDV traffic flow rate is greater during weekdays than during weekends between 5 AM and 8 PM, and in summer this time period becomes 4 AM to 8 PM. HDV traffic flow peaks at 10 AM during winter and summer 2011. HDV traffic flow during weekdays is clearly greater than those during weekends.

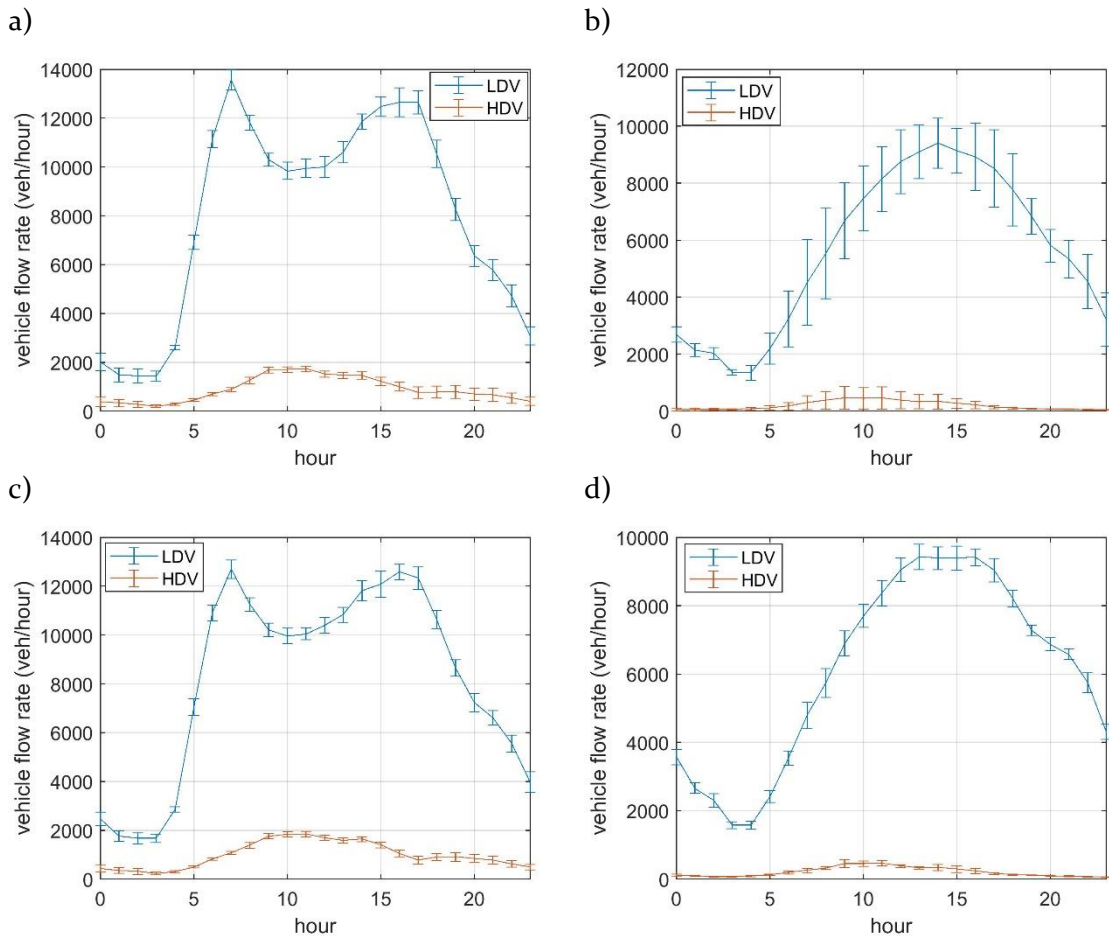


Figure 5-4- Diurnal variation of average traffic flow rate of Light Duty Vehicles (LDV) and High Duty Vehicles (HDV) for a) winter weekdays, b) winter weekends, c) summer weekdays, and d) summer weekends. Error bars indicate one standard deviation.

## 5.4 Results of the field study

### 5.4.1 Meteorology

The wind rose for the summer campaign along with the freeway direction is shown in Figure 5-5. It indicates the presence of a distinct westerly wind, which is typical for this part of the South Coast air basin. Precipitation data during the winter campaign showed an unusually high number of precipitation days. Based on Polidori and Fine (2012), the following days were rainy: 02/05/2009 – 02/09/2009, 02/13/2009, 02/15/2009 – 02/17/2009,

and 03/04/2009. Because the wet deposition mechanisms are not included in the dispersion models, we did not model concentrations during the rainy days.

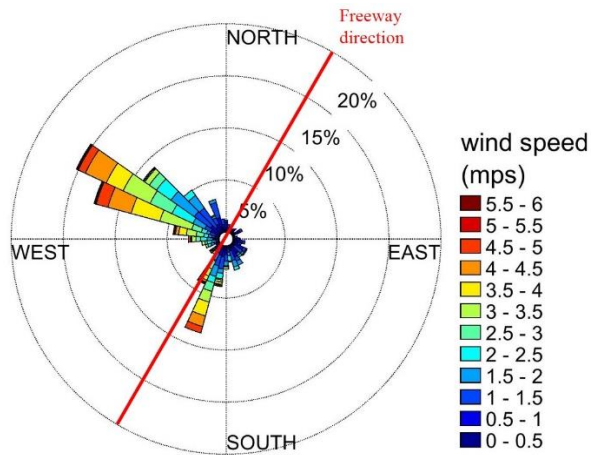


Figure 5-5- Observed wind rose measured by the upwind 3-D sonic anemometer along with freeway direction.

#### 5.4.2 Fine particulate matter, black carbon content, and NOx concentrations

The measured PM<sub>2.5</sub> mass concentrations are also analyzed for spatial and seasonal differences (Table 5-2). Because a sampler was not available at the Del Amo site, PM<sub>2.5</sub> data are not available at this station. However, background PM<sub>2.5</sub> levels for both the winter and summer campaigns were obtained from the North Long Beach site (Polidori and Fine, 2012), one of AQMD's network stations located away from the influence of the I-710, but in the same geographical area. As expected, the highest mean and median concentrations of all species occurred at the 'near' site and decreased to the 'far' site concentrations, which were higher than the background concentrations.

The PM<sub>2.5</sub> concentrations measured at the 'near' and 'far' site showed around 35% and 23% increase relative to the background concentrations, respectively, which indicate that the background concentrations constitute a major fraction of the PM<sub>2.5</sub> concentrations near the freeway. Conversely, the ambient concentrations of BC reflected higher

contribution from traffic activity. The median of the BC concentrations measured at the ‘near’ and the ‘far’ sites were 100% and 25% higher than the median of the background concentrations. The large influence of the roadway activity on concentrations downwind of the freeway could be contributed to the large emissions of BC from high duty diesel trucks. The median of ambient concentrations of NOx at the near and the far site were observed to be 3.62 and 2.20 times the median of the background concentrations, respectively, which indicates a large contribution from the roadway emissions to NOx concentrations.

Table 5-2- Average and median fine particulate matter (PM<sub>2.5</sub>), black carbon (BC), and NOx concentrations at the “near”, “far” and background stations during the winter and summer campaigns. Minimum (Min) and maximum (Max) values, standard deviations (SD), and the total number of valid samples (Valid N) are also included. Background PM<sub>2.5</sub>, BC, and NOx data were measured at the North Long Beach station, Del Amo station, and Del Amo station respectively. (Adapted from Polidori and Fine (2012))

	15 m	80 m	Background		15 m	80 m	Background
<i>PM<sub>2.5</sub> (µg/m<sup>3</sup>) - WINTER</i>				<i>PM<sub>2.5</sub> (µg/m<sup>3</sup>) - SUMMER</i>			
<b>Average</b>	12.6	11.5	9.59	<b>Average</b>	15.2	14.0	12.2
<b>Median</b>	12.1	10.6	7.96	<b>Median</b>	14.2	13.4	11.8
<b>SD</b>	5.72	5.34	4.63	<b>SD</b>	4.83	4.70	4.18
<b>Min</b>	3.21	3.29	2.84	<b>Min</b>	7.29	4.58	4.59
<b>Max</b>	26.2	25.2	21.1	<b>Max</b>	28.6	25.4	23.7
<b>Valid N</b>	36	36	35	<b>Valid N</b>	41	34	43
<i>BC (µg/m<sup>3</sup>) - WINTER</i>				<i>BC (µg/m<sup>3</sup>) - SUMMER</i>			
<b>Average</b>	4.94	3.59	2.24	<b>Average</b>	2.50	1.39	0.98
<b>Median</b>	3.99	2.55	1.42	<b>Median</b>	2.07	1.23	0.74
<b>SD</b>	4.10	3.12	2.12	<b>SD</b>	1.80	0.81	0.81
<b>Min</b>	0.05	0.06	0.04	<b>Min</b>	0.15	0.14	0.04
<b>Max</b>	26.0	18.6	13.8	<b>Max</b>	14.0	8.06	6.71
<b>Valid N</b>	978	955	921	<b>Valid N</b>	1194	1185	846
<i>NOx (ppb) - Winter</i>				<i>NOx (ppb) - Summer</i>			
<b>Average</b>	108	80.7	45.3	<b>Average</b>	50.4	26.0	15.0
<b>Median</b>	91.2	56.9	25.5	<b>Median</b>	39.5	23.5	10.8
<b>SD</b>	88.0	75.6	48.0	<b>SD</b>	37.4	17.0	13.1
<b>Min</b>	3.72	2.82	2.34	<b>Min</b>	2.51	1.78	2.89
<b>Max</b>	496	462	305	<b>Max</b>	295	189	128
<b>Valid N</b>	907	906	832	<b>Valid N</b>	1335	1176	809

Since continuous measurements of PM<sub>2.5</sub> concentrations are not available and also the Del Amo station was not operating to measure the background PM<sub>2.5</sub> concentrations, the

line source dispersion models are calibrated to estimate continuous BC and NO<sub>x</sub> measurements. To analyze the continuous measurements of BC and NO<sub>x</sub> in more detail, time series of their concentrations are plotted in Figure 5-6. During both campaigns, 1-hr concentrations of both species measured at three monitoring stations tracked each other over time. For example, the highest concentrations at the 'near' site occurred at the same time that the highest concentrations at the Del Amo station were observed. This suggests that the Del Amo station may be influenced by local traffic emissions and may not well represent the background concentrations. To partly resolve this issue, we modeled the concentrations only when the measured concentration at the 'near' site was greater than 3 times the concentration measured at the Del Amo station. It is worth noting that very small concentrations were observed during intense precipitation between 02/05/2009 and 02/07/2009 (Figure 5-6).

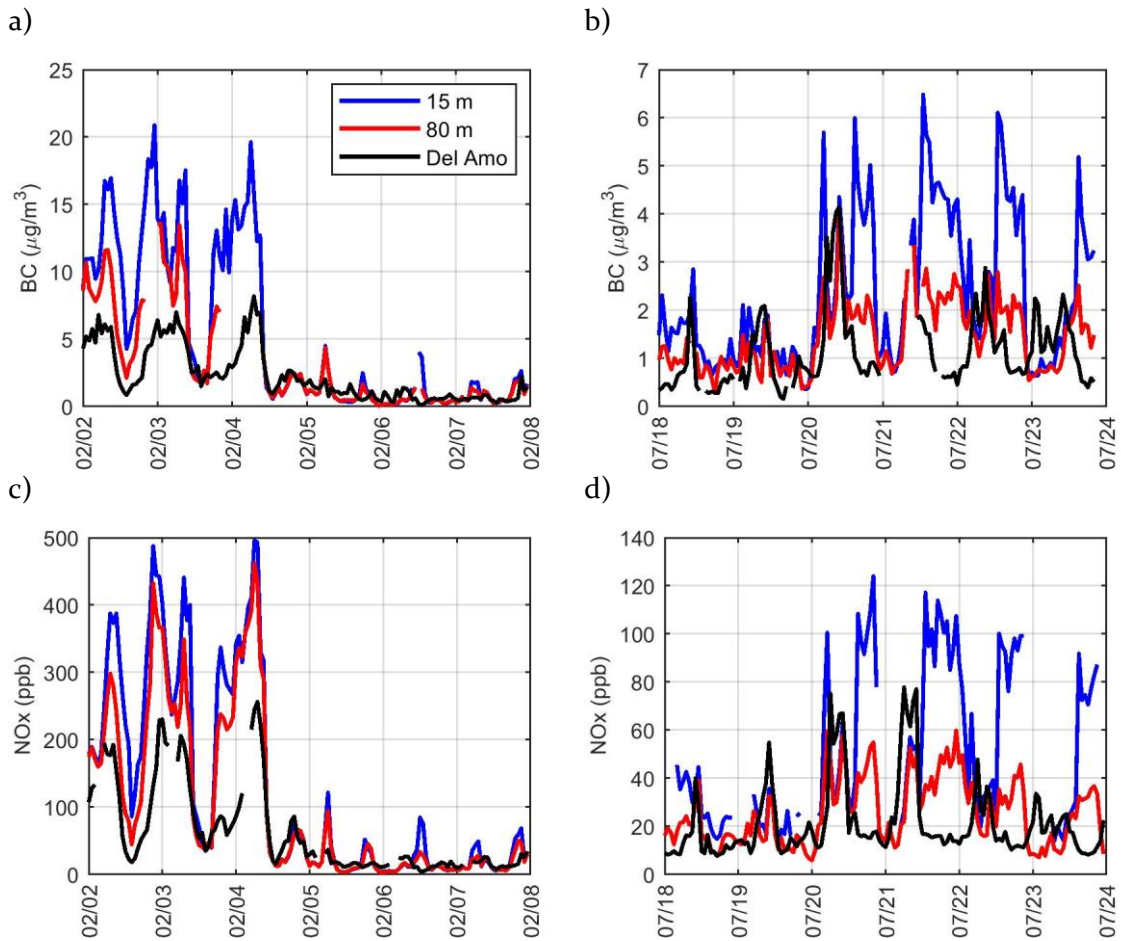


Figure 5-6- Representative 1-hr average of a) winter BC, b) summer BC, c) winter NOx, and d) summer NOx, at the 'near', 'far', and Del Amo stations.

## 5.5 Dispersion modeling results

The BC and NOx emission factors are highly uncertain. As discussed before, we treat the emission factors as unknown parameters whose values are obtained by fitting model estimates to measured concentrations. Using each model, we estimate individual species' emission factors for different seasons and different atmospheric stability conditions. If the models perform well, the resulting emission factors for different stabilities within each season should be of the same order and lie within the reported range of emission factors in literature.

A comprehensive study quantified the emission factors of several pollutants for 64 gasoline vehicles and 5 diesel vehicles by conducting different types of test cycles on vehicles (May et al., 2014). The pollutants studied in this work included CO, NO<sub>x</sub>, PM, BC, and Organic Carbon (OC). Two of the tests on gasoline vehicles were simulating the freeway conditions with cruise driving patterns. Ten tests on diesel vehicles were simulating heavy heavy-duty diesel truck (HHDDT) with 50 mph speed. Emission factors (mg.kg<sup>-1</sup> of fuel) of different pollutants for these tests were reported along with the fuel economy of each vehicle (mpg) to convert the emission factors to emission rates (ER) (g.km<sup>-1</sup>). The results show that BC emission rate of gasoline vehicles can be of the order of 10 different (Table 5-3). Moreover, ER<sub>BC</sub> of diesel vehicles can be even lower than the limit of detection (LOD), or can be as large as 0.049 g.km<sup>-1</sup>.

Another study reported that the BC emission factor of LDV and HDDT are  $30 \pm 2$  mg.kg<sup>-1</sup> and  $1440 \pm 160$  mg.kg<sup>-1</sup>, respectively (Miguel et al., 1998). Assuming that the fuel economy of LDV's is around 20 mpg and that of HDDT's is around 8 mpg, the BC emission rates of LDV's and HDDT's are  $3 \pm 0.2$  mg.km<sup>-1</sup> and  $360 \pm 40$  mg.km<sup>-1</sup>, respectively. Because of the large uncertainty reported in literature, for BC concentration analysis, we use the ratio  $0.36/0.003 = 120$  to convert the number of trucks to the equivalent number of LDV's.

Considering that NO<sub>x</sub> emission factor varies significantly for different types of cars and different certificates (Table 5-3), EMFAC Model inventory data reports NO<sub>x</sub> emission factor (California Air Resources Board, 2011) for the LDV's and HDV's averaged over mileage for the fleet operating in Los Angeles County. Based on EMFAC, NO<sub>x</sub> emission factor for LDV's and HDV's are estimated to be 0.17 g.km<sup>-1</sup> and 3.18 g.km<sup>-1</sup>, respectively. In our analysis, we

assume the contribution of HDV's to NO<sub>x</sub> concentrations is  $3.18/0.17 = 18.70$  times that of LDV's.

The performance of the models are evaluated using the geometric mean ( $m_g$ ), standard deviation of the residuals between the observations and predictions ( $s_g$ ), the fraction of data points that lie within a factor of two of the observations (*fact2*), and the correlation coefficient between the observations and predictions ( $r^2$ ). These statistical parameters were defined in section 2.5.

Table 5-3- Gasoline and diesel vehicle emissions under test cycles similar to cruise driving patterns.

Vehicle type	Vehicle name	Test ID number	Model year	Engine Size (L)	Aftertreatment	Fuel economy (mpg)	EF <sub>BC</sub> (mg/kg)	EF <sub>NOx</sub> (g/kg)	ER <sub>BC</sub> (mg/km)	ER <sub>NOx</sub> (g/km)
Gasoline	LEV2-6	1032345	2011	3.6	NA	23.9	3.85	0.36	0.03	0.03
	LEV1-3	1032348	1998	3.0	NA	24.2	5.07	4.13	0.34	0.34
Diesel	D2	1426	2007	12.8	DOC+DPF+SCR	5.9	<LOD	7.93	<LOD	2.68
		1427				5.8	0.4	7.76	0.14	2.67
	D3	1435	2006	10.8	none	7.6	161	12.3	42.29	3.23
		1437				7.6	164	12.4	43.08	3.26
		1440				7.5	185	12.7	49.24	3.38
		1444				7.7	171	11.4	44.33	2.96
	D1	1453	2010	14.9	DOC+DPF	5.1	0.2	1.78	0.08	0.70
		1454				5.1	0.2	1.86	0.08	0.73
		1462				5.1	<LOD	2.10	<LOD	0.82
		1463				5.1	0.4	2.37	0.16	0.93

### 5.5.1 Simple line source model assessment

The performance of the simple line source model in estimating BC concentrations during winter and summer at ‘near’ and ‘far’ stations is shown in Figure 5-7. The model estimates the emission rate of LDV’s during winter to be 3.46 mg.km<sup>-1</sup> and 4.13 mg.km<sup>-1</sup> during unstable and stable conditions, respectively (Figure 5-7a and b). The two emission rates are within the range of the reported emission rates in literature and the difference between these two emission rates is less than 15% which is acceptable considering the large uncertainty in emission factor estimations.

The model is able to estimate winter concentrations downwind of the freeway with  $r^2 = 0.54$  and  $r^2 = 0.29$  during unstable and stable conditions, respectively. The estimated winter concentrations are within a factor of two of the observations for 88% and 72% of the time during unstable and stable conditions, respectively.

The emission rate of LDV’s during summer is estimated to be 2.39 mg.km<sup>-1</sup> and 1.99 mg.km<sup>-1</sup> during unstable and stable conditions, respectively (Figure 5-7c and d). The two emission rates are also within the range of the reported emission rates in literature and the difference between these two emission rates is less than 17% which is also acceptable.

The model is able to estimate summer concentrations downwind of the freeway with  $r^2 = 0.54$  and  $r^2 = 0.32$  during unstable and stable conditions, respectively. The estimated winter concentrations are within a factor of two of the observations for 89% and 82% of the time during unstable and stable conditions, respectively.

The average BC emission rate during winter is 1.7 times that during summer. This is consistent with findings in literature where higher emission rates of particulate matters during colder temperatures are reported (Christenson et al., 2014). It should be noted that

the average temperature during winter campaign is 13°C and that during summer campaign is 22°C.

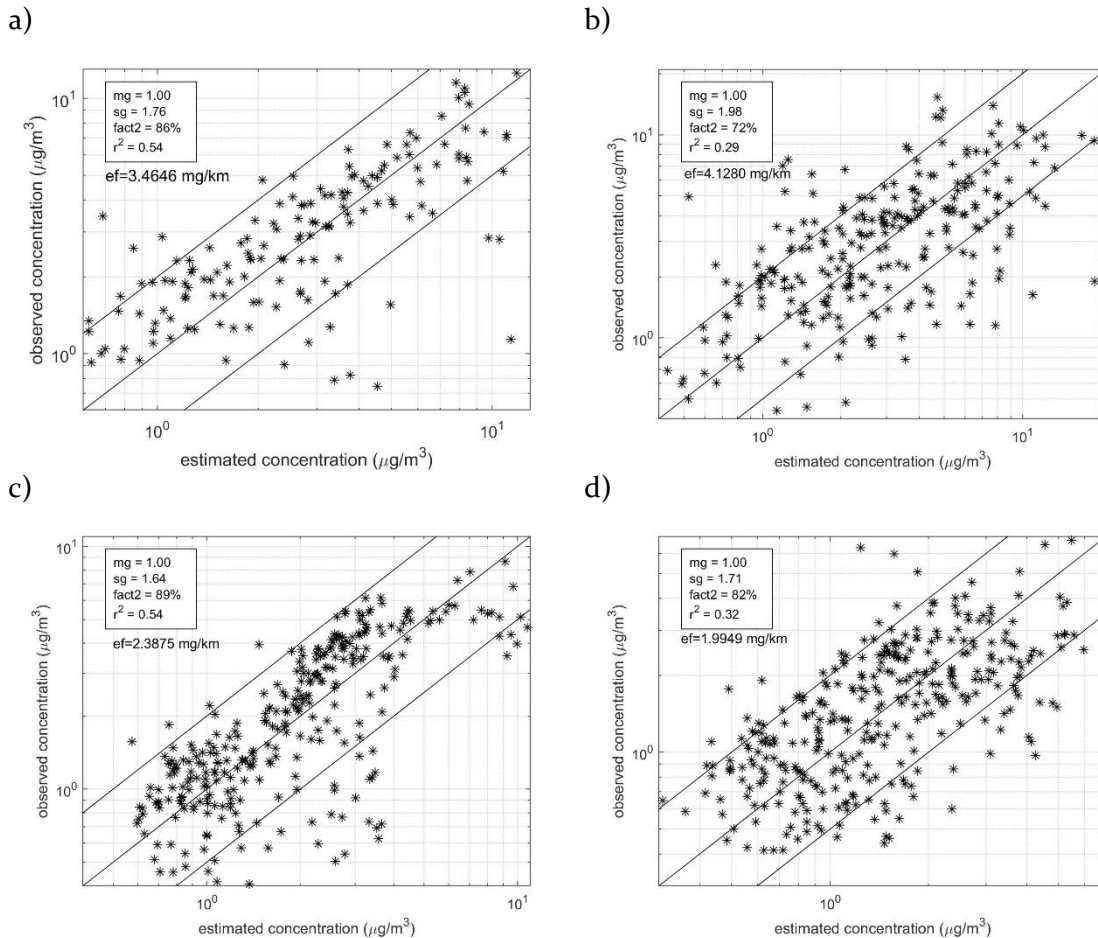


Figure 5-7- Comparison of BC observed concentrations and simple line source model estimates during a) winter unstable, b) winter stable, c) summer unstable, and d) summer stable. Emission factors are shown on each plot.

The performance assessment of the simple line source model in estimating NO<sub>x</sub> concentrations during winter and summer at both ‘near’ and ‘far’ stations is indicated in Figure 5-8. The estimated emission rate of LDV’s during winter is 0.331 g.km<sup>-1</sup> and 0.339 g.km<sup>-1</sup> during unstable and stable conditions, respectively (Figure 5-8a and b). The two emission rates are within the range of the reported emission rates in literature and the difference between these two emission rates is less than 3%.

The model estimates winter concentrations downwind of the freeway with  $r^2 = 0.54$  and  $r^2 = 0.27$  during unstable and stable conditions, respectively. The estimated winter concentrations are within a factor of two of the observations for 88% and 66% of the time during unstable and stable conditions, respectively.

The NO<sub>x</sub> emission rate of LDV's during summer is modeled to be 0.223 g.km<sup>-1</sup> and 0.185 g.km<sup>-1</sup> during unstable and stable conditions, respectively (Figure 5-8c and d). The two emission rates are also within the range of the reported emission rates in literature and the difference between these two emission rates is less than 17% which is also acceptable.

The model is able to estimate NO<sub>x</sub> summer concentrations downwind of the freeway with  $r^2 = 0.38$  during both unstable and stable conditions. The estimated summer concentrations are within a factor of two of the observations for 89% and 86% of the time during unstable and stable conditions, respectively.

The average NO<sub>x</sub> emission rate during winter is 1.64 times that during summer. This is consistent with findings in literature where higher emission rates of NO<sub>x</sub> during colder temperatures are reported (Christenson et al., 2014).

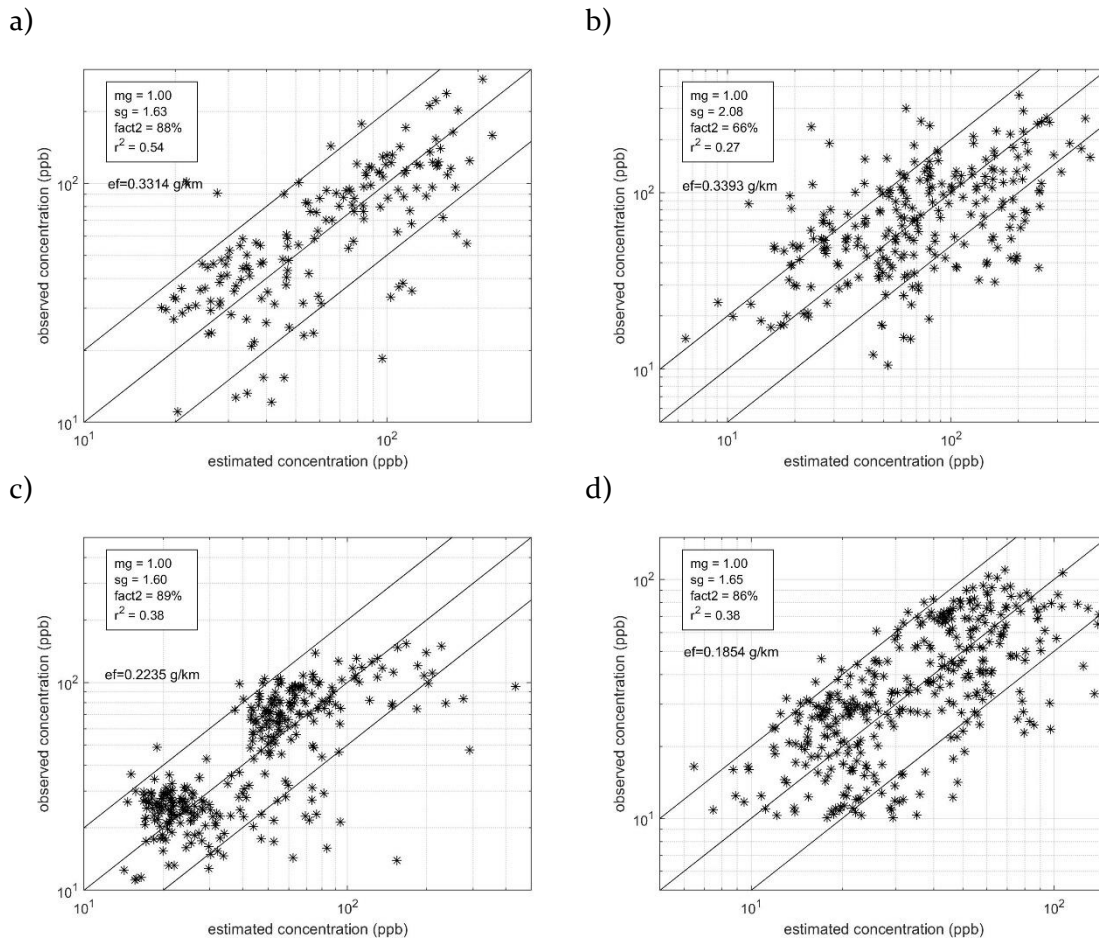


Figure 5-8- Comparison of NOx observed concentrations and simple line source model estimates during a) winter unstable, b) winter stable, c) summer unstable, and d) summer stable. Emission factors are shown on each plot.

### 5.5.2 Analytical line source model assessment

The performance of the analytical line source model in estimating BC concentrations during winter and summer at ‘near’ and ‘far’ stations is shown in Figure 5-9. Using the Analytical line source model, the BC emission rate of LDV’s during winter is estimated to be  $5.49 \text{ mg.km}^{-1}$  and  $6.99 \text{ mg.km}^{-1}$  during unstable and stable conditions, respectively (Figure 5-9a and b). The two emission rates are within the range of the reported emission rates in literature and the difference between these two emission rates is less than 22% which is acceptable considering the large uncertainty in emission factor estimations.

The model estimates winter concentrations downwind of the freeway with  $r^2 = 0.52$  and  $r^2 = 0.27$  during unstable and stable conditions, respectively. The estimated winter concentrations are within a factor of two of the observations for 85% and 75% of the time during unstable and stable conditions, respectively.

The BC emission rate of LDV's during summer is estimated to be  $3.58 \text{ mg.km}^{-1}$  and  $3.35 \text{ mg.km}^{-1}$  during unstable and stable conditions, respectively (Figure 5-9c and d). The two emission rates are also within the range of the reported emission rates in literature and the difference between these two emission rates is less than 9% which is also acceptable.

The model is able to estimate BC summer concentrations downwind of the freeway with  $r^2 = 0.50$  and  $r^2 = 0.27$  during unstable and stable conditions, respectively. The estimated winter concentrations are within a factor of two of the observations for 87% and 83% of the time during unstable and stable conditions, respectively. The average BC emission rate during winter is 1.8 times that during summer.

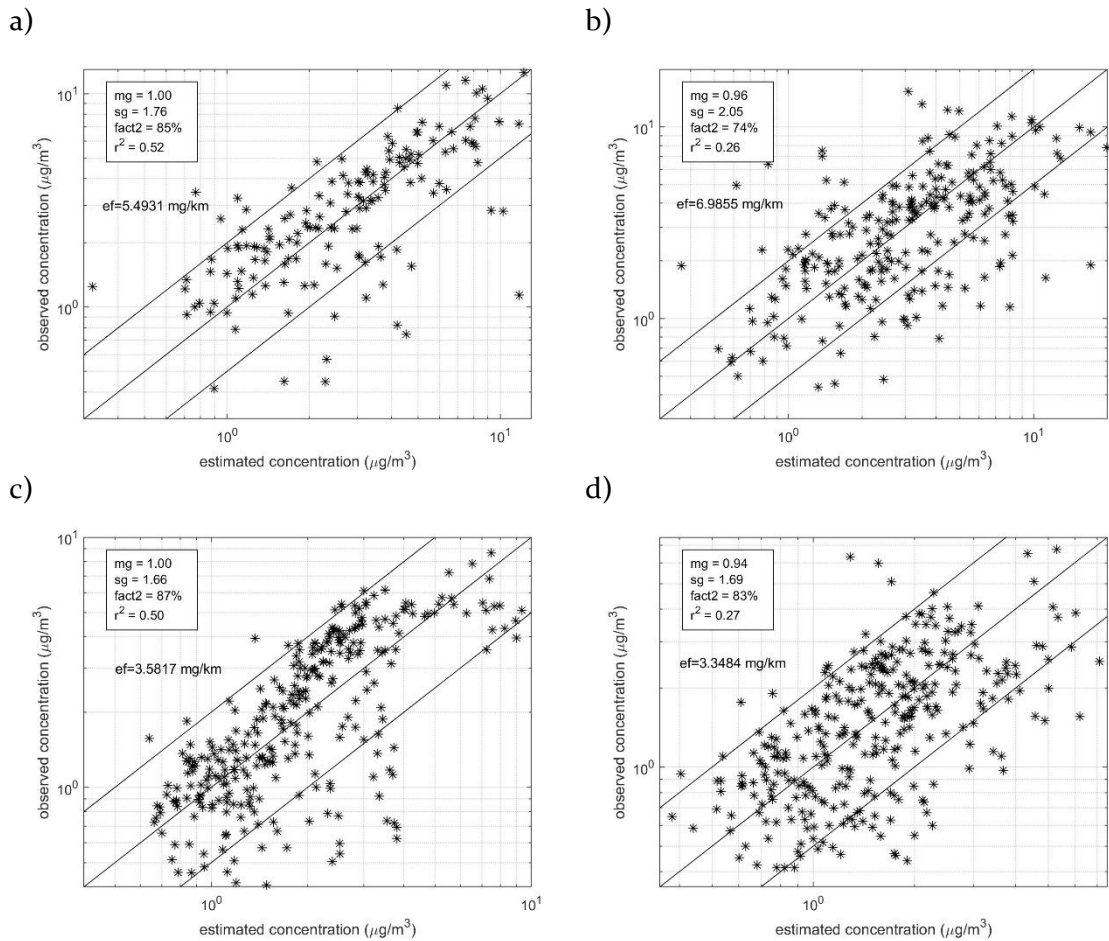


Figure 5-9- Comparison of BC observed concentrations and analytical line source model estimates during a) winter unstable, b) winter stable, c) summer unstable, and d) summer stable. Emission factors are shown on each plot.

The performance assessment of the analytical line source model in estimating NOx concentrations during winter and summer at both ‘near’ and ‘far’ stations is indicated in Figure 5-10. The estimated NOx emission rate of LDV’s during winter is 0.521 g.km<sup>-1</sup> and 0.562 g.km<sup>-1</sup> during unstable and stable conditions, respectively (Figure 5-10a and b). The two emission rates are within the range of the reported emission rates in literature and the difference between these two emission rates is less than 8%.

The model estimates winter concentrations downwind of the freeway with  $r^2 = 0.51$  and  $r^2 = 0.28$  during unstable and stable conditions, respectively. The estimated winter concentrations are within a factor of two of the observations for 84% and 68% of the time during unstable and stable conditions, respectively.

The NO<sub>x</sub> emission rate of LDV's during summer is modeled to be  $0.337 \text{ mg.km}^{-1}$  and  $0.303 \text{ mg.km}^{-1}$  during unstable and stable conditions, respectively (Figure 5-10c and d). The two emission rates are also within the range of the reported emission rates in literature and the difference between these two emission rates is 10% which is acceptable.

The model is able to estimate NO<sub>x</sub> summer concentrations downwind of the freeway with  $r^2 = 0.37$  and  $r^2 = 0.32$  during unstable and stable conditions, respectively. The estimated summer concentrations are within a factor of two of the observations for 88% and 83% of the time during unstable and stable conditions, respectively. The average NO<sub>x</sub> emission rate during winter is 1.70 times that during summer.

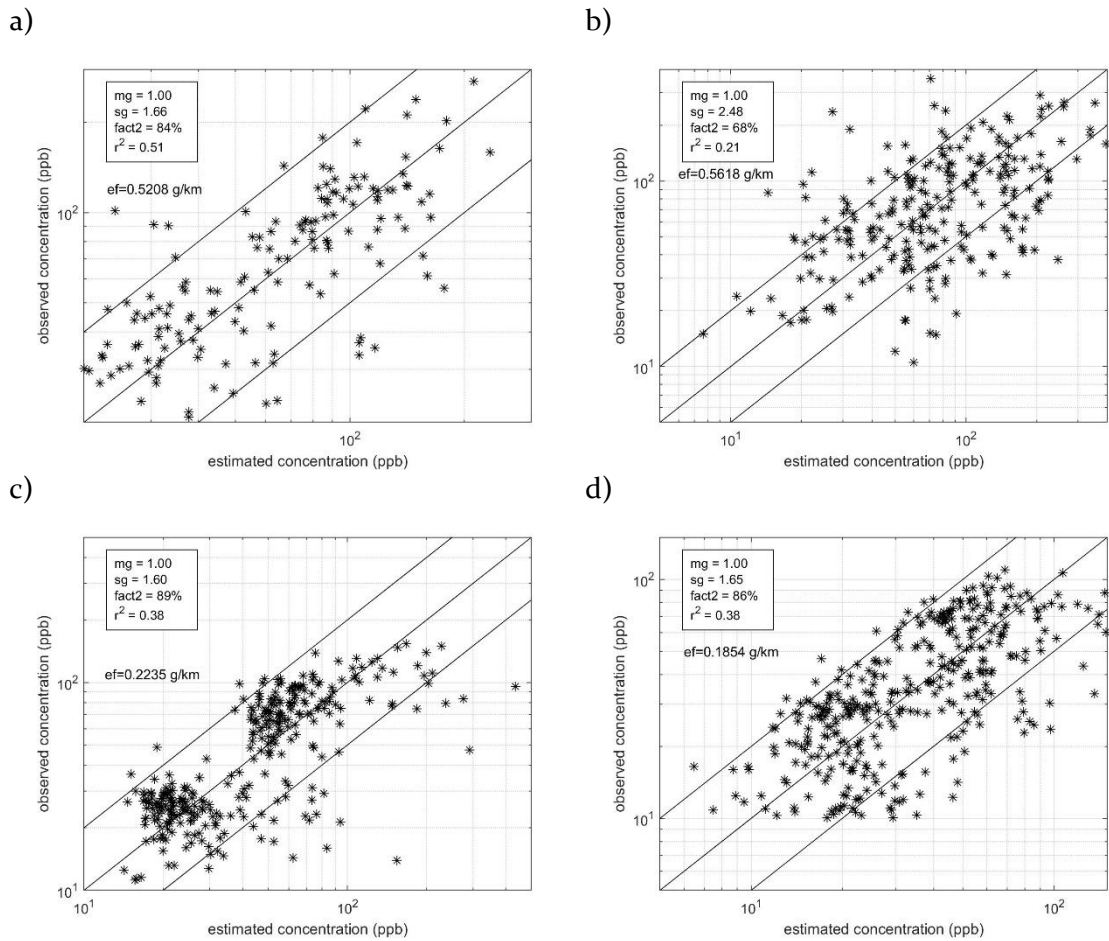


Figure 5-10- Comparison of NO<sub>x</sub> observed concentrations and simple line source model estimates during a) winter unstable, b) winter stable, c) summer unstable, and d) summer stable. Emission factors are shown on each plot.

## 5.6 Demonstration of the proposed system

In this section, we demonstrate how the proposed algorithm is applied to a real case. We downscale the daily satellite-derived 3-km PM<sub>2.5</sub> concentration ( $C_{sat}$ ) estimated at the intersection of the freeways I-405 and I-10 in West Los Angeles, CA, on December 1<sup>st</sup>, 2016. The first algorithm of the downscaling system reveals that  $C_{sat}$  at this grid during the specified date is  $10.40 \mu\text{g}/\text{m}^3$  (Al-Hamdan et al., 2014). For illustration purposes, we first

downscale the PM<sub>2.5</sub> concentrations to 500 m, and then to 100 m. We describe the downscaling procedure step by step as follows.

We first determine the exact co-ordinates of the 3-km grid and extract the hourly meteorological parameters measured at the closest meteorological station (Santa Monica Airport). Depending on the desired final scale of the concentrations, we set up the subgrids. To downscale concentrations from 3 km to 500 m, the 3-km grid should be divided into 6×6 subgrids. Figure 5-11 shows the co-ordinates of the 3-km grid and the subgrids.

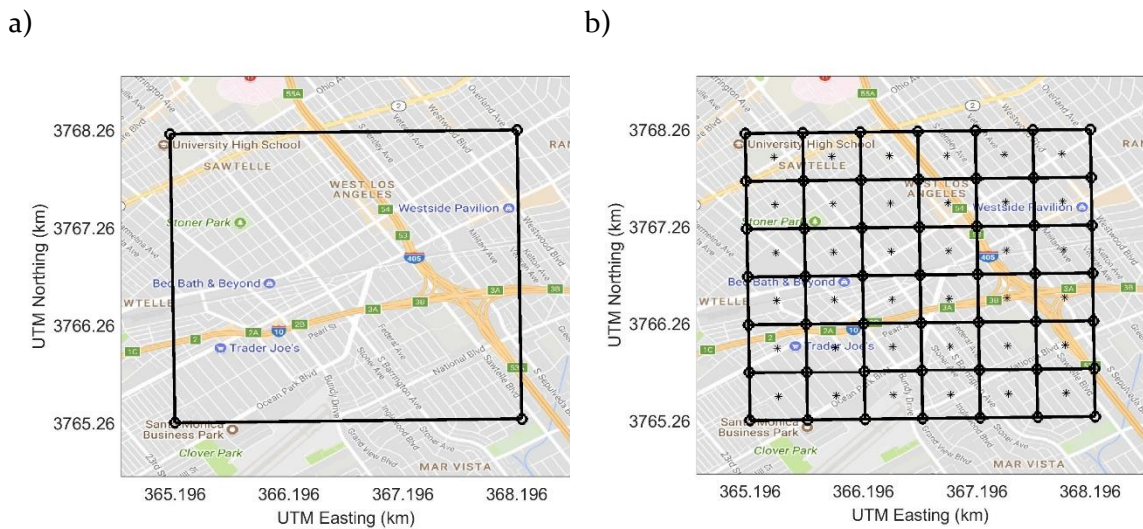


Figure 5-11- The area of study. The left panel shows the 3-km grid generated by (Al-Hamdan et al., 2014). The right panel shows the generated subgrids with their centers marked by asterisks. The scale of each subgrid is 500 m.

We then detect the line sources located within the grid (Figure 5-12) and estimate the primary PM<sub>2.5</sub> concentrations at the center of each subgrid due to emissions from the detected line sources. To do so, we use the analytical line source model along with the AADT of the detected line sources and EMFAC reported emission factor of PM<sub>2.5</sub> for LDV and HDV for fleet operating in Los Angeles County which are 0.0152 g.km<sup>-1</sup> and 0.1275 g.km<sup>-1</sup>.

It should be noted that the temporal resolution of the dispersion model output is one hour, while that of  $C_{sat}$  is 24 hours. Thus, we average the dispersion model outputs over the entire day and obtain the daily average value of the PM<sub>2.5</sub> local components ( $\Delta C_i$ ). The plot of  $\Delta C_i$  within the 3-km grid is shown in Figure 5-13. The model shows that on December 1<sup>st</sup>, 2016, the contribution of the detected line sources within the grid can be as high as  $5.64 \mu\text{g}/\text{m}^3$ . The model also estimates that the spatially-averaged contribution of the line sources on that particular day is  $\overline{\Delta C_i} = 0.85 \mu\text{g}/\text{m}^3$ . This indicates that the overall local PM<sub>2.5</sub> component constitutes only 8% of the reported satellite-derived total PM<sub>2.5</sub> concentration. Now, we have all the necessary components to downscale the satellite-derived PM<sub>2.5</sub> concentrations.

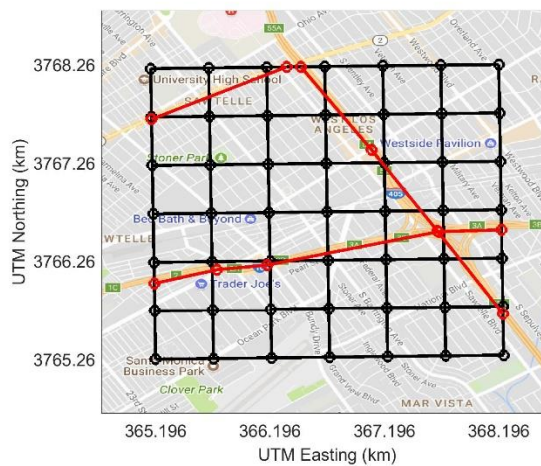


Figure 5-12- The line sources detected within the grid (indicated by red lines). The red circles indicate the traffic sensors available in AADT files



Figure 5-13 the plot of estimated daily-averaged primary PM<sub>2.5</sub> concentrations due to line sources within the 3-km grid.

We repeat the above-mentioned steps to downscale the same satellite-derived PM<sub>2.5</sub> concentration to 100 m. This requires dividing the grid into 300×300 subgrids. By using equations (5-1) and (5-2) and the results of the model over the finer subgrids, we are able to estimate the PM<sub>2.5</sub> concentration fields over the initial grid at much smaller scale (Figure 5-14). This figure shows that downscaled concentrations can be as twice as the satellite-derived concentrations next to major roads. Another important key point from this figure is that the minimum PM<sub>2.5</sub> concentration within the grid is  $C_{base} = C_{sat} - \overline{\Delta C_l} = 10.4 - 0.74 = 9.66 \mu\text{g}/\text{m}^3$ , which is only 9% smaller than the satellite-derived PM<sub>2.5</sub> concentration ( $C_{sat}$ ).

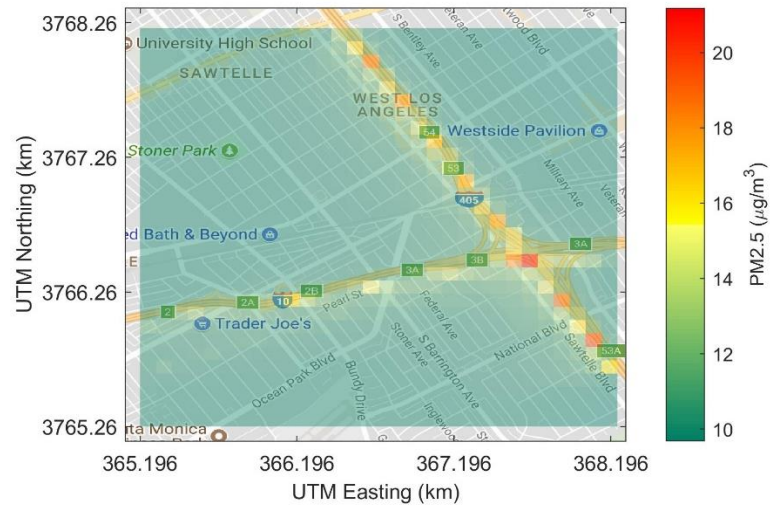


Figure 5-14- Downscaled PM<sub>2.5</sub> concentrations at the scale of 100 m.

## 5.7 Summary and conclusions

In this chapter, we describe a downscaling system that adapts roadway dispersion models to yield the concentration gradients that are not captured by the satellite maps. My contribution to this area of research is to show that line source dispersion models can be used to estimate near road concentrations in urban areas where emission factors and meteorological inputs are uncertain. I show that these models provide the best descriptions of the observations if stability effects are neglected and corrections are made to the friction velocity when wind speeds are low. This approach improves over methods of Land Use Regression (LUR) models that have been used to improve the spatial resolution of satellite-derived concentration maps (Kloog et al., 2011). LUR relates observed concentration gradients to land use factors such as proximity to roads using statistical methods. It represents a stationary picture of the concentration pattern at the time the concentration measurements were made. It thus cannot handle changes in emissions and cannot be used to examine the effects of emission changes on concentrations. On the other hand, the

dispersion model that we propose overcomes these difficulties in addition to providing a highly resolved map of concentrations.

The system detects the line sources within the satellite grid, along with their associated traffic flow rates. It divides the satellite grid into multiple subgrids. The number of subgrids depends on the degree of downscaling that one is interested in. It then runs a calibrated line source dispersion model to estimate primary PM<sub>2.5</sub> concentrations at each subgrid due to traffic activity of the line sources within the grid (line sources). The overall estimated local component of the PM<sub>2.5</sub> concentrations is subtracted from the satellite-derived PM<sub>2.5</sub> concentrations ( $C_{sat}$ ) to result in the regional component of the PM<sub>2.5</sub> concentration at the 3-km grid. The estimated local PM<sub>2.5</sub> components are then added to the regional components to result in the downscaled concentrations. The downscaled concentration can be used to improve the accuracy of the health risk assessments at the community scale.

The main uncertainty in the modeling results is related to the emission rates of different species. For dispersion model validation purposes, we treated the emission factors of NO<sub>x</sub> and BC as unknowns and we estimated the emission factors using the modeling results. However, since no PM<sub>2.5</sub> concentration data very close to the road were available, we were not able to calibrate the PM<sub>2.5</sub> emission factors; thus, we used those reported by EMFAC. The system output will improve if the PM<sub>2.5</sub> emission factor is calibrated against the concentrations measured near major roads.

Although we validated the performance of the line source dispersion models, we were not able to validate the final output of the proposed system because PM<sub>2.5</sub> concentration measurements near roads during the time that  $C_{sat}$  is available are not available. Once the  $C_{sat}$  is updated to the year 2017, we will be able to use PM<sub>2.5</sub> concentration measurements

by Purple Air low-cost monitors to validate the final product of the system.

## 6 Conclusions

Near road air quality is a public concern because exposure to elevated concentrations of vehicle emitted pollutants is associated with adverse health effects. This has motivated the development and application of models to estimate near road concentrations of traffic-related emissions. Roadway design is suggested as a potential strategy to mitigate near-road exposure to elevated vehicle-emitted pollutant concentrations. For example, roadside solid barriers can enhance dispersion, thereby mitigating elevated roadside concentrations. Some researchers have also suggested roadside vegetation as a potential mitigation strategy. However, the flow field downwind of vegetation is too complex to report a definitive result on the impact of vegetation on near-road air quality. Also, depressed road configurations decrease the surface concentrations downwind of the road compared to those of the flat terrain.

Practical dispersion models that can be used to estimate the impact of different road configurations on near-road concentrations of vehicle emissions are needed. The work in the first part of this dissertation develops semi-empirical dispersion models that are useful for linking vehicle emissions of complex road geometries with near-road concentrations.

First, two solid barrier dispersion models are developed to estimate concentrations downwind of a flat terrain freeway with a solid barrier along its downwind side. Second, wind tunnel measurements in vicinity of a flat terrain freeway with a thick vegetation barrier next to it are analyzed using dispersion models. Third, the impact of roadway depression on dispersion of roadway emissions is examined through modifying dispersion models that are applicable to flat terrain.

Additionally, health researchers have increasingly found that elevated PM<sub>2.5</sub> concentrations lead to increased risk of cardiovascular and respiratory diseases. An accurate health risk assessment on the community scale (10s-1000s of meters) requires concentration estimates at these spatial scales and at fine temporal scales. Satellite remote sensing provides a potentially cost effective way to estimate daily PM<sub>2.5</sub> concentrations by using Aerosol Optical Depth (AOD) in areas where air quality monitors are not available or are too sparse. However, the smallest scale of the current satellite-derived PM<sub>2.5</sub> concentrations is 3 km, which is still too large for an appropriate health risk assessment on the community scale. Air pollution concentrations on sub-kilometer to kilometer scales are typically estimated by dispersion models. Since major sources of PM<sub>2.5</sub> emissions in California are freeways, we develop a system that adapts roadway dispersion models to yield the concentration gradients that are not captured by satellite maps.

## **6.1 Roadside solid barriers**

Roadside solid barriers increase vertical dispersion of vehicular emissions by lofting emissions and inducing a recirculation zone on their leeward edge. The enhanced vertical

dispersion of the pollutant plume results in significant surface concentration reduction downwind of the barriers.

Two semi-empirical dispersion models were developed to describe the ultrafine particle measurements made in a field study downwind of a roadside solid barrier next to the UC Riverside campus. The developed models assume that the mixed-wake region behind the barrier results in constant concentrations from surface to the barrier height, while vertical concentration profiles follow normal distribution above the barrier height. The first model is a simplified version of model presented in Schulte et al. (2014), which assumes neutral conditions. The second model is a modification of the model described in Schulte et al. (2014) to account for reduced entrainment in the immediate wake of the barrier during unstable conditions. Both models performed well in estimating the pollutant concentrations. Due to large uncertainty in UFP emission factor, the models treat the emission factor as an unknown parameter whose value is computed by fitting the model estimates at large distances to the corresponding observed values.

The models predict that a 4 m barrier results in a 35% reduction in average concentration within 40 m (10 barrier heights) of the barrier, relative to the no-barrier site. This concentration reduction is 55% when the barrier height is doubled. The good performance of the simple barrier model reinforces the conclusion from Schulte et al. (2014) that the primary impact of the barrier is equivalent to shifting the line sources on the road upwind by a distance of about  $HU/u_* \cos\theta$ .

## 6.2 Roadside vegetation barriers

We analyzed the results from a wind-tunnel study to examine the impacts of vegetative and solid barriers on near-road air quality. While the solid barrier decreases ground-level concentrations downwind of the barrier compared to flat terrain by up to 0.3, the vegetation barrier results in an increase in surface concentrations (up to 50%) for several barrier heights downwind of vegetation compared to corresponding concentrations downwind of the freeway with no structures next to it. The wind tunnel results indicate formation of a recirculation zone immediately downwind of the solid barrier; however, a low-air-speed zone with no recirculation is observed downwind of the vegetation barrier. The low-air-speed zone is characterized by lower turbulence levels and persists to several barrier heights.

We incorporate the effects of the vegetation barrier on turbulence levels into a line source dispersion model applicable to at-grade roadways; while the vegetation barrier lofts some particles above its height, it decreases turbulence levels for the particles that pass through it. Two scenarios are examined; 1) The first scenario assumes that the only impact of vegetation on vehicular emissions is increasing initial vertical dispersion from  $h_0 = 0.8 \text{ m}$  for the at-grade case to  $h_0 = 3 \text{ m}$ , 2) The second scenario assumes that vegetation decreases surface friction velocity, from 0.25 m/s to 0.11 m/s, in addition to increasing initial vertical dispersion to 3 m. The observations show that the surface concentrations downwind of the vegetation lie within the concentrations estimated by these two scenarios. The surface concentrations close to the vegetation are better explained by the second scenario where the effects of vegetation on reducing surface friction velocity are accounted for, and those

far away from the vegetation are better explained by the first scenario, where the only effect of the vegetation on the flow field is increasing initial vertical dispersion. The shift from the second scenario to the first scenario occurs within  $[3H_w, 7H_w]$ , where  $H_w = 9\text{ m}$  is the vegetation barrier height, from the leeward edge of vegetation. Thus, the effect of vegetation on reducing turbulence does not go beyond  $7H_w$  from its leeward edge. It should be noted that the effect of the initial vertical plume spread on total vertical plume spread ( $\sigma_z$ ) diminishes as the downwind distance increases; thus, the surface concentrations downwind of vegetation barrier eventually converges to those of the flat terrain.

This analysis indicates that vegetative barriers influence dispersion of air pollutants close to the roadways in two counteracting ways: 1) they decrease turbulence behind the barrier that results in larger surface concentrations, and 2) they increase vertical mixing which reduces the surface concentrations. These two opposing effects can lead to a decrease or increase in concentrations relative to those in the absence of the barrier. This result may explain the inconclusiveness of the past research on the effects of vegetation on roadway-emitted pollutants.

### **6.3 Depressed roadway configurations**

Data from a wind-tunnel study (Heist et al., 2009) are analyzed to suggest modifications to flat terrain dispersion models to account for the effects of depressed roadways on dispersion. We examine three depressed roadway configurations; a 6 m deep depressed roadway with vertical sidewalls (D690), a 6 m deep depressed roadway with 30° angled sidewalls (D630), and a 9 m deep depressed roadway with vertical sidewalls (D990).

Observations of flow and dispersion for these configurations were compared with those from the flat roadway case (FLAT).

The first conclusion of this work is that the vertical concentration profiles under neutral stability conditions downwind of all configurations, including depressed and at-grade roadways, is best described by a distribution function with exponent 1.3, rather than the 2 used in most currently used dispersion models. Thus, in the first phase of model development, we utilized the van Ulden (1978) dispersion model with shape factor  $s = 1.3$  as the flat terrain road dispersion model.

The second conclusion of this work is that by modifying only two parameters of the flat terrain model for each case, the model is able to estimate downwind concentrations at all downwind distances and at all elevations. These modifications include an increase in initial vertical dispersion and an increase in the surface friction velocity relative to the flat terrain case. The friction velocity and initial vertical dispersion used to account for the effects of the depressed roadway increase with the depth of the depressed roadway. The largest increase in initial vertical dispersion occurs in D990 and the lowest occurs in D630, indicating that the strength of the recirculation zone determines the level of increase in initial vertical dispersion. However, the largest increase in surface friction velocity occurs in D630 and the lowest occurs in D690. The large vertical component of the wind speed at the edge of the sloped wall in D630 is assumed to contribute to the greater value of the surface friction velocity.

Similar modifications to the RLINE model also provide good descriptions of near-surface concentrations measured downwind of the depressed roadway configurations in the

wind tunnel (Heist et al., 2009). However, the modified RLINE model is not able to capture the vertical concentration profiles very well.

At this point, we do not have enough data to suggest a general formula to estimate these increases. However, the empirical results from our study are relevant to modeling the effects of depressed roadways that lie in the range of 6-9 m. The concentrations associated with emissions from these roadways can be estimated by increasing the friction velocity corresponding to flat terrain by a factor of 1.8 and using an initial vertical dispersion of about 4 m. This work provides a foundation for future studies that can result in development of a depressed roadway dispersion model formulation.

#### **6.4 Downscaling satellite-derived PM<sub>2.5</sub> concentrations**

A downscaling system is described that adapts roadway dispersion models to yield the concentration gradients that are not captured by the satellite maps. My contribution to this area of research is to show that line source dispersion models can be used to estimate near road concentrations in urban areas where emission factors and meteorological inputs are uncertain. I show that these models provide adequate descriptions of the observations if stability effects are neglected and corrections are made to the friction velocity when wind speeds are low. This approach improves over methods of Land Use Regression (LUR) models that have been used to improve the spatial resolution of satellite-derived concentration maps (Kloog et al., 2011). LUR relates observed concentration gradients to land use factors such as proximity to roads using statistical methods. It represents a stationary picture of the concentration pattern at the time the concentration measurements were made. It thus cannot handle changes in emissions and cannot be used to examine the effects of emission

changes on concentrations. On the other hand, the dispersion model that we propose overcomes these difficulties in addition to providing a highly resolved map of concentrations.

The system detects the intersects of the line sources with the satellite grid, along with their associated traffic flow rates. It divides the satellite grid into multiple subgrids. The number of subgrids depends on the degree of downscaling that one is interested in. It then runs a calibrated line source dispersion model to estimate primary PM<sub>2.5</sub> concentrations at each subgrid due to traffic activity of the line sources within the grid. The overall estimated local component of the PM<sub>2.5</sub> concentrations is subtracted from the satellite-derived PM<sub>2.5</sub> concentrations ( $C_{sat}$ ) to result in the regional component of the PM<sub>2.5</sub> concentration at the 3-km grid. The estimated local PM<sub>2.5</sub> components are then added to the regional components to result in the downscaled concentrations. The downscaled concentration can be used to improve the accuracy of the health risk assessments at the community scale.

The main uncertainty in the modeling results is related to the emission rates of different species. For dispersion model validation purposes, we treated the emission factors of NO<sub>x</sub> and BC as unknowns and we estimated the emission factors using the modeling results. However, since no PM<sub>2.5</sub> concentration data very close to the road were available, we were not able to calibrate the PM<sub>2.5</sub> emission factors; thus, we used those reported by EMFAC. The system output will improve if the PM<sub>2.5</sub> emission factor is calibrated against the concentrations measured near major roads.

## Bibliography

- Ahangar, F.E., Amini, S., Venkatram, A., 2017a. Using Vegetation to Enhance the Impact of Solid Barriers on Near-road Air Pollution. A&WMA's 110th Annu. Conf. Exhib.
- Ahangar, F.E., Heist, D., Perry, S., Venkatram, A., 2017b. Reduction of air pollution levels downwind of a road with an upwind noise barrier. *Atmos. Environ.* 155, 1–10. doi:10.1016/j.atmosenv.2017.02.001
- Al-Dabbous, A.N., Kumar, P., 2014. The influence of roadside vegetation barriers on airborne nanoparticles and pedestrians exposure under varying wind conditions. *Atmos. Environ.* 90, 113–124. doi:10.1016/j.atmosenv.2014.03.040
- Al-Hamdan, M.Z., Crosson, W.L., Economou, S.A., Estes, M.G., Estes, S.M., Hemmings, S.N., Kent, S.T., Puckett, M., Quattrochi, D.A., Rickman, D.L., Wade, G.M., McClure, L.A., 2014. Environmental Public Health Applications Using Remotely Sensed Data. *Geocarto Int.* 29, 85–98. doi:10.1080/10106049.2012.715209
- Amini, S., Ahangar, F.E., Schulte, N., Venkatram, A., 2016. Using models to interpret the impact of roadside barriers on near-road air quality. *Atmos. Environ.* 138, 55–64. doi:10.1016/j.atmosenv.2016.05.001
- Amini, S., Venkatram, A., Heist, D.K., Perry, S.G., 2017. Modeling the dispersion of pollutants in vicinity of depressed roadways, in: Proceedings of the Air and Waste Management Association's Annual Conference and Exhibition, AWMA.
- Baldauf, R., Thoma, E., Khlystov, a., Isakov, V., Bowker, G., Long, T., Snow, R., 2008. Impacts of noise barriers on near-road air quality. *Atmos. Environ.* 42, 7502–7507. doi:10.1016/j.atmosenv.2008.05.051
- Barad, M.L., 1958. Project prairie grass, a field program in diffusion. Volume 1 (no. Grp-59-vol-1). Air Force Cambridge Res. Labs Hanscom AFB MA. doi:10.1016/0022-460X(71)90105-2
- Beelen, R., Hoek, G., van Den Brandt, P.A., Goldbohm, R.A., Fischer, P., Schouten, L.J., Jerrett, M., Hughes, E., Armstrong, B., Brunekreef, B., 2008. Long-term effects of traffic-related air pollution on mortality in a Dutch cohort (NLCS-AIR study). *Environ. Health Perspect.* 116, 196.
- Bemis, G.R., Ranzieri, A.J., Benson, P.E., Peter, R.R., Pinkerman, K.O., Squires, B.T., 1977. Air pollution and roadway location, design, and operation- project overview. FHWA-CATL-7080-77-25, California Department of Transportation, Sacramento, CA.
- Benson, P.E., 1992a. A review of the development and application of the caline3 and 4 models 26, 379–390.

- Benson, P.E., 1992b. A review of the development and application of the caline<sub>3</sub> and 4 models 26, 379–390.
- Berkowicz, R., 2000. OSPM - a parameterised street pollution model. *Environ. Monit. Assess.* 65, 323–331. doi:10.1023/A:1006448321977
- Bowker, G.E., Baldauf, R., Isakov, V., Khlystov, A., Petersen, W., 2007. The effects of roadside structures on the transport and dispersion of ultrafine particles from highways. *Atmos. Environ.* 41, 8128–8139. doi:10.1016/j.atmosenv.2007.06.064
- Brantley, H.L., Hagler, G.S.W., J. Deshmukh, P., Baldauf, R.W., 2014. Field assessment of the effects of roadside vegetation on near-road black carbon and particulate matter. *Sci. Total Environ.* 468–469, 120–129. doi:10.1016/j.scitotenv.2013.08.001
- California Air Resources Board, 2007. EMFAC<sub>2007</sub> Users Guide. Mobile Source Emission Inventory. <http://www.arb.ca.gov/msei/documentation.htm>.
- Chang, J.C., Hanna, S.R., 2004. Air quality model performance evaluation. *Meteorol. Atmos. Phys.* 87, 167–196.
- Christenson, M., Loiselle, A., Karman, D., Graham, L. a, 2014. The Effect of Driving Conditions and Ambient Temperature on Light Duty Gasoline-Electric Hybrid Vehicles ( 2 ): Fuel Consumption and Gaseous Pollutant Emission Rates 776–790. doi:10.4271/2007-01-2137
- Chudnovsky, A.A., Koutrakis, P., Kloog, I., Melly, S., Nordio, F., Lyapustin, A., Wang, Y., Schwartz, J., 2014. Fine particulate matter predictions using high resolution Aerosol Optical Depth (AOD) retrievals. *Atmos. Environ.* 89, 189–198. doi:10.1016/j.atmosenv.2014.02.019
- Cimorelli, A.J., Perry, S.G., Venkatram, A., Weil, J.C., Paine, R.J., Wilson, R.B., Lee, R.F., Peters, W.D., Brode, R.W., 2005. AERMOD: A Dispersion Model for Industrial Source Applications. Part I: General Model Formulation and Boundary Layer Characterization. *J. Appl. Meteorol.* 44, 682–693. doi:10.1175/JAM2227.1
- Dominici, F., Peng, R.D., Bell, M.L., Mcdermott, A., Zeger, S.L., Samet, J.M., 2015. Fine Particulate Air Pollution and Hospital Admission for Cardiovascular and Respiratory Diseases 295, 1127–1134.
- Finn, D., Clawson, K.L., Carter, R.G., Rich, J.D., Eckman, R.M., Perry, S.G., Isakov, V., Heist, D.K., 2010. Tracer studies to characterize the effects of roadside noise barriers on near-road pollutant dispersion under varying atmospheric stability conditions. *Atmos. Environ.* 44, 204–214. doi:10.1016/j.atmosenv.2009.10.012
- Gehring, U., Wijga, A.H., Brauer, M., Fischer, P., de Jongste, J.C., Kerkhof, M., Oldenwening, M., Smit, H.A., Brunekreef, B., 2010. Traffic-related air pollution and the development

- of asthma and allergies during the first 8 years of life. *Am J Respir Crit Care Med* 181, 596–603. doi:10.1164/rccm.200906-0858OC
- Ghasemian, M., Amini, S., Princevac, M., 2017. The influence of roadside solid and vegetation barriers on near-road air quality. *Atmos. Environ.* 170. doi:10.1016/j.atmosenv.2017.09.028
- Gidhagen, L., Johansson, C., Langner, J., Foltescu, V.L., 2005. Urban scale modeling of particle number concentration in Stockholm. *Atmos. Environ.* 39, 1711–1725. doi:10.1016/j.atmosenv.2004.11.042
- Gold, D.R., Litonjua, A., Schwartz, J., Lovett, E., Larson, A., Nearing, B., Allen, G., Verrier, M., Cherry, R., Verrier, R., 2000. Ambient pollution and heart rate variability. *Circulation* 101, 1267–1273. doi:10.1161/01.CIR.101.11.1267
- Hagler, G.S.W., Lin, M.Y., Khlystov, A., Baldauf, R.W., Isakov, V., Faircloth, J., Jackson, L.E., 2012. Field investigation of roadside vegetative and structural barrier impact on near-road ultrafine particle concentrations under a variety of wind conditions. *Sci. Total Environ.* 419, 7–15. doi:10.1016/j.scitotenv.2011.12.002
- Hagler, G.S.W., Tang, W., Freeman, M.J., Heist, D.K., Perry, S.G., Vette, A.F., 2011. Model evaluation of roadside barrier impact on near-road air pollution. *Atmos. Environ.* 45, 2522–2530. doi:10.1016/j.atmosenv.2011.02.030
- Hasheminassab, S., Daher, N., Ostro, B.D., Sioutas, C., 2014. Long-term source apportionment of ambient fine particulate matter (PM 2.5) in the Los Angeles Basin: A focus on emissions reduction from vehicular sources. *Environ. Pollut.* 193, 54–64. doi:10.1016/j.envpol.2014.06.012
- Heist, D., Isakov, V., Perry, S., Snyder, M., Venkatram, A., Hood, C., Stocker, J., Carruthers, D., Arunachalam, S., Owen, R.C., 2013. Estimating near-road pollutant dispersion: A model inter-comparison [WWW Document]. *Transp. Res. Part D Transp. Environ.* doi:10.1016/j.trd.2013.09.003
- Heist, D.K., Perry, S.G., Brixey, L. a., 2009. A wind tunnel study of the effect of roadway configurations on the dispersion of traffic-related pollution. *Atmos. Environ.* 43, 5101–5111. doi:10.1016/j.atmosenv.2009.06.034
- Hitchins, J., Morawska, L., Wolff, R., Gilbert, D., 2000. Concentrations of submicrometre particles from vehicle emissions near a major road. *Atmos. Environ.* 34, 51–59. doi:10.1016/S1352-2310(99)00304-0
- Hoek, G., Brunekreef, B., Goldbohm, S., Fischer, P., van den Brandt, P.A., 2002. Association between mortality and indicators of traffic-related air pollution in the Netherlands: a cohort study. *Lancet* 360, 1203–1209. doi:10.1016/S0140-6736(02)11280-3

- Hoff, R., Christopher, S., 2009. The A&WMA 2009 Critical Review -- Remote Sensing of Particulate Pollution from Space: Have We Reached the Promised Land? *J. Air Waste Manage. Assoc.* 59, 645–675. doi:10.3155/1047-3289.59.6.645
- Holmes, N.S., Morawska, L., 2006. A review of dispersion modelling and its application to the dispersion of particles: An overview of different dispersion models available. *Atmos. Environ.* 40, 5902–5928. doi:10.1016/j.atmosenv.2006.06.003
- Hsu, N.C., Jeong, M.J., Bettenhausen, C., Sayer, A.M., Hansell, R., Seftor, C.S., Huang, J., Tsay, S.C., 2013. Enhanced Deep Blue aerosol retrieval algorithm: The second generation. *J. Geophys. Res. Atmos.* 118, 9296–9315. doi:10.1002/jgrd.50712
- Hu, X., Waller, L.A., Lyapustin, A., Wang, Y., Al-Hamdan, M.Z., Crosson, W.L., Estes, M.G., Estes, S.M., Quattrochi, D.A., Puttaswamy, S.J., Liu, Y., 2014. Estimating ground-level PM<sub>2.5</sub> concentrations in the Southeastern United States using MAIAC AOD retrievals and a two-stage model. *Remote Sens. Environ.* 140, 220–232. doi:10.1016/j.rse.2013.08.032
- Jacobs, A.F.G., 1983. Flow around a line obstacle. Thesis 122.
- Kaimal, J. C., & Finnigan, J. J. (1994). *Atmospheric boundary layer flows: their structure and measurement*. Oxford University Press.
- Kim, J.J., Smorodinsky, S., Ostro, B., Lipsett, M., Singer, B.C., Hogdson, A.T., 2002. Traffic-related Air Pollution and Respiratory Health: the East Bay Children's Respiratory Health Study. *Epidemiology* 13, S100.
- Kittelson, D.B., Watts, W.F., Johnson, J.P., Remerowki, M.L., Ische, E.E., Oberdorster, G., Gelein, R.A., Elder, A., Hopke, P.K., Kim, E., Zhao, W., Zhou, L., Jeong, C.H., 2004. On-road exposure to highway aerosols. 1. Aerosol and gas measurements. *Inhal. Toxicol.* 16, 31–39.
- Kloog, I., Koutrakis, P., Coull, B.A., Lee, H.J., Schwartz, J., 2011. Assessing temporally and spatially resolved PM<sub>2.5</sub> exposures for epidemiological studies using satellite aerosol optical depth measurements. *Atmos. Environ.* 45, 6267–6275. doi:10.1016/j.atmosenv.2011.08.066
- Kumar, P., Ketzler, M., Vardoulakis, S., Pirjola, L., Britter, R., 2011. Dynamics and dispersion modelling of nanoparticles from road traffic in the urban atmospheric environment-A review. *J. Aerosol Sci.* 42, 580–603. doi:10.1016/j.jaerosci.2011.06.001
- Lee, E.S., Ranasinghe, D.R., Ahangar, F.E., Amini, S., Mara, S., Choi, W., Paulson, S., Zhu, Y., 2018. Field evaluation of vegetation and noise barriers for mitigation of near-freeway air pollution under variable wind conditions. *Atmos. Environ.* 175, 92–99. doi:10.1016/j.atmosenv.2017.11.060

- Lee, H.J., Chatfield, R.B., Strawa, A.W., 2016. Enhancing the Applicability of Satellite Remote Sensing for PM<sub>2.5</sub> Estimation Using MODIS Deep Blue AOD and Land Use Regression in California, United States. *Environ. Sci. Technol.* 50, 6546–6555. doi:10.1021/acs.est.6b01438
- Lee, H.J., Liu, Y., Coull, B.A., Schwartz, J., Koutrakis, P., 2011. A novel calibration approach of MODIS AOD data to predict PM<sub>2.5</sub> concentrations. *Atmos. Chem. Phys.* 11, 7991–8002. doi:10.5194/acp-11-7991-2011
- Levy, R.C., Mattoo, S., Munchak, L.A., Remer, L.A., Sayer, A.M., Patadia, F., Hsu, N.C., 2013. The Collection 6 MODIS aerosol products over land and ocean. *Atmos. Meas. Tech.* 6, 2989–3034. doi:10.5194/amt-6-2989-2013
- Lin, M.Y., Hagler, G., Baldauf, R., Isakov, V., Lin, H.Y., Khlystov, A., 2016. The effects of vegetation barriers on near-road ultrafine particle number and carbon monoxide concentrations. *Sci. Total Environ.* 553, 372–379. doi:10.1016/j.scitotenv.2016.02.035
- Liu, Y., Franklin, M., Kahn, R., Koutrakis, P., 2007a. Using aerosol optical thickness to predict ground-level PM<sub>2.5</sub> concentrations in the St. Louis area: A comparison between MISR and MODIS. *Remote Sens. Environ.* 107, 33–44. doi:10.1016/j.rse.2006.05.022
- Liu, Y., Koutrakis, P., Kahn, R., 2007b. Estimating fine particulate matter component concentrations and size distributions using satellite-retrieved fractional aerosol optical depth: Part 1 - Method development. *J. Air Waste Manag. Assoc.* 57, 1351–1359. doi:10.3155/1047-3289.57.11.1351
- Liu, Y., Koutrakis, P., Kahn, R., Turquety, S., Yantosca, R.M., 2007c. Estimating fine particulate matter component concentrations and size distributions using satellite-retrieved fractional aerosol optical depth: Part 2 - A case study. *J. Air Waste Manag. Assoc.* 57, 1360–1369. doi:10.3155/1047-3289.57.11.1360
- Liu, Y., Paciorek, C.J., Koutrakis, P., 2009. Estimating regional spatial and temporal variability of PM<sub>2.5</sub> concentrations using satellite data, meteorology, and land use information. *Environ. Health Perspect.* 117, 886–892. doi:10.1289/ehp.0800123
- Liu, Y., Sarnat, J.A., Kilaru, V., Jacob, D.J., Koutrakis, P., 2005. Estimating Ground-Level PM<sub>2.5</sub> in the Eastern United States Using Satellite Remote Sensing. *Environ. Sci. Technol.* 39, 3269–3278. doi:10.1021/es049352m
- May, A.A., Nguyen, N.T., Presto, A.A., Gordon, T.D., Lipsky, E.M., Karve, M., Gutierrez, A., Robertson, W.H., Zhang, M., Brandow, C., Chang, O., Chen, S., Cicero-Fernandez, P., Dinkins, L., Fuentes, M., Huang, S.M., Ling, R., Long, J., Maddox, C., Massetti, J., McCauley, E., Miguel, A., Na, K., Ong, R., Pang, Y., Rieger, P., Sax, T., Truong, T., Vo, T., Chattopadhyay, S., Maldonado, H., Maricq, M.M., Robinson, A.L., 2014. Gas- and particle-phase primary emissions from in-use, on-road gasoline and diesel vehicles. *Atmos. Environ.* 88, 247–260. doi:10.1016/j.atmosenv.2014.01.046

- Miguel, A.H., Kirchstetter, T.W., Harley, R.A., Hering, S. V., 1998. On-road emissions of particulate polycyclic aromatic hydrocarbons and black carbon from gasoline and diesel vehicles. *Environ. Sci. Technol.* 32, 450–455. doi:10.1021/es970566w
- Morawska, L., Ristovski, Z., Jayaratne, E.R., Keogh, D.U., Ling, X., 2008. Ambient nano and ultrafine particles from motor vehicle emissions: Characteristics, ambient processing and implications on human exposure. *Atmos. Environ.* doi:10.1016/j.atmosenv.2008.07.050
- Nieuwstadt, F.T.M., van Ulden, A.P., 1978. A numerical study of the vertical dispersion of passive contaminants from a continuous source in the atmospheric surface layer. *Atmos. Environ.* 14, 267–269. doi:10.1016/0004-6981(80)90288-7
- Ning, Z., Hudda, N., Daher, N., Kam, W., Herner, J., Kozawa, K., Mara, S., Sioutas, C., 2010. Impact of roadside noise barriers on particle size distributions and pollutants concentrations near freeways. *Atmos. Environ.* 44, 3118–3127. doi:10.1016/j.atmosenv.2010.05.033
- Paciorek, C.J., Moreno-macias, H., 2008. Spatio-temporal Associations Between GOES Aerosol Optical Depth Retrievals and Spatio-temporal Associations Between GOES Aerosol Optical Depth Retrievals and 42, 5800–5806.
- Peters, A., Dockery, D.W., Muller, J.E., Mittleman, M.A., 2001. Increased particulate air pollution and the triggering of myocardial infarction. *Circulations* 103, 2810.
- Polidori, A., Fine, P.M., 2012. Ambient Concentrations of Criteria and Air Toxic Pollutants in Close Proximity To a Freeway With Heavy-Duty Diesel Traffic. Final Rep. Prep. by South Coast Air Qual. Manag. Dist. Diam. Bar, CA.
- Qian, W., Venkatram, A., 2011. Performance of Steady-State Dispersion Models Under Low Wind-Speed Conditions. *Boundary-Layer Meteorol.* 138, 475–491. doi:10.1007/s10546-010-9565-1
- Raupach, M.R., Woods, N., Dorr, G., Leys, J.F., Cleugh, H. a., 2001. The entrainment of particles by windbreaks. *Atmos. Environ.* 35, 3373–3383. doi:10.1016/S1352-2310(01)00139-X
- Remer, L.A., Mattoo, S., Levy, R.C., Munchak, L.A., 2013. MODIS 3 km aerosol product: Algorithm and global perspective. *Atmos. Meas. Tech.* 6, 1829–1844. doi:10.5194/amt-6-1829-2013
- Schulte, N., Amini, S., Ahangar, F.E., Venkatram, A., 2017. The Impact of Road Structures and Buildings on Urban Air Quality, in: 18th International Conference on Harmonisation within Atmospheric Dispersion Modelling for Regulatory Purposes.
- Schulte, N., Snyder, M., Isakov, V., Heist, D., Venkatram, A., 2014. Effects of solid barriers

- on dispersion of roadway emissions. *Atmos. Environ.* 97, 286–295. doi:10.1016/j.atmosenv.2014.08.026
- Schulte, N., Tan, S., Venkatram, A., 2015. The ratio of effective building height to street width governs dispersion of local vehicle emissions. *Atmos. Environ.* 112, 54–63. doi:10.1016/j.atmosenv.2015.03.061
- Snyder, M.G., Venkatram, A., Heist, D.K., Perry, S.G., Petersen, W.B., Isakov, V., 2013. RLINE: A line source dispersion model for near-surface releases. *Atmos. Environ.* 77, 748–756. doi:10.1016/j.atmosenv.2013.05.074
- Steffens, J.T., Heist, D.K., Perry, S.G., Isakov, V., Baldauf, R.W., Zhang, K.M., 2014. Effects of roadway configurations on near-road air quality and the implications on roadway designs. *Atmos. Environ.* 94, 74–85. doi:10.1016/j.atmosenv.2014.05.015
- Steffens, J.T., Wang, Y.J., Zhang, K.M., 2012. Exploration of effects of a vegetation barrier on particle size distributions in a near-road environment. *Atmos. Environ.* 50, 120–128.
- Tong, Z., Baldauf, R.W., Isakov, V., Deshmukh, P., Max Zhang, K., 2016. Roadside vegetation barrier designs to mitigate near-road air pollution impacts. *Sci. Total Environ.* 541, 920–927. doi:10.1016/j.scitotenv.2015.09.067
- Tong, Z., Whitlow, T.H., MacRae, P.F., Landers, A.J., Harada, Y., 2015. Quantifying the effect of vegetation on near-road air quality using brief campaigns. *Environ. Pollut.* 201, 141–149. doi:10.1016/j.envpol.2015.02.026
- U.S. Environmental Protection Agency, 2016. Technical Support Document (TSD) for Replacement of CALINE<sub>3</sub> with AERMOD for Transportation Related Air Quality Analyses. Report No. EPA- 454/ B-16-006, December.
- van Donkelaar, A., Martin, R. V., Park, R.J., 2006. Estimating ground-level PM<sub>2.5</sub> using aerosol optical depth determined from satellite remote sensing. *J. Geophys. Res. Atmos.* 111, 1–10. doi:10.1029/2005JD006996
- Van Donkelaar, A., Martin, R. V., Spurr, R.J.D., Drury, E., Remer, L.A., Levy, R.C., Wang, J., 2013. Optimal estimation for global ground-level fine particulate matter concentrations. *J. Geophys. Res. Atmos.* 118, 5621–5636. doi:10.1002/jgrd.50479
- van Ulden, A.P., 1978. Simple estimates for vertical diffusion from sources near the ground. *Atmos. Environ.* 12, 2125–2129. doi:10.1016/0004-6981(78)90167-1
- Venkatram, A., 2004. On estimating emissions through horizontal fluxes. *Atmos. Environ.* 38, 1337–1344. doi:10.1016/j.atmosenv.2003.11.018
- Venkatram, A., Amini, S., 2017. Classic Papers on Dispersion in the Surface Layer, in: 18th International Conference on Harmonisation within Atmospheric Dispersion

- Modelling for Regulatory Purposes. Bologna, Italy, pp. 1–5.
- Venkatram, A., Horst, T.W., 2006. Approximating dispersion from a finite line source. *Atmos. Environ.* 40, 2401–2408. doi:10.1016/j.atmosenv.2005.12.014
- Venkatram, A., Snyder, M.G., Heist, D.K., Perry, S.G., Petersen, W.B., Isakov, V., 2013. Re-formulation of plume spread for near-surface dispersion. *Atmos. Environ.* 77, 846–855. doi:10.1016/j.atmosenv.2013.05.073
- Vos, P.E.J., Maiheu, B., Vankerkom, J., Janssen, S., 2013. Improving local air quality in cities: To tree or not to tree ? 183.
- Wellenius, G.A., Burger, M.R., Coull, B.A., Schwartz, J., Suh, H.H., Koutrakis, P., Schlaug, G., Gold, D.R., Mittleman, M.A., 2012. Ambient air pollution and the risk of acute ischemic stroke. *Arch. Intern. Med.* 172, 229–34.
- Wilhelm, M., Ritz, B., 2003. Residential proximity to traffic and adverse birth outcomes in Los Angeles County, California, 1994–1996. *Environ. Health Perspect.* 111, 207–216.
- You, W., Zang, Z., Pan, X., Zhang, L., Chen, D., 2015. Estimating PM<sub>2.5</sub> in Xi’an, China using aerosol optical depth: A comparison between the MODIS and MISR retrieval models. *Sci. Total Environ.* 505, 1156–1165. doi:10.1016/j.scitotenv.2014.11.024
- Zhang, H., Hoff, R.M., Engel-Cox, J.A., 2009. The Relation between Moderate Resolution Imaging Spectroradiometer (MODIS) Aerosol Optical Depth and PM<sub>2.5</sub> over the United States: A Geographical Comparison by U.S. Environmental Protection Agency Regions. *J. Air Waste Manage. Assoc.* 59, 1358–1369. doi:10.3155/1047-3289.59.11.1358
- Zhang, K.M., Wexler, A.S., 2004. Evolution of particle number distribution near roadways—Part I: analysis of aerosol dynamics and its implications for engine emission measurement. *Atmos. Environ.* 38, 6643–6653. doi:10.1016/j.atmosenv.2004.06.043
- Zhu, Y., Hinds, W.C., Kim, S., Shen, S., Sioutas, C., 2002a. Study of ultrafine particles near a major highway with heavy-duty diesel traffic. *Atmos. Environ.* 36, 4323–4335. doi:10.1016/S1352-2310(02)00354-0
- Zhu, Y., Hinds, W.C., Kim, S., Sioutas, C., 2002b. Concentration and size distribution of ultrafine particles near a major highway. *J. Air Waste Manag. Assoc.* 52, 1032–1042. doi:10.1080/10473289.2002.10470842